# MSc Thesis:
# The Compaction of Moondust

## A Combined Gravity and Light Polarisation Study of Lunar Regolith

By A.H.J. Bakx

Delft University of Technology

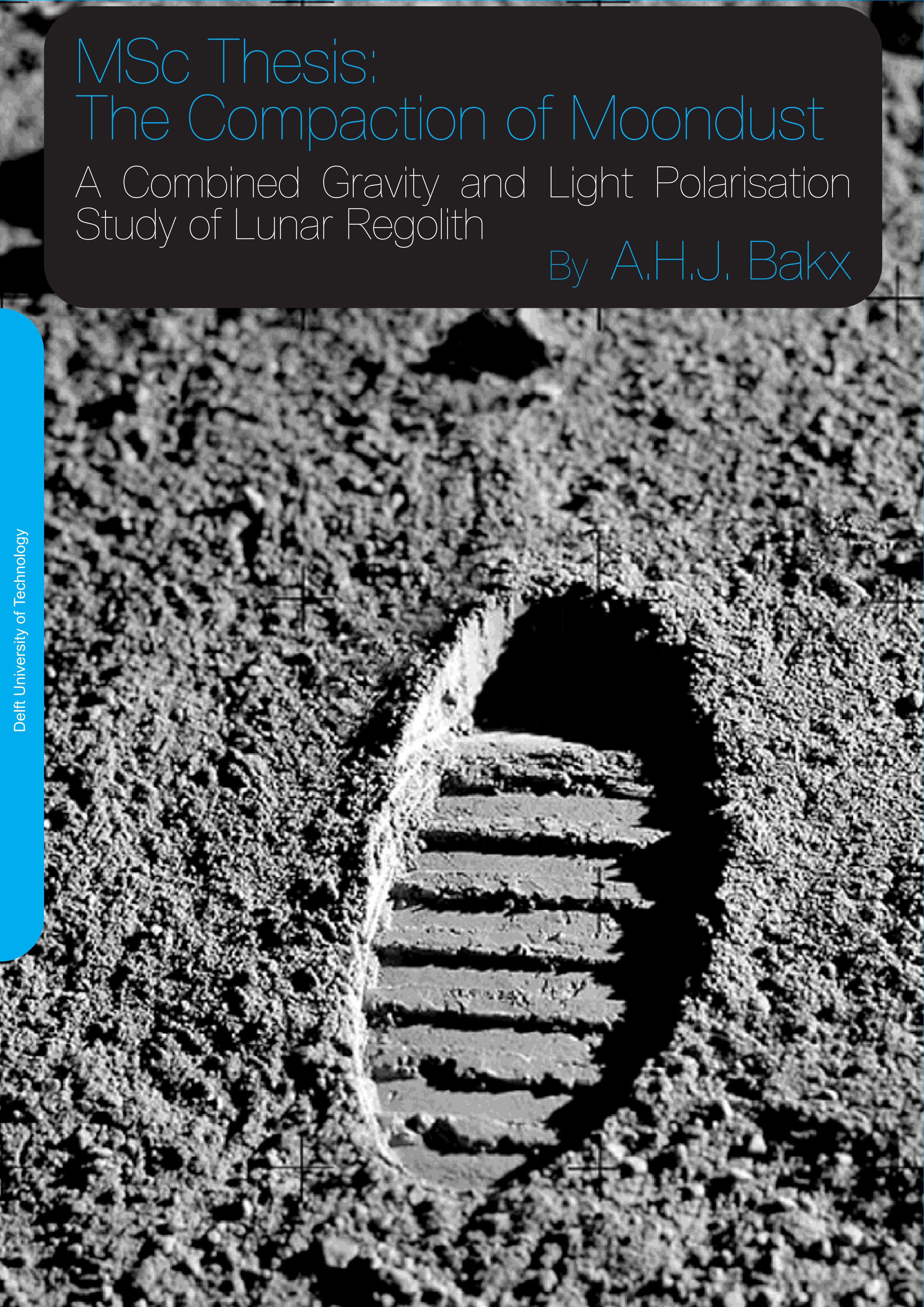

# MSc Thesis:
# The Compaction of Moondust

## A Combined Gravity and Light Polarisation Study of Lunar Regolith

by

## A.H.J. Bakx

to obtain the degree of Master of Science
at the Delft University of Technology,
to be defended publicly on Monday August 30, 2021 at 14:00 PM.

| | | |
|---|---|---|
| Student number: | 4578708 | |
| Project duration: | January 25, 2021 – August 30, 2021 | |
| Assessment Committee: | Dr.ir. B.C. Root, | Supervisor |
| | Dr. S.M. Cazaux, | Chair |
| | Dr. P.G. Ditmar | |

An electronic version of this thesis is available at `http://repository.tudelft.nl/`.

Cover image credits: courtesy to NASA (Hapke and Sato, 2015).

*That orbed maiden,*
*with white fire laden,*
*Whom mortals call the moon.*

~ Percy Bysshe Shelley

# Abstract

The Moon is covered by a blanket of rock fragments and loosely bound dust particles called regolith. This layer is key in deciphering the evolution of the Moon and the terrestrial planets, including Earth. It is also a protagonist in the return of humanity to the Moon after its last visit over half a century ago.

The main concern for lunar regolith studies is the determination of compactness. Compactness may be expressed as porosity and can be determined by the discrepancy between bulk density estimates from the gravity field and grain density estimates from material composition. New state-of-the-art gravity models of the Moon allow for small-scale gravity studies of regolith porosity, which have resulted in better understanding of the Moon's thermal evolution. However, regional variations in compactness are currently poorly known due to the ambiguous nature of gravity data. Ideally, an additional information source is desired to provide constraints on regolith compaction.

It might be that the amount of reflected sunlight from the lunar surface provides extra constraints on regolith compactness. For example, incident light can enter a more porous material deeper, increasing the probability of absorption and decreasing the amount of reflected light. Therefore, this thesis will explore the scattering behaviour of reflected sunlight from the lunar surface as a potential additional information source.

More specifically, interaction of sunlight with the lunar surface will leave a footprint in the reflected light, particularly in the polarisation degree. Subsequent analysis of this footprint has shown to contain information of physical characteristics of regolith, such as the grain size. This property is interesting, since the grain size also affects the amount of reflected sunlight. Moreover, the grain size will in turn influence the porosity of the regolith. Therefore, a triangular study of albedo, gravity-derived porosity and polarisation-derived grain size is carried out in this work.

First, models for vertical density and porosity distributions within the Moon's upper crust are determined through a spectral analysis of the gravity field. High correlations between the gravity field and surface topography allow for an unbiased estimate of crustal density as a function of spherical harmonic degree, called the effective density, and can be interpreted as a depth-dependent density estimation. Subsequent fitting of theoretical density profiles to the effective density provide estimates for the vertical density structure described by the surface density and density gradient. The surface density can be translated to regolith porosity through grain density estimates.

Second, lateral variations of density and porosity are determined by means of localisation of the global gravity field. Local effective density spectra are obtained by multiplication of localisation windows concentrated within a spherical cap with a given radius and spherical harmonic bandwidth. The windows are then systematically rotated to an area of interest in order to assure the whole lunar nearside is covered. Within the localisation window the lateral variation in density and porosity is constant. Therefore, the radius of the spherical cap is especially important for geologic complex areas such as the lunar maria.

Finally, Earth-based polarimetric observations of the lunar nearside are used to map the median grain size of lunar regolith. The prominent anti-correlation between the albedo and polarisation degree of the Moon's surface is exploited to determine the polarimetric anomaly, which is empirically related to the median grain size. The exact values resulting from this relationship should be treated with some caution however, as the overall variation is admissible.

The resulting median grain size map reveals a larger grain size in the lunar maria than in the highlands, most likely because of the difference in composition results in an increased sensitivity to comminution in the highlands as compared to the maria due to continuous bombardment of weathering agents on the Moon's surface.

From a triangular correlation study between gravity-derived porosity, polarisation-derived median grain size and albedo of lunar regolith, the amount of density and porosity distributions can be substantially limited. Porosities in the lunar highlands of 18 ± 2 % have been found, which are consistent with lunar soil samples and previously determined bulk porosities, while regional variations are novel.

Porosity estimates in the lunar maria remain uncertain, which is attributed to the geologically complex nature of the maria.

Based on these results, future studies could address the following aspects: first, gravity modelling of the lunar mare basalts, in particular the determination of basalt thickness. Second, reiteration of this study for the lunar farside, as new polarimetry observations are carried out in the near future. Finally, these new observations will enable the compaction of regolith to be inferred for the entire lunar surface, which will act as a direct constraint on the Moon's upper crustal density structure.

This method has only been demonstrated for the lunar nearside because Earth-based telescopes are not exposed to the farside due to the synchronous rotation of the Moon around Earth. The correlation study performs well in the lunar highlands and has limited applicability for the geologically complex lunar maria. Nevertheless, the results indicate the potential for future gravity space missions to carry a polarimeter on board.

# Preface

This thesis report is the culmination of my time as a student at Delft University of Technology. My time in Delft started with the pursuit of a BSc degree in Applied Physics, where I've had the opportunity to learn about the intriguing world of physics. During this time my passion for space flight never ceased to exist, which led me to the decision to get a MSc degree in Aerospace Engineering with specialisation in Space Exploration. I wanted to combine my enthusiasm for physics and space exploration in this thesis project, and I can definitely say that this has been accomplished. This project is about advancing the study of our nearest neighbour: The Moon. I firmly believe in a future where humans live on the Moon and explore its magnificent desolation,[1] which will serve as a stepping stone for humanity to explore Mars and beyond.

This project would not have been possible without my supervisor Bart: your weekly guidance and inspiration really helped me to carry out this work during a global pandemic. I would like to thank the research group and my fellow students for their helpful discussions, fun study sessions, and constructive feedback on this work. Furthermore, to my family and friends: I am truly thankful for your continued support, especially during the times when I gave unwanted mini-lectures about the technicalities of this work. Finally, I would like to express my gratitude towards the assessment committee for their time and effort.

*Aaron Bakx*
*Delft, August 2021*

---

[1] "Magnificent Desolation" were the famous words spoken by Astronaut Buzz Aldrin when he took his first step onto the lunar surface during the first human lunar landing mission in 1969. Later, he wrote a book carrying these words on its front cover Aldrin and Abraham (2010).

# Contents

**Abstract** iii

**Preface** v

**List of Figures** ix

**List of Tables** xiii

**Nomenclature** xv

**I Introduction** 1

**1 Introduction** 3

**2 The Moon** 5
- 2.1 Lunar Geology . . . 5
  - 2.1.1 The Dark Maria and Bright Highlands . . . 5
  - 2.1.2 Elemental Composition . . . 6
  - 2.1.3 Lunar Regolith . . . 7
  - 2.1.4 Lunar Soil Types . . . 8
- 2.2 Lunar Observations . . . 9
  - 2.2.1 Gravimetry from Lunar Orbit . . . 9
  - 2.2.2 Polarimetry from Earth-based Telescopes . . . 9

**3 Lunar Gravimetry** 11
- 3.1 Introduction to Gravity . . . 11
  - 3.1.1 The Gravitational Acceleration . . . 11
  - 3.1.2 Gravity Ambiguity . . . 13
  - 3.1.3 Spherical Harmonic Gravity . . . 14
- 3.2 A Brief History of Lunar Gravimetry . . . 15
- 3.3 The Gravity Recovery and Interior Laboratory (GRAIL) Mission . . . 17
- 3.4 Lunar Gravity and Topography . . . 17

**4 Lunar Polarimetry** 21
- 4.1 Introduction to Polarisation . . . 21
  - 4.1.1 Polarisation of Light . . . 21
  - 4.1.2 The Stokes Parameters . . . 22
- 4.2 A Brief History of Lunar Polarimetry . . . 23
- 4.3 Multi-band Polarimetric Observations of the Nearside Lunar Surface . . . 24

**5 Research Objective and Question** 27

**II Manuscript** 29

**Abstract** 31

**Plain Language Summary** 32

**1 Introduction** 32

**2 Method** 34
- 2.1 Vertical and Lateral Density Variations from the Gravity Field . . . 34
  - 2.1.1 Admittance and Effective Density . . . 34
  - 2.1.2 Theoretical Compaction Profiles . . . 35
  - 2.1.3 Localised Spectral Multitaper Approach . . . 36
  - 2.1.4 Lunar Regolith Grain Density and Porosity . . . 38

2.2 Polarimetric Anomaly and its Relation to Median Grain Size . . . 39
  2.2.1 Albedo and Polarisation Distribution of the Lunar Nearside . . . 39
  2.2.2 Polarimetric Anomaly and its Consequences for Surface Characteristics . . . 41
2.3 Polarimetric Constraints on the Moon's Crustal Density Structure . . . 43

**3 Results 44**
3.1 Density and Porosity Distributions from the Gravity Field . . . 44
3.2 Median Grain Size of Lunar Regolith from Polarimetry . . . 44
3.3 Triangular Correlations for Various Regolith Porosity Distributions . . . 47
3.4 Constrained Crustal Density and Porosity Structure . . . 49

**4 Discussion 50**
4.1 Type of Correlation and Comparison with Laboratory Photometry . . . 50
4.2 Selenographic Latitudinal Dependency . . . 51
4.3 Theoretical Density Models for the Moon's Crust . . . 53
4.4 Possible Causes for Non-unity Correlation . . . 54
4.5 Polarimetric Limitations . . . 55

**5 Conclusion 56**

**Acknowledgements 58**

**References 58**

**6 Supplementary Materials 63**
6.1 Theoretical Density Models . . . 63
6.2 Pearson Correlation . . . 63

**III Discussion and Conclusion 65**

**1 Validation and Verification 67**
1.1 Data Preparation . . . 67
1.2 Comparison of Polarimetric Anomaly . . . 67
1.3 Median Grain Size Estimates . . . 67
1.4 Mare Basalt Model . . . 69
1.5 Highland Linear Model and Spectral Localisation Approach . . . 71

**2 Supplementary Discussion 73**
2.1 The Different Behaviour of the Lunar Maria and Highlands . . . 73
2.2 Modelling Approach and Effect of Crustal Thickness Variations . . . 73
2.3 Localisation Robustness Analysis . . . 76
2.4 Possibility of Inaccurate Albedo Correction for Latitude . . . 79
2.5 Basalt Thickness Determination and Sensitivity Study . . . 80

**3 Conclusion 83**

**A Linear Least Squares Fitting Procedure 85**
A.1 Median Grain Size . . . 85
A.2 Effective Density . . . 86

**B Uncertainty Analysis 89**

**C Supplementary Spatial Maps 91**
C.1 Free Air Anomaly . . . 92
C.2 Topography . . . 93
C.3 Bouguer Anomaly . . . 94
C.4 Gravity Gradient . . . 97
C.5 Albedo . . . 98
C.6 Polarisation Degree . . . 99
C.7 Polarimetric Anomaly . . . 100

**Bibliography 101**

# List of Figures

2.1 Apparent albedo of the lunar nearside. The lunar *maria* are indicated with a striped white ellipse (Velikodsky et al., 2011). . . . 6

2.2 Photograph of the historic *Apollo* 11 mission showing a footprint in the moondust, implying a highly porous surface (Hapke and Sato, 2015). . . . 8

2.3 The phases of the Moon as observed from Earth. The angle between the Sun-Moon-Earth line affects observations of the Moon. Figure based on Pogge (2008). . . . 10

3.1 Coordinate system where the mass $M$ is positioned at the origin. Figure based on Hilst et al. (2002). . . . 11

3.2 Definition of the spherical coordinates $(r, \theta, \phi)$ with respect to the Cartesian coordinates $(x, y, z)$. Figure based on Hilst et al. (2002). . . . 12

3.3 Visualisation of the spherical harmonics up to degree and order 3. Figure based on Hilst et al. (2002). . . . 14

3.4 Associated Legendre polynomials with argument $\cos\theta$ up to degree and order 2. Figure based on Hilst et al. (2002). . . . 16

3.5 One- and two-dimensional power spectra for the GRGM1200B $\lambda_{\mathrm{RM1}} = 10$ spherical harmonics model . . . 18

3.6 Global free-air anomaly of the Moon from the GRAIL GRGM1200B RM1 $\lambda_{\mathrm{RM1}} = 10$ spherical harmonic model. The map is presented in a Mollweide equal area projection centered on 270°E longitude and show the farside on the left and nearside on the right. 19

3.7 Global surface topography of the Moon from the LOLA2600p spherical harmonic model, referenced to the GRGM1200B $\lambda_{\mathrm{RM1}} = 10$ lunar geoid. The map is presented in a Mollweide equal area projection centered on 270°E longitude and show the farside on the left and nearside on the right. . . . 19

3.8 Global lunar geoid from the GRAIL GRGM1200B RM1 $\lambda_{\mathrm{RM1}} = 10$ spherical harmonic model. The map is presented in a Mollweide equal area projection centered on 270°E longitude and show the farside on the left and nearside on the right. . . . 20

4.1 Linear polarised light. The electromagnetic wave propagated in the $z$-direction, and the linear polarised light is in the second and fourth quadrants. The magnetic field is not displayed for better interpretability (Hecht and Zajac, 2013). . . . 22

4.2 Visualisation of the physical properties of Stokes parameters $Q$, $U$, and $V$. Stokes $I$ is the total intensity of the wave. The direction of the source is into the paper (Landi Degl'Innocenti, E. and Bagnulo, S. and Fossati, L. , 2007). . . . 23

4.3 Typical polarimetric phase function of the Moon's surface (Kvaratskhelia, 1988). . . . 25

2.1 Effective density spectra for representative regions in a) Oceanus Procellarum, b) Mare Imbrium, c) Southern Highlands, and d) Northern Highlands. The colored line is the best fitting theoretical model, where red indicates the basalt model, and blue indicates the linear model. The black line represents the local observed effective density spectrum, with the grey lines being the standard deviation of the local spectrum. The dashed line is the spectral correlation between gravity and gravity predicted from topography (Bouguer correction). . . . 37

2.2 Nearside (a) surface density estimates for a linear density-with-depth profile with $\theta_{\mathrm{cap}} = 7.5°$, (b) grain density estimates from Lunar Prospector gamma ray spectrometer, and (c) porosity estimates. The maps are presented in an orthographic projection centered on 0° longitude. . . . 39

2.3 Nearside V-band (a) albedo- and (b) maximum polarisation ($P_{\mathrm{max}}$) maps of the Moon measured by Jeong et al. (2015). The maps are presented in an orthographic projection centered on 0° longitude. . . . . . . . . . . . . . . . . . . . . . . . . . . . . . . . . . 40

2.4 Anti-correlation between 630 nm albedo and maximum polarisation degree distributions for the nearside (a) lunar maria and (b) lunar highlands. The regression line is presented with empirical constants determined by Shkuratov and Opanasenko (1992) and from a best fit of the observations by Jeong et al. (2015). A darker colour is associated with a higher density of points. . . . . . . . . . . . . . . . . . . . . . . . . . . . . . . . . . 42

3.1 Overview of the density and porosity structures resulting from the localised spectral multitaper approach for cap radii ranging between 5° (150 km) to 70° (2150 km). The maps are presented in an orthographic projection centered on 0° longitude. . . . . . . . . . . 45

3.2 Nearside median grain size of lunar regolith estimates of the Moon. The map is presented in an orthographic projection centered on 0° longitude. Lunar maria are outlined by a thin solid white line, and large craters discussed in the text are indicated by a black circle. . . . . . . . . . . . . . . . . . . . . . . . . . . . . . . . . . . . . . . . . . . . 46

3.3 Nearside correlation between regolith albedo, polarisation-derived median grain size, and gravity-derived porosity of the Moon. Correlations are calculated between two parameters for a range of fixed values of the third; (a) albedo-porosity, (b) albedo-grain size, and (c) porosity-grain size. Correlation expressed as Szekely-Rizzo-Bakirov (SRB) distance correlation coefficient (Szekely et al., 2007), and presented by median values (dots) and 25th and 75th percentiles (whiskers) as a function of localisation spherical cap radius. . . . . . . . . . . . . . . . . . . . . . . . . . . . . . . . . . . . . . . . . 48

3.4 Nearside (a) density gradient, (b) surface density, and (c) surface porosity distributions that have highest correlations with polarimetric observations, resulting from the localised spectral multitaper approach for cap radius of 10° (300 km). The maps are presented in an orthographic projection centered on 0° longitude. . . . . . . . . . . . . . . . . . . . . . 49

4.1 Boxplots of nearside median grain size for the maria (red), highlands (blue), and total nearside (black) of the Moon, as a function of selenographic latitude $\beta$. The central lines within the boxes are the median values, and the boxes range from 25th to 75th percentiles. 52

4.2 Nearside correlation between regolith albedo, polarisation-derived median grain size, and gravity-derived porosity of the Moon as a function of selenographic latitude. Correlations are calculated for $\theta_{\mathrm{cap}} = 10°$ for each latitude band between two parameters for a range of fixed values of the third; (a) albedo-porosity, (b) albedo-grain size, and (c) porosity-grain size. . . . . . . . . . . . . . . . . . . . . . . . . . . . . . . . . . . . . . 53

6.1 Theoretical density models of the lunar highlands and maria. The highlands are modelled as density varying linearly with depth, with a surface density $\rho_{\mathrm{s,lin}}$ and density gradient $a$. The maria are modelled as a high-density basalt overlying a less-dense crust. The basalt has constant density $\rho_{\mathrm{b}}$ and thickness $T_{\mathrm{b}}$, and the crust underneath has an upper density of $\rho_0$ and density gradient $a$. . . . . . . . . . . . . . . . . . . . . . . . . . . . . 63

6.2 Nearside correlation between regolith albedo, polarisation-derived median grain size, and gravity-derived porosity of the Moon. Correlations are calculated between two parameters for a range of fixed values of the third; (a) albedo-porosity, (b) albedo-grain size, and (c) porosity-grain size. Correlation expressed as Pearson product-moment correlation coefficient (Szekely et al., 2007), and presented by median values (dots) and 25th and 75th percentiles (whiskers) as a function of localisation spherical cap radius. . 63

1.1 Comparison of the polarimetric anomaly $(P_{\mathrm{max}})^a A$ between the (a) B-band polarimetry with $a = 0.795$, (b) same B-band polarimetry by Jeong et al. (2015), and (c) 420 nm polarimetry by Shkuratov et al. (2007), for the western portion of the lunar disk. Light colors represent a higher value for the polarimetric anomaly, and vice-versa. . . . . . . 68

1.2 Theoretical effective density for various upper crustal densities (a), crustal linear density gradients (b), basalt densities (c), and basalt thicknesses (d) for the two-layer density model. Unless stated otherwise, an upper crustal density $\rho_0 = 2390$ kg/m$^3$, crustal linear density gradient $a = 21$ kg/m$^3$/km, basalt density $\rho_b = 2963$ kg/m$^3$, and basalt thickness $T_b = 0.3$ km is used for the model (Gong et al., 2016). . . . . . . . . . . . . . . 70
1.3 Validation of nearside linear surface density (a,c) and linear density gradient (b,d) estimates of the Moon. Lateral variations determined by a multitaper approach where 30 spherical caps are 99% concentrated each $r$ degrees in latitude and longitude, with various cap radii $\theta_{\text{cap}}$ and bandwidth $l_{\text{win}}$ indicated in the subcaptions. The same input parameters as used by Goossens et al. (2020) are used. Maps are presented in an orthographic projection centered on 0° longitude. Boundaries of the lunar maria are indicated by in (a) and (b) by a solid white and black line, respectively. . . . . . . . . . . . 72

2.1 Total nearside (a) albedo- and (b) maximum polarisation distributions of the Moon. . . . 74
2.2 Nearside maria (red) and highlands (blue) regions of the Moon (Nelson et al., 2014). The map is presented in an orthographic projection centered on 0° longitude. . . . . . . . . . 74
2.3 Box-and-whisker plots of nearside albedo (a) and maximum polarisation (b) for the maria (red) and highlands (blue) of the Moon, as a function of central wavelength of the four bands. The central lines within the boxes are the median values, the boxes range from 25th to 75th percentiles, and the whiskers range from 5th to 95th percentiles. The mean values are represented by open circles, and are connected by a solid line. . . . . . . . 75
2.4 The first three layer interfaces of a vertically layered crust with density distribution $\rho(z)$ and surface topography $h(x)$ for a given wavelength $2\pi/k$. Each layer has a constant density and each interface has a density contrast $d\rho = \frac{\partial\rho}{\partial z}\mathrm{d}z$, where $\mathrm{d}z$ is the infinitesimal distance between consecutive layers (Besserer et al., 2014). . . . . . . . . . . . . . . . 75
2.5 Nearside linear surface density estimates of the Moon. Lateral variations determined by a multitaper approach where 30 spherical caps are 99% concentrated each $r$ degrees in latitude and longitude, with various cap radii $\theta_{\text{cap}}$ indicated in the subcaptions. Maps are presented in an orthographic projection centered on 0° longitude. Boundaries of the lunar maria are indicated in (a) by a solid white line. . . . . . . . . . . . . . . . . . . . . . 77
2.6 Nearside linear density gradient estimates of the Moon. Lateral variations determined by a multitaper approach where 30 spherical caps are 99% concentrated each $r$ degrees in latitude and longitude, with various cap radii $\theta_{\text{cap}}$ indicated in the subcaptions. Maps are presented in an orthographic projection centered on 0° longitude. Boundaries of the lunar maria are indicated in (a) by a solid black line. . . . . . . . . . . . . . . . . . . . . . 78
2.7 Boxplots of nearside linear surface density (a) and nearside linear density gradient (b) of the Moon, as a function of spherical cap radius $\theta_{\text{cap}}$. The central lines within the boxes are the median values, the boxes range from 25th to 75th percentiles, and the whiskers range from 5th to 95th percentiles. The outliers are shown as black dots. . . . . . . . . 79
2.8 Basalt thickness estimates of the Moon by Du et al. (2019). Map is presented in an orthographic projection centered on 0° longitude. Boundaries of the lunar maria are indicated in by a solid black line, and basalt thickness estimates are indicated by a red dot. . . . . . . . . . . . . . . . . . . . . . . . . . . . . . . . . . . . . . . . . . . . . 80
2.9 Nearside linear surface density estimates of the Moon for (a) 75% basalt thickness, and (b) 125% basalt thickness. Lateral variations determined by a multitaper approach where 30 spherical caps are 99% concentrated each 5 degrees in latitude and longitude, with cap radius $\theta_{\text{cap}} = 10°$. Maps are presented in an orthographic projection centered on 0° longitude. . . . . . . . . . . . . . . . . . . . . . . . . . . . . . . . . . . . . . . 81

C.1 Nearside free air anomaly of the Moon for spherical harmonic degrees $1 \leq l \leq 650$. The map is presented in an orthographic projection centered on 0° longitude. . . . . . . . . . 92
C.2 Nearside topography of the Moon for spherical harmonic degrees $20 \leq l \leq 650$. The map is presented in an orthographic projection centered on 0° longitude. . . . . . . . . . 93
C.3 Nearside Bouguer anomaly of the Moon for spherical harmonic degrees $1 \leq l \leq 650$. The map is presented in an orthographic projection centered on 0° longitude. . . . . . 94

C.4 Nearside Bouguer anomaly of the Moon for spherical harmonic degrees $3 \leq l \leq 650$. The map is presented in an orthographic projection centered on 0° longitude. . . . . . . 95
C.5 Nearside Bouguer anomaly of the Moon for spherical harmonic degrees $250 \leq l \leq 650$. The map is presented in an orthographic projection centered on 0° longitude. . . . . . . 96
C.6 Nearside zz-component gravity gradient of the Moon for spherical harmonic degrees $20 \leq l \leq 650$. The map is presented in an orthographic projection centered on 0° longitude. . . . . . . 97
C.7 Nearside albedo of the Moon. The map is presented in an orthographic projection centered on 0° longitude. . . . . . . 98
C.8 Nearside maximum polarisation degree of the Moon. The map is presented in an orthographic projection centered on 0° longitude. . . . . . . 99
C.9 Nearside polarimetric anomaly of the Moon. The map is presented in an orthographic projection centered on 0° longitude. . . . . . . 100

# List of Tables

2.1 Composition of the lunar soil expressed in contribution of chemical compounds with corresponding density. Lunar soil composition taken from Lunar Prospector (Taylor et al., 2006), and density values taken from Haynes (2011). . . . . . . . . . . . . . . . . . . . . . 7
2.2 Median grain size for the characteristic lunar soil types, demonstrated by six Apollo lunar soil samples (Dollfus, 1998). . . . . . . . . . . . . . . . . . . . . . . . . . . . . . . . . . . 9

4.1 The four bands and their corresponding central wavelength of the polarimetric observations carried out by Jeong et al. (2015). . . . . . . . . . . . . . . . . . . . . . . . . . . . . 24

1.1 Determined empirical constants $a$ and $b$ with corresponding wavelength used for the regression line in log-log scale between albedo and maximum polarisation. . . . . . . . . 68
1.2 Median grain size of Apollo soil samples and estimates at the Apollo landing site locations, for both $a = 0.8294 \pm 0.0007$ and $a = 0.845$ at 630 nm, together with polarimetric properties $A$ and $P_{\max}$. An assumed uncertainty of $\delta a = 0.001$ is assumed for the latter $a$ value. . . . . . . . . . . . . . . . . . . . . . . . . . . . . . . . . . . . . . . . . . . 69

# Nomenclature

## Abbreviations

| | |
|---|---|
| **ASSB** | Atmosphere-less Solar System Body |
| **CF** | Center of Figure |
| **CM** | Center of Mass |
| **CNSA** | China National Space Administration |
| **D/O** | Degree and Order |
| **DPE** | Doppler Gravity Experiment |
| **ESA** | European Space Agency |
| **GRAIL** | Gravity Recovery and Interior Laboratory |
| **GSFC** | Goddard Space Flight Center |
| **ISRO** | Indian Space Research Organisation |
| **JAXA** | Japan Aerospace Exploration Agency |
| **JPL** | Jet Propulsion Laboratory |
| **KPLO** | Korea Pathfinder Lunar Orbiter |
| **LGRS** | Lunar Gravity Ranging System |
| **LOLA** | Lunar Orbiter Laser Altimeter |
| **LRO** | Lunar Reconnaissance Orbiter |
| **MIT** | Massachusetts Institute of Technology |
| **NASA** | National Aeronautics and Space Administration |
| **NPB** | Negative Polarisation Branch |
| **PB** | Principle Axis |
| **PM** | Primary Mission (of GRAIL) |
| **PolCam** | Wide-Angle Polarimetry Camera |
| **PPB** | Positive Polarisation Branch |
| **SELENE** | Selenological and Engineering Explorer |
| **SPA** | South Pole-Aitken basin |
| **SH** | Spherical Harmonics |
| **SMART** | Small Missions for Advanced Research in Technology |
| **VLBI** | Very Long Baseline Interferometry |
| **XM** | Extended Mission (of GRAIL) |

## Latin symbols

| | |
|---|---|
| $a$ | Linear density gradient |
| $A$ | Albedo |
| $A(l)$ | Autopower function |
| $b$ | Deviation of Umov effect |
| $C$ | Spherical harmonic coefficient |
| $D$ | Characteristic particle size |
| $d$ | Exponential depth scale |
| $\mathbf{E}$ | Electric field |
| $\mathbf{F}$ | Force vector acceleration |
| $G$ | Gravitational constant |
| $\mathbf{g}$ | Gravity field |
| $g$ | Gravity field magnitude |
| $\mathbf{H}$ | Magnetic field |
| $h$ | Height above reference surface |
| $I$ | Intensity |

| | |
|---|---|
| $k$ | Wavenumber |
| $l$ | Spherical harmonic degree |
| $m$ | Spherical harmonic order |
| $M$ | Mass |
| $P^{\mathrm{leg}}$ | Legendre polynomial |
| $P$ | Polarisation degree |
| $R$ | Reference radius |
| $\mathbf{r}$ | Position vector |
| $r, \theta, \phi$ | Spherical coordinate system |
| $S$ | Spherical harmonic coefficient |
| $t$ | Time |
| $U$ | Gravitational potential |
| $V$ | Volume |
| $x, y, z$ | Cartesian right-handed coordinate system |
| $X$ | Crosspower |
| $Z$ | Admittance |

## Greek symbols

| | |
|---|---|
| $\alpha$ | Phase angle |
| $\delta$ | Kronecker delta |
| $\mathcal{E}$ | Fourier transform equivalent of electric field |
| $\lambda$ | Wavelength |
| $\tilde{\lambda}$ | Scale factor between gravity and topography (RM1 constraint) |
| $\rho$ | Density |
| $\phi$ | Porosity |
| $\omega$ | Frequency |

## Superscripts

| | |
|---|---|
| ˆ | Unit vector |
| - | Normalised quantity |
| B | Bouguer |
| FA | Free Air |
| o | Observed |
| t | Topography |

## Subscripts

| | |
|---|---|
| 0 | Origin |
| $lm$ | Spherical harmonic coefficient of function in base of degree $l$ and order $m$ |
| eff | Effective |
| exp | Exponential |
| lin | Linear |
| max | Maximum |
| min | Minimum |
| s | Surface |
| $x, y, z$ | Cartesian direction |

## Miscellaneous

| | |
|---|---|
| $\nabla$ | Gradient operator |
| $\langle ... \rangle$ | Expectation value |

# Part I

# Introduction

# 1

# Introduction

Studies of the Moon's shallow surface are a trending topic for the construction of habitable complexes on the Moon and they are becoming of increasing importance as humanity is returning to the Moon after its last visit over half a century ago during NASA's Apollo program. Recent announcements of NASA's Artemis[1] program aim for humanity's return to the Moon by 2024 and subsequent sustainable lunar exploration, as well as being a training ground for the colonisation of Mars (Smith et al., 2020).

The Moon's shallow surface is made up of a blanket of loosely bound dust particles and rock fragments called regolith. This layer is a protagonist in lunar base designs, as it guides building location and materials (e.g. Gualtieri and Bandyopadhyay (2015)). In addition, the relevance for lunar regolith studies goes beyond human exploration of the Moon; the lunar surface has been preserved for most of the solar system's age and acts as a key for deciphering the evolution of the Moon and the terrestrial planets, including Earth (Zuber et al., 2012). A broad overview of the Moon's geology and lunar observations is presented in Chapter 2.

The main concern for regolith studies is the determination of compactness, as it plays a central role in several aspects. From a practical standpoint, if lunar soil is too loose, the construction of habitable complexes may be severely limited and robotic rovers may be unable to drive in the looser soil. Furthermore, it is expected that the compactness of regolith is influenced by moon quakes, nearby impact events and thermal cycling of the individual grains. Therefore, more accurate estimates of lunar regolith compactness may lead to a better understanding of the Moon's (thermal) evolution (Metzger et al., 2018).

Computation of regolith compactness has been attempted by many studies. Particularly, the high-resolution lunar gravity field[2] allows for upper crustal studies of the Moon and has been widely used to compute regolith compactness.

One can estimate the compaction by two quantities; the bulk density and the grain density. The bulk density is an estimate of density of a volume, whereas grain density stems from material composition. Therefore, the discrepancy between these two quantities is a measure for the amount of pore space (porosity) in the material, which is a measure for compactness.

One of the major gravity discoveries of the Moon is that the average density of the crust is estimated to be approximately 2550 kg/m$^3$, which is much lower than the density of the minerals that make up the crust: 2800-2900 kg/m$^3$. In order to account for this discrepancy, the crust must be fractured and porous, with approximately 12% void space up to depths of a few kilometers (Wieczorek et al., 2013).

Since then, studies have focused on determining vertical and lateral distributions of bulk density and porosity made possible by the increasing resolution of the Moon's gravity field (Goossens et al., 2020). A more elaborate introduction of lunar gravimetry is presented in Chapter 3.

However, gravity data has an intrinsic ambiguous property that limits accurate determination of regional variations in density and porosity. This ambiguous nature is due to a gravity signal essentially being a column integral of mass over a volume. Therefore, multiple density profiles will fit the same gravity signals.[3] Thus, it is desired to add constraints to the density and porosity profiles in addition to gravity constraints. In this thesis, the possibility of using the reflected sunlight of the lunar surface as an additional constraint will be explored.

---

[1] Artemis is a goddess of Greek mythology, and is associated with the hunt, the wilderness and the Moon. She is the twin sister of Apollo.

[2] The gravity field of the Moon is the most accurate measured gravity field of any astronomical body, with a current spatial resolution of approximately 4.5 km at the surface.

The behaviour of the reflected sunlight from the Moon's surface is determined by physical properties of lunar regolith (Hapke, 2008). For example, incident light can enter a more porous material deeper, increasing the probability of absorption and therefore decreasing the amount of reflected light. Therefore, analysis of the amount of reflected sunlight (albedo) of the lunar surface could better constrain the density and porosity of lunar regolith.

However, the albedo is also affected by other physical properties, such as the size of the regolith grains (Sakai and Nakamura, 2005), and grain size will in turn influence the porosity of the regolith (Kar et al., 2020). Nevertheless, the study of these interconnections may pose extra constraints on regolith porosity.

The interaction of sunlight with the lunar surface will leave a footprint in the reflected light, from which physical properties of lunar regolith can be inferred. The amount of linear polarisation (polarisation degree) in the reflected sunlight is commonly studied for regolith layers. The combination of albedo and polarisation degree contains ample information of physical characteristics of (lunar) regolith (Shkuratov et al., 2011). A more elaborate introduction to lunar polarimetry is presented in Chapter 4.

This report is structured in three parts. The remainder of Part I contains a more thorough introduction of the Moon (Chapter 2), lunar gravimetry (Chapter 3), and lunar polarimetry (Chapter 4). In Chapter 5, the research objective and questions are presented. Next, Part II is the main body of this report and contains the research of this work. It is a stand-alone document, meaning readers that are solely interested in the research can skip to this part. It is written as a manuscript that will be submitted to the journal *JGR Planets*. It contains an introduction (Chapter 1), the methods (Chapter 2), results (Chapter 3), discussions (Chapter 4) and conclusions (Chapter 5) of this study. Finally, Part III contains the validation and verification steps taken in this work (Chapter 1), supplementary discussion beyond the scope of the manuscript (Chapter 2), and conclusions of this study with recommendations for future studies (Chapter 3).

---

[3] A similar problem is the following; it is impossible to determine a curve when only its area is known.

# 2

# The Moon

The Moon is quite different from Earth. For one thing, it lacks a true atmosphere, and therefore the lunar surface has been well preserved due to the lack weather processes such as erosion. The Moon's radius is about a quarter of Earth's radius, and because of its smaller size and similar composition, it cooled faster than Earth and has a lower gravity of about 1/6$^{\text{th}}$ Earth's gravity. The lunar geomorphology has been dominated by impact cratering and volcanism processes (Srivastava and Varatharajan, 2016). An overview of the lunar geology is presented in Section 2.1.

At a mean distance from Earth of about 400.000 km, the Moon is responsible for the main production of the tides on Earth (Scott, 2015). The Moon is in synchronous rotation with Earth due to a tidal lock, resulting in the same hemisphere always facing the Earth (Zuber et al., 2012). The Earth-facing hemisphere is called the nearside, the other hemisphere, consequently, is called the farside. Observations of the Moon is done from Earth-based telescopes or from lunar orbit. An overview of lunar missions and a discussion of lunar observation is presented in Section 2.2.

This chapter serves as a more thorough introduction to the Moon. Readers that are solely interested in the research are referred to the manuscript in Part II.

## 2.1. Lunar Geology

### 2.1.1. The Dark Maria and Bright Highlands

When looking at the Moon with the naked eye, one can distinguish two lunar surface features.

There are the *maria*: smooth, dark, basaltic plains, formed by the flooding of large impact basins by ancient volcanic activity. The maria cover approximately 16% of the global lunar surface and nearly a third of the lunar nearside (Lissauer and Pater, 2013). Early astronomers thought of these regions being actual seas, hence the name maria (Latin for seas). One of the most well-known mare is Mare Tranquillitatis, pictured in Figure 2.1, being the landing site for the first manned lunar mission *Apollo 11* (Staid et al., 1996).

In contrast to the dark maria, the lunar surface is dominated by the brighter highlands, which cover approximately 80% of the lunar surface. The highlands are older than the maria, indicated by the presence of more impact craters (von Engelhardt et al., 1976).

The age of these regions has been determined by direct radiometric dating and crater counting. The highlands are estimated to be 4.4 Gyr old, while the maria are estimated to be 3.1-3.9 Gyr old. The lunar farside is crater-pocketed and features much more elevation differences than the nearside. A distinct feature on the farside is the South Pole-*Aitken* basin: the largest known impact crater in the Solar System (Petro and Pieters, 2004).

The difference in brightness of the lunar *maria* and highlands can be quantified by using the concept of albedo. Albedo is the latin word for 'whiteness', and describes the brightness of an astronomical body. As the Moon is illuminated by the Sun, the lunar surface reflects the sunlight back into space, which is what makes the Moon visible to people on Earth. Albedo is defined as the ratio between the reflected light to the total incident light, and has therefore a value between 0 and 1, where 1 means that all light is reflected of the surface of the body.

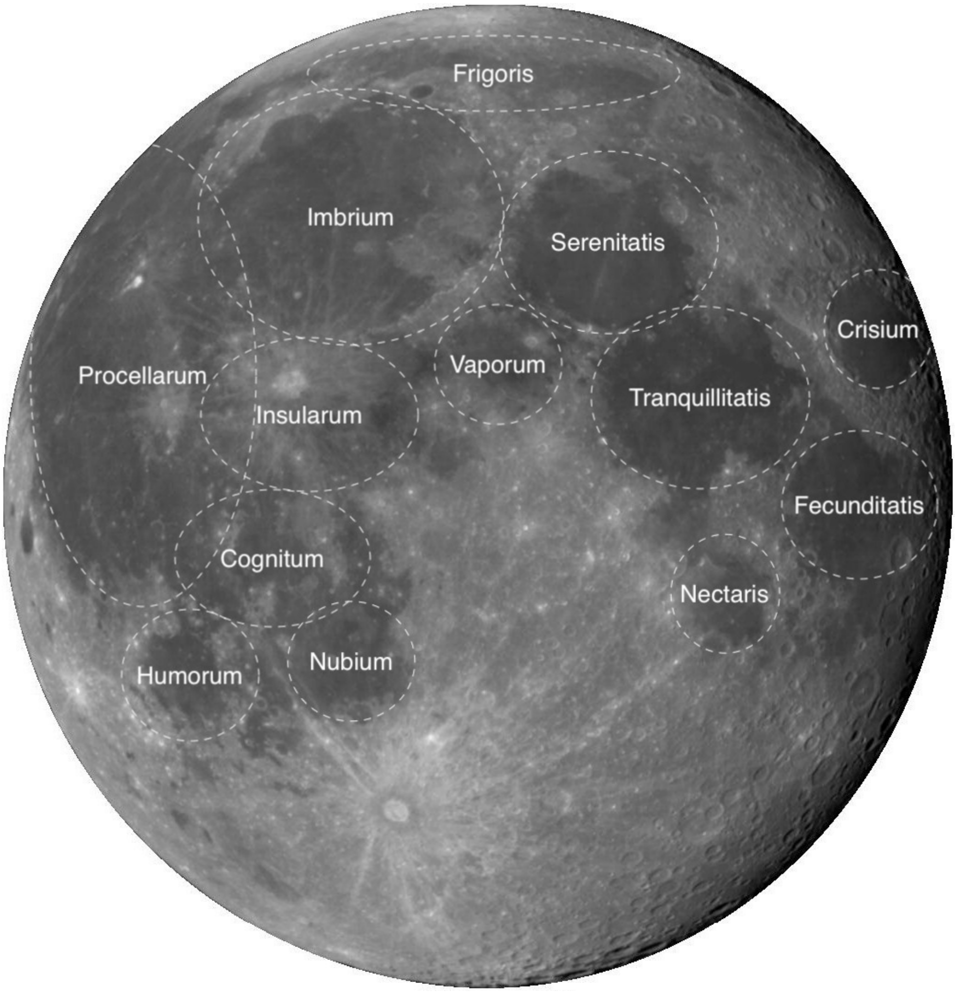

Figure 2.1: Apparent albedo of the lunar nearside. The lunar *maria* are indicated with a striped white ellipse (Velikodsky et al., 2011).

The darker *maria* have a lower albedo of 7-10%, compared to the bright highlands with an albedo of 11-18% (Lissauer and Pater, 2013). An albedo image of the lunar nearside, as observed by a telescope on Earth, is pictured in Figure 2.1. The prominent lunar *maria* are labelled in the picture. A derivative quantity of albedo is used for scientific study, called the equigonal albedo. It is a more suitable measure of albedo, as a correction has been applied to it for global brightness trend from the edge to the day/night boundary (Shkuratov et al., 2011).

### 2.1.2. Elemental Composition

Since the Moon is a differentiated body, the chemical composition of the lunar surface consists primarily of lighter elements; silicon dioxide ($SiO_2$) at an abundance of around 45% both for maria and highlands. Aluminium oxide ($Al_2O_3$) and calcium oxide (CaO) are more abundant in the highlands than in the maria: approximately 24% and 15% compared to 15% and 12%, respectively. Meanwhile, iron(II) oxide (FeO) and titanium dioxide ($TiO_2$) are more abundant in the maria than in the highlands: approximately 14% and 4% compared to 5% and 0.6%, respectively.

The remaining chemical composition is made up of magnesium oxide (MgO) and sodium oxide ($Na_2O$) with similar abundances in the maria and highlands of around 8% and 0.6%, respectively (Taylor et al., 2006). A summary of the elemental composition of the Moon is presented in Table 2.1, together with the density value of each chemical compound. It is recognised that compounds more abundant in the maria are higher in their density compared to the other compounds.

The maria are large flows of basaltic lava-filled plains. Most of the maria erupted within or flowed into low-lying impact basins on the nearside. One major exception is Oceanus Procellarum, the largest

Table 2.1: Composition of the lunar soil expressed in contribution of chemical compounds with corresponding density. Lunar soil composition taken from Lunar Prospector (Taylor et al., 2006), and density values taken from Haynes (2011).

| Compound | $SiO_2$ | $Al_2O_3$ | CaO | FeO | MgO | $TiO_2$ | $Na_2O$ |
|---|---|---|---|---|---|---|---|
| Composition maria, % | 45.4 | 14.9 | 11.8 | 14.1 | 9.2 | 3.9 | 0.6 |
| Composition highlands, % | 45.5 | 24.0 | 15.9 | 5.9 | 7.5 | 0.6 | 0.6 |
| Density, kg/m$^3$ | 2650 | 3950 | 3340 | 5740 | 3580 | 4230 | 2270 |

mare, which does not correspond to a known impact basin. It is thought that the maria are mostly present on the nearside because the nearside crust is thinner than the farside crust (Wieczorek et al., 2013). Basalts are mafic igneous volcanic rocks formed by rapid solidification of lava. The term mafic indicates rocks with a large abundances of magnesium (Mg) and iron (Fe), and less abundance of silicon dioxide. Lunar basalts differ from those on Earth in their high iron content, typically 17 to 22 wt% FeO,[1] and a wide range of titanium concentrations of 1 to 13 wt% $TiO_2$ (Gong et al., 2016).

The highlands are anorthositic in composition formed by crystallisation of lava. Anorthosites are igneous monomineralic rocks primarily (>90%) composed of plagioclase feldspar with a low mafic component (<10%). The term 'plagioclase feldspar' indicates tectosilicate minerals, meaning the minerals are made up of silicate groups (Ohtake et al., 2009).

### 2.1.3. Lunar Regolith

The Moon is covered by loosely bound dust particles, called moondust, which make up the lunar regolith. The regolith is mainly a consequence of rocks being disintegrated due to a long exposure to meteoric impacts and space weathering (von Engelhardt et al., 1976). The average size of moondust particle is estimated to be a little less than 100 μm, and the regolith layer's thickness is estimated to be between 5 to 10 meters (Hapke and Sato, 2015). This section provides a way of characterising and describing the Moon's regolith surface layer.

The definition of density $\rho$ for completely homogeneous materials is defined by by the fraction mass $m$ over volume $V$

$$\rho \equiv \frac{\text{mass}}{\text{volume}} = \frac{m}{V}, \tag{2.1}$$

and expressed in kg m$^{-3}$. More precisely, the definition given in Equation 2.1 is called the volumetric mass density, also known as specific mass (Hilst et al., 2002). The density of an homogeneous material is completely determined by its volume in space and mass enclosed in this volume. The average density of the lunar crust is estimated to be 2550 kg m$^{-3}$ for the lunar highlands (Wieczorek et al., 2013).

However, pictures of footsteps of astronauts on the lunar surface (see Figure 2.2) reveal that the first centimetres is compacted, implying a porous material. Qualitatively speaking, a porous material is a material that contains pores, meaning liquids and gasses can be present inside the (void) spaces in the material. The lunar regolith is made up of individual particles, and when packed together will not form a completely homogeneous material.

The density of a regolith in itself may not provide an accurate measure for the physical properties of the regolith. In addition, the measure of porosity is often expressed together with density. Porosity is denoted by symbol $\phi$[2], and is a measure of the pore volumes in a material. It is defined as the fraction of pore volume over the total volume of the material

$$\phi \equiv \frac{\text{pore volume}}{\text{total volume}}, \tag{2.2}$$

and is therefore a dimensionless quantity between 0 and 1 (Hilst et al., 2002).

In geophysical studies, the porosity is often calculated from density. A porous material consists of individual so-called grains. For example, lunar regolith is made up of moondust. One can distinguish between three measures of density for regolith, namely the *bulk* density $\rho_{\text{bulk}}$, *grain* density $\rho_{\text{grain}}$, and the *pore* density $\rho_{\text{pore}}$. The bulk density is the average density of the regolith as calculated by

---

[1] wt% denotes the mass fraction of a particular substance with respect to the total mass.

[2] The used symbol for porosity is debatable in common literature. In gravity studies, it is common to use $\phi$, whereas photometric studies often use $P$. In the end, the used symbol in this work must not be confused with the filling factor, sometimes also denoted as $\phi$ (Hapke and Sato, 2015).

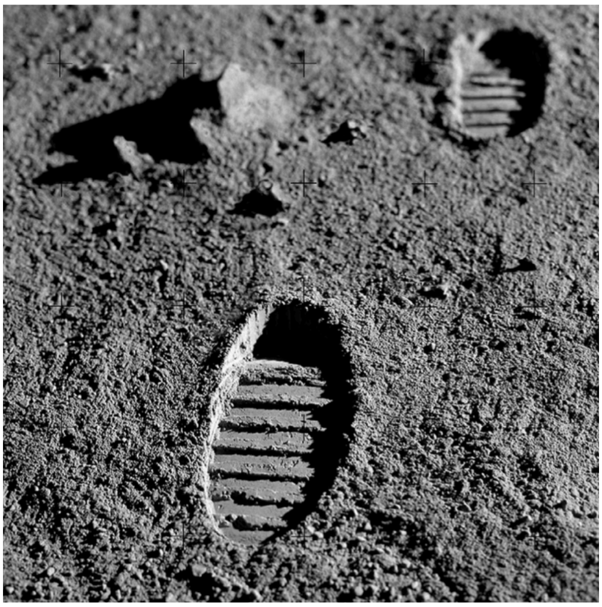

Figure 2.2: Photograph of the historic *Apollo* 11 mission showing a footprint in the moondust, implying a highly porous surface (Hapke and Sato, 2015).

Equation 2.1. The grain density is the density of the individual grains in the material, whereas the pore density is the density of the pores. Then the porosity can be calculated as

$$\phi = \frac{\rho_{\text{grain}} - \rho_{\text{bulk}}}{\rho_{\text{grain}} - \rho_{\text{pore}}}. \tag{2.3}$$

If a fluid is present in the pores, the pore density will become influential to the calculation of porosity. However, in most geological materials, air is present in the pores, and since air density is much smaller than grain density ($\rho_{\text{grain}} - \rho_{\text{pore}} \approx \rho_{\text{grain}}$), Equation 2.3 reduces to the simpler form of

$$\phi = 1 - \rho_{\text{bulk}}/\rho_{\text{grain}}, \tag{2.4}$$

to calculate porosity (Hilst et al., 2002). This is a valid assumption on Earth. On atmosphere-less astronomical bodies, such as the Moon, these pores are usually a vacuum, such that Equation 2.4 is exact. The average porosity of the lunar crust is estimated to be 12% (Wieczorek et al., 2013), increasing to 20% and higher on the surface (Goossens et al., 2020, Hapke and Sato, 2015).

### 2.1.4. Lunar Soil Types

The regolith structure of the lunar surface is the result of comminution of rocks by micrometeroid impacts integrated over very long periods of time. Each impact produces a progressive decrease of grain sizes. When temperatures get sufficiently high by volcanic activity, grains of glass-like nature are produced, such as agglutinates (clumping of grains) and spherules (Zellner, 2019). Distinct lunar soil types can be recognized based on their exposure to space weathering and (micro-)meteroid impacts.

Lunar surfaces that are steady state areas since they have reached space weathering and impact saturation due to their geological old age are called *mature* soils. Areas that have been geologically recently covered by nearby impact ejecta material produce *immature* soils. The newly resurfaced immature soils can be modified by space weathering and impact comminution, and are called *sub-mature* soils. Areas that have not been significantly modified by space weathering and impact comminution, such that they are in their original state, are called *fresh* soils. For example, the rims of new craters have a high probability of consisting of fresh lunar soil. As previously discussed, some grains are not formed by mechanical comminution but by melting processes due to volcanic activity. These grains could be, for example, *glass* soils.

Each soil type has different physical properties. One property of interest in this study is the median grain size of the regolith, which are presented for six Apollo lunar soil samples of different types in

Table 2.2: Median grain size for the characteristic lunar soil types, demonstrated by six Apollo lunar soil samples (Dollfus, 1998).

| Soil type | $d$, μm | Sample id |
|---|---|---|
| glass | 38 | 74220,82 |
| mature | 47 | 72141,1 |
| sub-mature | 78 | 60009,45 |
| sub-mature | 67 | 75081,36 |
| immature | 100 | 71061,1 |
| fresh | 300 | 14141,30 |

Table 2.2. A decreasing median grain size is observed for increasing maturity, which is in accordance with larger comminution of rocks by longer exposure to space weathering.

## 2.2. Lunar Observations

### 2.2.1. Gravimetry from Lunar Orbit

Exploration and mapping of the lunar gravity field began in the 1960s with the *Apollo* missions. By tracking the manned *Apollo* spacecrafts, large positive gravity anomalies were discovered on the lunar surface. These regions of positive gravity anomaly are called ”mascons” (mass concentrations), and were found to be centered on giant impact basins (Hinze et al., 2013). A more detailed gravity field of the Moon was mapped with data of the NASA *Clementine* mission in 1994 and the NASA *Lunar Prospector* mission in 1998 to 1999 (Smith et al., 1997). The *Lunar Prospector* carried a Doppler Gravity Experiment (DPE) instrument which measured the Moon's gravity field. Since this instrument relied on direct line-of-sight Doppler tracking, only the nearside gravity field could be measured (Konopliv et al., 2002).

The gravity field of the lunar farside was still undetermined. Numerical integration of the equations of motion of the spacecraft provided estimates of the farside gravity field, but still uncertainties remained in the estimates. The JAXA *SELENE* mission in 2007 to 2009 significantly improved the gravity field of the lunar farside. The mission featured three separate satellites: the main satellite *Kayuga*; a relay sub-satellite *Okina*; and a Very Long Baseline Interferometry (VLBI) sub-satellite *Ouna*. The relay subsatellites allowed for direct observation of the lunar farside gravity field (Namiki et al., 2009). NASA's *GRAIL* mission is the most recent lunar exploration mission, aiming to further improve the resolution of the gravity field of the Moon (Zuber et al., 2012). *The GRAIL* mission will be presented in Section 3.3, and Section 3.4 will describe the gravimetry data used in this study.

### 2.2.2. Polarimetry from Earth-based Telescopes

No polarimetric measurements from lunar orbit have been done to this day. Recent lunar missions such as NASA *Clementine* (1994-1995), NASA *Lunar Prospector* (1998-1999), ESA *SMART-1* (2003-2006), CNSA *Chang'E* series (2003-present), JAXA *SELENE* (2007-2009), ISRO *Chandrayaan* (2008), and NASA LRO (2009-present) have all made observations of the Moon and made data available for scientific research. However, each mission did not make polarimetric measurements (Jeong et al., 2015). Polarimetric observations have only been done with Earth-based telescopes. Observatories across the globe, such as Paris Observatory, Georgian National Astrophysical Observatory, and Kharkiv Observatory have made ample polarimetric observations of the Moon over many decades (Shkuratov et al., 2011). In Section 4.3 the polarimetric data that is used in this study will be described.

Direct observation of the Moon from Earth is not as straightforward as one might think. A noteworthy aspect to mention is the phases of the Moon. The lunar surface reflects sunlight differently based on the angle between the Sun and a telescope on Earth. This angle is commonly called the phase angle, and reflective properties such as the albedo vary quite a lot with phase angle. For example, if the phase angle is small (near 0°), the majority of the Moon's surface is not illuminated and appears dark. However, if the phase angle is large (near 180°), the Moon is fully illuminated and bright, as presented in Figure 2.3. The change of light behaviour with phase angle is widely used to infer physical properties of the lunar surface (Shkuratov et al., 2011). The phase angle between Sun-Moon-Earth ranges from 0° (New Moon) to 180° (Full Moon).

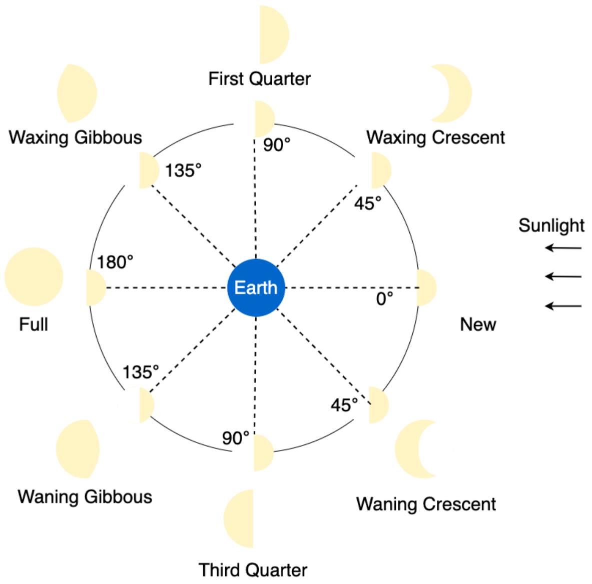
First Quarter
Waxing Gibbous
Waxing Crescent
90°
135°
45°
Sunlight
180°
Earth
0°
Full
New
135°
45°
90°
Waning Gibbous
Waning Crescent
Third Quarter

Figure 2.3: The phases of the Moon as observed from Earth. The angle between the Sun-Moon-Earth line affects observations of the Moon. Figure based on Pogge (2008).

# 3

# Lunar Gravimetry

Gravity studies of an astronomical body are able to reveal its interior structure and dynamic processes. Spatial variations of a gravity field contain information about the planet's topography, internal density distribution, and rotational characteristics. This means that the origin of the gravity signal is complex as it is influenced by numerous factors. A complexity to the interpretation of gravity data is its ambiguous nature, which means that multiple density profiles will result in the same gravity signal. The spherical harmonic representation of a gravity model is a widely used model to express gravity fields of astronomical bodies, and is presented Section 3.1. Next, a brief history of lunar gravimetry is presented in Section 3.2, after which the GRAIL gravity mission is discussed in Section 3.3. Finally, the GRAIL lunar gravity and LRO lunar topography maps are presented in Section 3.4.

This chapter serves as a more thorough introduction to lunar gravimetry. Readers that are solely interested in the research are referred to the manuscript in Part II.

## 3.1. Introduction to Gravity

### 3.1.1. The Gravitational Acceleration

Newton's universal law of gravitation relates the masses of two objects and the distance between them to a resulting attractive force. For example, the gravitational attraction between a mass $M$ and the Moon with mass $M_{\text{Moon}}$ is given by

$$\mathbf{F} = -G\frac{MM_{\text{Moon}}}{\|\mathbf{r}-\mathbf{r_0}\|^2}\hat{\mathbf{r}}', \tag{3.1}$$

where $\mathbf{r}$ is a vector to an arbitrary mass, $\mathbf{r_0}$ the vector to the center of mass of the Moon, and $\hat{\mathbf{r}}'$ is a unit vector in the direction $\mathbf{r}-\mathbf{r_0}$. To simplify this equation, usually the larger mass is placed at the origin as in Figure 3.1, such that $\mathbf{r_0} = \mathbf{0}$, and Equation 3.1 becomes

$$\mathbf{F} = -G\frac{MM_{\text{Moon}}}{r^2}\hat{\mathbf{r}}. \tag{3.2}$$

In Equation 3.2 $G$ is the universal gravitational constant $G = 6.673 \cdot 10^{-11}$ m$^3$ kg$^{-1}$ s$^{-2}$, which is the same for all objects (W.D. McComb, 1999). This quantity is commonly called "big G", in contrast to $\mathbf{g}$,

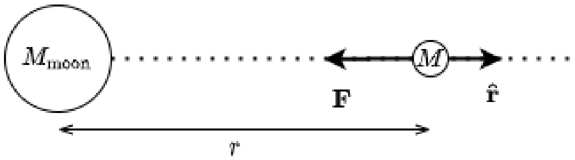

Figure 3.1: Coordinate system where the mass $M$ is positioned at the origin. Figure based on Hilst et al. (2002).

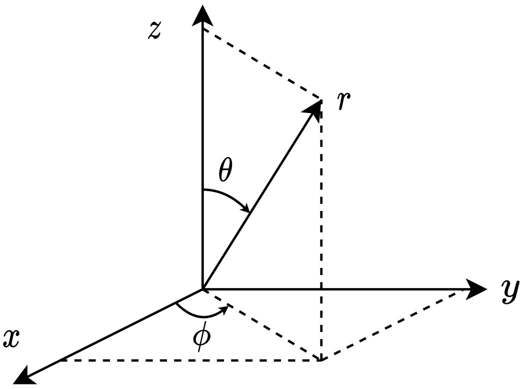

Figure 3.2: Definition of the spherical coordinates $(r, \theta, \phi)$ with respect to the Cartesian coordinates $(x, y, z)$. Figure based on Hilst et al. (2002).

"small g", which is the gravitational *acceleration* (force per unit mass). Using Newton's famous second law of motion Equation 3.2 can be rewritten to

$$\mathbf{F} = M\mathbf{a} = M\mathbf{g} \rightarrow \mathbf{g} = \frac{\mathbf{F}}{M} = -G\frac{M_{\text{Moon}}}{r^2}\hat{\mathbf{r}} = -\frac{\mu}{r^2}\hat{\mathbf{r}} \tag{3.3}$$

where the quantity $\mathbf{g}$ is defined as the gravity field, and $\mu = GM_{\text{Moon}}$ is called the gravitational parameter of the Moon (Hilst et al., 2002). The magnitude of $\mathbf{g}$ varies at each position on the surface of an astronomical body, and is the quantity of interest in studies of a body's gravity field.

Since the gravitational vector force field is conservative, the derivative of the potential with respect to position equals the gravitational acceleration in that direction. Using the potential representation of the gravity field simplifies the analysis since the potential is a scalar quantity, in contrast to acceleration, which is a vector quantity. Therefore potential is independent of direction (Hinze et al., 2013). The gravitational acceleration $\mathbf{g}$ can then be expressed as the gradient of the gravitational potential $U$ as given by

$$\mathbf{g}(\mathbf{r}) \equiv -\nabla U(\mathbf{r}). \tag{3.4}$$

In some literature the minus sign in front of the potential is omitted. Note that both sign conventions are true, depending on the sign used in the potential. The above convention is used since it is common to represent the potential as a potential well (negative) (W.D. McComb, 1999). Since the gravity field is a conservative field only the initial and final position matter. If a particle is placed in a gravity field at position $\mathbf{r}$, then it follows that the initial position $(\mathbf{r_i})$ is at infinity $\infty$ and final position at $\mathbf{r}$. Using the definition of gravitational potential and Equation 3.3 an expression is obtained in

$$U(\mathbf{r}) = \int_{\mathbf{r}_i}^{\mathbf{r}} \mathbf{g}(\mathbf{r}) \cdot \mathrm{d}\mathbf{r} = -\int_{\mathbf{r}_i}^{\mathbf{r}} \frac{\mu}{r'^2}\hat{\mathbf{r}} \cdot \mathrm{d}\mathbf{r} = -\mu \int_{\infty}^{r} \frac{1}{r'^2}\mathrm{d}r' = -\frac{\mu}{r}. \tag{3.5}$$

Returning to Equation 3.5, the gradient operator $\nabla$ depends on the coordinate system. Since this text deals with spherical bodies it is advantageous to use the gradient operator in spherical coordinates $(r, \theta, \phi)$ as displayed in Figure 3.2, where $r$ represents the distance from the center, $\theta$ the co-latitude and $\phi$ the longitude. The gradient operator in spherical coordinates is given by (Adams and Essex, 2016)

$$\nabla = \hat{\mathbf{r}}\frac{\partial}{\partial r} + \hat{\boldsymbol{\theta}}\frac{1}{r}\frac{\partial}{\partial \theta} + \hat{\boldsymbol{\phi}}\frac{1}{r\sin\theta}\frac{\partial}{\partial \phi}. \tag{3.6}$$

In practice the changes in the gravity field are measured as deviations with respect to reference surfaces. Gravity studies thus aim to explain these deviations. These reference surfaces are usually equipotential surfaces of an astronomical body. Gravity measurements can be used for computation of an equipotential surface in the form of a reference spheroid (Hilst et al., 2002). An example of an equipotential surface is the sea level of Earth, also called the geoid (Lissauer and Pater, 2013).

A note should be made on how to express a gravity contribution. Looking at Equation 3.3, the magnitude of $\mathbf{g}$ is the varied quantity over the surface of an astronomical body, and has units ms$^{-2}$ in S.I. units. In honor of astronomer and physicist Galileo Galilei the unit of gravitational acceleration is often expressed in *Gal*. 1 Gal equals 10$^{-2}$ ms$^{-2}$. To get a feel for the numbers, Earth's gravitational acceleration is approximately 9.8 ms$^{-2}$, which corresponds to 980 Gal. Since gravity anomalies are small, they are often expressed in *milliGal*: 1 mGal = $10^{-3}$ Gal = $10^{-5}$ ms$^{-2}$.

### 3.1.2. Gravity Ambiguity

It could be the case that studies into the *internal* density distribution are desired. However, in practice the gravitational acceleration can only be measured at, or above, the surface of an astronomical body. Gauss's Theorem provides a relationship between any observable $\mathbf{T}$ at a surface to the volume of the enclosed body, and can thus be used to study a volume. More precisely, Gauss's Theorem relates a volume integral to a surface integral. Gauss's Theorem is given by

$$\int_V \nabla \cdot \mathbf{T} \, \mathrm{d}V = \int_S \hat{\mathbf{n}} \cdot \mathbf{T} \, \mathrm{d}S, \tag{3.7}$$

for a body with volume $V$ bounded by its surface $S$ (Hilst et al., 2002). Applying Gauss's Theorem to the measured gravity field $\mathbf{g}(\mathbf{r})$ everywhere on the surface, and knowing that the gravity potential is a scalar potential field:[1]

$$\int_S \hat{\mathbf{n}} \cdot \mathbf{g}(\mathbf{r}) \, \mathrm{d}S = \int_V \nabla \cdot \mathbf{g}(\mathbf{r}) \, \mathrm{d}V = -\int_V \nabla \cdot \nabla U(\mathbf{r}) \, \mathrm{d}V = -\int_V \nabla^2 U(\mathbf{r}) \, \mathrm{d}V. \tag{3.8}$$

Now, assuming a spherical surface $S$,[2] the gravitational acceleration only has a nonzero component in the direction normal to the surface and therefore $\hat{\mathbf{n}} \cdot \mathbf{g}(\mathbf{r}) = -g$. Now substituting Equation 3.3 in the right hand side of Equation 3.7 results in

$$\int_S \hat{\mathbf{n}} \cdot \mathbf{g}(\mathbf{r}) \, \mathrm{d}S = -\int_S g \, \mathrm{d}S = -g \int_S \mathrm{d}S = -\frac{GM}{r^2} 4\pi r^2 = -4\pi GM, \tag{3.9}$$

where the total mass of the body is equal to the integral of the density over the whole volume $V$ expressed by

$$M = \int_V \rho(\mathbf{r}) \, \mathrm{d}V. \tag{3.10}$$

Substituting the expression for the total mass Equation 3.10 in Equation 3.9 results in

$$\int_S \hat{\mathbf{n}} \cdot \mathbf{g}(\mathbf{r}) \, \mathrm{d}S = -4\pi G \int_V \rho(\mathbf{r}) \, \mathrm{d}V. \tag{3.11}$$

Comparing Equation 3.8 and Equation 3.11 it is observed that the following quantities must be equal:

$$\nabla^2 U(\mathbf{r}) = 4\pi G \rho(\mathbf{r}), \tag{3.12}$$

which is known as Poisson's equation. In the homogeneous case ($\rho(\mathbf{r}) = 0$) Poisson's equation reduces to Laplace's equation

$$\nabla^2 U(\mathbf{r}) = 0. \tag{3.13}$$

In other words, Poisson's equation is valid for potential fields *inside* the source of the field, whereas Laplace's equation is valid for potential fields *outside* the source of the field.

Poisson's equation and Laplace's equation are relevant for the analysis of gravity fields because these equations provide insight into the properties of gravity field measurements. Equation 3.12 implies that the measured gravity field is independent of the distribution of the density $\rho(\mathbf{r})$ inside the volume $V$. In other words, for a given measurement there exist multiple density distributions that suffice the observation. This is the ambiguity nature of gravity data.

---

[1] Note that this only works for scalar potentials. For a vector potential $\mathbf{V}$: $\nabla^2 \mathbf{V} = \nabla(\nabla \cdot \mathbf{V}) - \nabla \times (\nabla \times \mathbf{V})$ (Adams and Essex, 2016).

[2] This derivation will work for any arbitrary enclosing surface (Hilst et al., 2002).

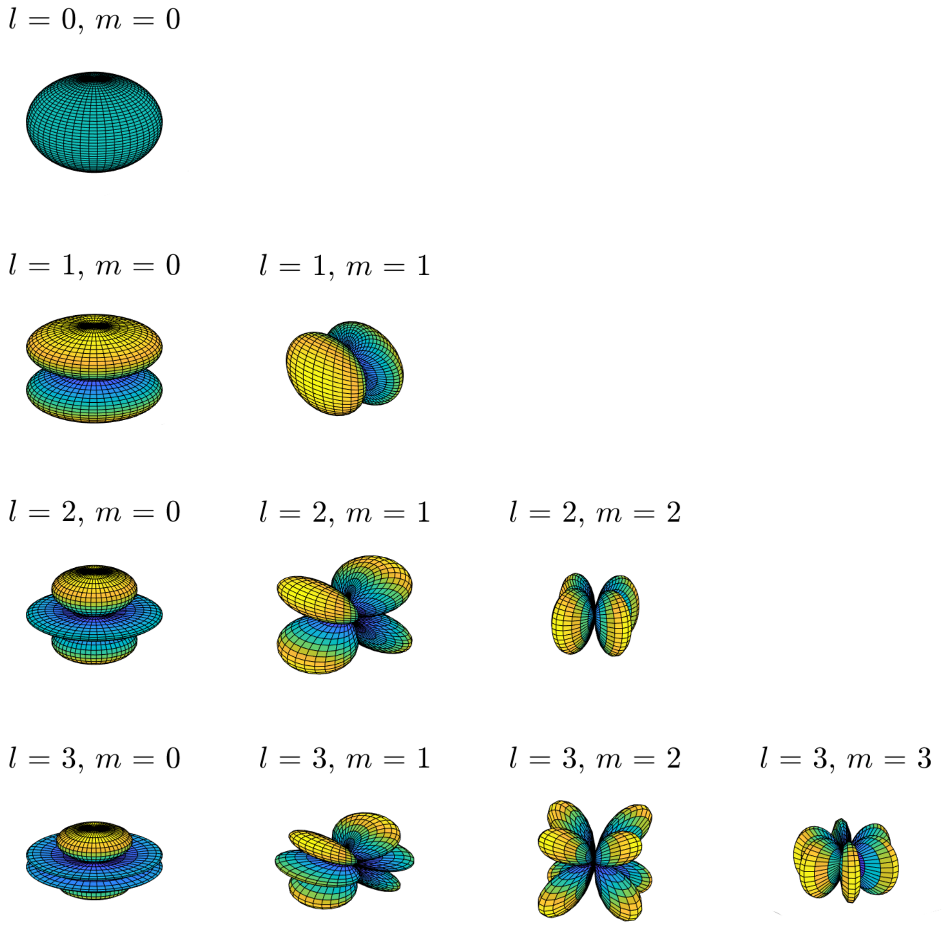

Figure 3.3: Visualisation of the spherical harmonics up to degree and order 3. Figure based on Hilst et al. (2002).

### 3.1.3. Spherical Harmonic Gravity

Solving Laplace's equation (Equation 3.13) in spherical coordinates result in spherical harmonics as a solution (Hilst et al., 2002). Since Laplace's equation is a differential equation the general solution will be in the form of a linear combination of exponentials, where each term comes with a weight factor (Adams and Essex, 2016). It turns out that for Cartesian coordinates this series solution are known as Fourier series (Hilst et al., 2002). This theory states that a signal can be represented as a superposition of exponentials ($\sin$ and $\cos$ functions). Thus, analogously to Fourier series, a superposition of spherical harmonics is able to represent any observable on the surface of a sphere, which in this text is an astronomical body.

The full solution of Laplace's equation can be found by using separation of variables, which means that the gravitational potential field is split into a product of three terms which each depend on a single three spherical coordinates $r$, $\theta$ and $\phi$, respectively. The solution is then given by

$$U(\mathbf{r}) = \frac{GM}{r} \sum_{l=0}^{\infty} \sum_{m=0}^{l} \left(\frac{R}{r}\right)^{l} \bar{P}_{l,m}^{\mathrm{leg}}(\cos\theta)\left(\bar{C}_{l,m}\cos m\phi + \bar{S}_{l,m}\sin m\phi\right), \tag{3.14}$$

where the integers $l$ and $m$ are the so-called degree and order of the spherical harmonic, respectively. $R$ is the reference radius of the astronomical body. $\bar{P}_{l,m}^{\mathrm{leg}}$ are the normalized associated Legendre polynomials of degree $l$ and order $m$. Finally $\bar{C}_{l,m}$ and $\bar{S}_{l,m}$ are the normalized spherical harmonic coefficients of order $l$ and degree $m$ (Hilst et al., 2002). These coefficients define the contribution of a latitudinal and longitudinal factor to the total gravitational potential field, and are thus what describe an observable of an astronomical body. In order to gain understanding of the above equation, it is perhaps useful to visualise the spherical harmonics, which is done in Figure 3.3.

When carefully looking at the visualization of the spherical harmonics (Figure 3.3), three types of spherical harmonics can be identified based on the degree $l$ and order $m$ (Wieczorek, 2015).

First, the *zonal harmonics* are defined to be $m = 0$. Applying this definition to Equation 3.14 results in

$$U(\mathbf{r}) = \frac{GM}{r} \sum_{l=0}^{\infty} \left(\frac{R}{r}\right)^{l} \bar{P}_{l,0}^{\mathrm{leg}}(\cos\theta)\bar{C}_{l,0} \tag{3.15}$$

where it can be seen that there is only a dependency on latitude (co-latitude $\theta$) and no dependency on longitude $\phi$. These harmonics thus divide a sphere into latitudinal zones (hence the name). It can also be seen from Equation 3.15 that the $\bar{S}_{l,m}$ are undefined for the zonal harmonics as $\sin m\phi = 0$ for $m = 0$. Zonal harmonic coefficients are often noted as $J_l$ such as the $J_2 = -\bar{C}_{2,0}$ coefficient, which is a measure of the flattening of an astronomical body (Lissauer and Pater, 2013).

Second, the *sectorial harmonics* have $2m$ zero crossings in longitudinal direction. In other words they divide a sphere into longitudinal sectors. These harmonics are defined to $l = m$.

Finally, the *tesseral harmonics* have $2m$ zero crossings in longitudinal direction and $(l - m)$ zero crossings in latitudinal direction. They contain all other harmonics $(l \neq m)$.

The spherical harmonic representation of the gravitational potential field (Equation 3.14) has three terms, each depending on a separate spherical coordinate.

First, the radial dependency in the form of $\sim r^{-(l+1)}$ implies that the larger the distance from the source the spherical harmonics with low degree become more dominant. Since the degree is directly related to the amount of detail that can be observed (see Figure 3.3), it can be interpreted as an attenuation factor depending on the radius and degree. The radial dependency has direct effect on the resolution of the gravity field which is correlated with the degree of the potential field (Hilst et al., 2002).

Second, the longitudinal dependency is in the form of a linear combination of exponentials ($\cos$ and $\sin$) with a weight given by the spherical harmonic coefficients $\bar{C}_{l,m}$ and $\bar{S}_{l,m}$ and the period influenced by the order $m$. These coefficients are what define the deviations from a perfectly spherical symmetric gravity field (Hilst et al., 2002). When $l = 0$ (zero order) Equation 3.14 reduces to

$$U(\mathbf{r}) = -\frac{GM}{r}, \tag{3.16}$$

and represents a spherically symmetric harmonic (see Figure 3.3 for $l = 0$, $m = 0$). Note that Equation 3.16 is identical to Equation 3.5 valid for a point mass gravitational source.

Finally, the latitudinal dependency is in the form of the normalized associated Legendre polynomials with argument $\cos\theta$: $\bar{P}_{l,m}^{\mathrm{leg}}(\cos\theta)$, which are the direct result of solving Laplace's equation (Equation 3.13 in spherical coordinates. The behaviour of these polynomials is summarized in an expression, given by (Wieczorek, 2015)

$$\bar{P}_{l,m}^{\mathrm{leg}}(x) = \sqrt{(2-\delta_{0m})(2l+1)\frac{(l-m)!}{(l+m)!}} P_{l,m}(x) \tag{3.17}$$

$$P_{l,m}^{\mathrm{leg}}(x) = (1-x^2)^{m/2}\frac{\mathrm{d}^m}{\mathrm{d}x^m}P_l(x) \tag{3.18}$$

$$P_l^{\mathrm{leg}}(x) = \frac{1}{2^l l!}\frac{\mathrm{d}^l}{\mathrm{d}x^l}(x^2-1)^l \tag{3.19}$$

The associated Legendre polynomials with argument $\cos\theta$ are visualised in Figure 3.4 up to degree and order 2. It can be seen that for the associated Legendre polynomials with $l \neq m$ there are $(l - m)$ zero crossings, corresponding to the sectorial harmonics.

## 3.2. A Brief History of Lunar Gravimetry

Exploration and mapping of the lunar gravity field began in the 1960s with the *Apollo* missions. By tracking the manned *Apollo* spacecrafts, large positive gravity anomalies were discovered on the lunar surface. These regions of positive gravity anomaly are called ”mascons” (mass concentrations), and were found to be centered on giant impact basins (Hinze et al., 2013).

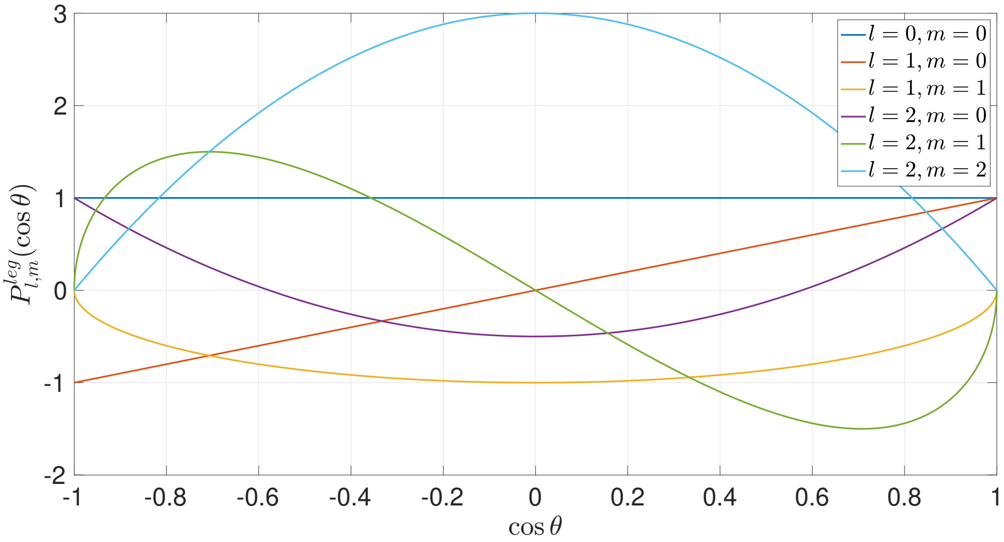

Figure 3.4: Associated Legendre polynomials with argument $\cos\theta$ up to degree and order 2. Figure based on Hilst et al. (2002).

A more detailed gravity field of the Moon was mapped with data of the NASA *Clementine* mission in 1994 and the NASA *Lunar Prospector* mission in 1998 to 1999. The *Clementine* mission carried a laser altimeter and measured the Moon's topography to an accuracy of 100m (Smith et al., 1997). The *Lunar Prospector* carried a Doppler Gravity Experiment (DPE) instrument which measured the Moon's gravity field. Since this instrument relied on direct line-of-sight Doppler tracking, only the nearside gravity field could be measured. Both the topography data of *Clementine* and gravity data of *Lunar Prospector* resulted in the LP165P gravity field model of the Moon to degree and order (D/O) 165 (Konopliv et al., 2002).

The gravity field of the lunar farside was still undetermined. Numerical integration of the equations of motion of the spacecraft provided estimates of the farside gravity field, but still uncertainties remained in the estimates. The JAXA *SELENE* mission in 2007 to 2009 significantly improved the gravity field of the lunar farside. The mission featured three separate satellites: the main satellite *Kayuga*; a relay sub-satellite *Okina*; and a Very Long Baseline Interferometry (VLBI) sub-satellite *Ouna*. The relay sub-satellites allowed for direct observation of the lunar farside gravity field, up to D/O 100 (Namiki et al., 2009).

NASA's *GRAIL* mission is the most recent lunar exploration mission, aiming to further improve the resolution of the gravity field of the Moon. Since its launch in 2011 it has enabled global gravity field models of the Moon up to D/O 1500 (Goossens et al., 2020, Zuber et al., 2012). The *GRAIL* mission is presented in section 3.3.

The data of *GRAIL* have resulted in gravity field models of the Moon increasing in D/O with time, since more data could be used to construct models as time passed. Zuber et al. (2013) published an initial D/O 420 model of the Moon's gravity field called GL0420A. M. Zuber and D. Smith are affiliated with Massachusetts Institute of Technology (MIT) in Cambridge, Massachusetts in the United States. With an accuracy of 30 by 30 km at the Moon's equator, these initial mission results provided information about the lunar crust (Wieczorek et al., 2013), which in turn could be used for the Moon's chemical composition (Goossens et al., 2020).

Two separate research groups analysed *GRAIL*'s data and subsequently determined gravity models of the Moon independently, while cross-validating their results. One group was affiliated with the Jet Propulsion Laboratory (JPL) in Pasadena, California, in the United States, and one group was affiliated with Goddard Space Flight Center (GSFC) in Greenbelt, Maryland, in the United States. In addition to these groups, independent researchers from MIT, such as M. Zuber and D. Smith, aided in analysis of the GRAIL and development of lunar gravity field models. Researchers from the GSFC group are S. Goossens, T. Sabaka, G. Neumann, E. Mazarico, F. Lemoine and J. Nicholas. Lemoine et al. (2014) published two D/O 900 model called GRGM900B and GRGM900C, with most recent models of D/O 1200 by Goossens et al. (2020) called GRGM1200A, GRGM1200B, and GRGM1200C. Researchers from the JPL group are R. Park, A. Konopliv, D. Yuan, S. Asmar, M. Watkins and J. Williams. Data from the PM resulted in a D/O 660 model published by Konopliv et al. (2013) called GL0660B. Supplementary from the XM resulted in two D/O 900 models published by Konopliv et al. (2014) called GL0900C and GL0900D, followed by a D/O 1500 model published in 2016 by Park et al. (2015).

The high-resolution global gravity field models from GRAIL, with a spatial resolution of approximately 5 km, enabled many studies on the Moon's interior. These studies can be distinguished in crustal studies and deep interior studies. Crustal studies involve determining the density and porosity of the crust at global and local scale, as well as determining the structure of impact basins or mare regions (Goossens et al., 2020).

Key studies into the density and porosity structure of the Moon are Wieczorek et al. (2013), Besserer et al. (2014), Jansen et al. (2017), and Goossens et al. (2020). It is perhaps good to list the affiliations of aforementioned authors. M. Wieczorek is affiliated with Observatoire de la Côte d'Azur in Nice, France, J. Besserer is affiliated with University of California in the United States, J. Jansen and G. Goossens are affiliated with NASA GSFC.

## 3.3. The Gravity Recovery and Interior Laboratory (GRAIL) Mission

The *GRAIL* mission features two twin spacecraft: *GRAIL* A (*Ebb*) and *GRAIL* B (*Flow*). Each spacecraft has a Lunar Gravity Ranging System (LGRS), and measures the *change* in distance between *Ebb* and *Flow* as they orbit the Moon. As the spacecraft fly over the lunar surface, their motion is influenced by various external accelerations. These accelerations include gravitational accelerations, as well as non-gravitational accelerations, such as solar radiation pressure and relativistic effects. Carefully correcting for non-gravitational accelerations[3] will reveal the gravitational accelerations, which in turn can be used to construct the gravity field (Zuber et al., 2013).

The mission has been developed with heritage from the Gravity Recovery and Climate Experiment (*GRACE*) mission, also spacecraft-to-spacecraft tracking mission. The *GRACE* mission was launched in 2002, and made detailed measurements of Earth's gravitational field as a function of time, allowing scientists to study the changing Earth due to climate change (Tapley et al., 2004).

*GRAIL* consisted of two mission phases. The Primary Mission (PM) lasted from March 1 until May 29, 2012, where the spacecraft flew at a mean altitude of 55 km above the lunar surface, with a lower bound of ~20 km (Goossens et al., 2020). During the PM, the distance between *Ebb* and *Flow* varied between 82 and 218 km, providing a wide range of wavelength sensitivities of the lunar gravity field (Zuber et al., 2012). The Extended Mission (XM) followed the PM and lasted from August 30 until December 14, where the spacecraft flew at a mean altitude of 23 km above the lunar surface, with a lower bound of ~11 km (Goossens et al., 2020).

## 3.4. Lunar Gravity and Topography

The global gravity and topography are better known for the Moon than for any other solar system body, including Earth (Wieczorek, 2015). The GRAIL (Section 3.3) mission has enabled global gravity field models of the Moon up to spherical harmonic degree and order (D/O) 1500 (Park et al., 2015). The most recent models, called GRGM1200B, are of D/O 1200 and are substantially more stable over their entire degree range and show less noise for degrees greater than 600, in contrast to the D/O 1500 model. The GRGM1200B models have been subjected to a constraint based on topography, called the RM1 (rank-minus-one) constraint, and have a weigh factor $\lambda_{\mathrm{RM1}}$ that indicates how strongly the RM1 constraint is applied (Goossens et al., 2020). In the manuscript (Part II) the GRGM1200B model is used to determine the density structure of the Moon's crust.

The power spectra for GRGM1200B RM1 $\lambda_{\mathrm{RM1}} = 10$ spherical harmonics model are presented in Figure 3.5. It is observed in Figure 3.5a that the error does not cross the observed spectrum, which means that the higher degrees are not dominated by noise. Furthermore, the two-dimensional power spectrum in Figure 3.5b is free of major correlations, except for the two lower power arches for degrees $100 \leq l \leq 500$, which could be due to the orbit mismatches of the GRAIL satellites. Finally, in both power spectra there is a small jump around $l = 600$, which is due to the RM1 constraint being applied for degrees larger than 600 (Goossens et al., 2020)

The global free-air anomaly of the Moon from the GRAIL GRGM1200B RM1 $\lambda_{\mathrm{RM1}} = 10$ spherical

---

[3] Of course, gravitational forces of *other* astronomical bodies should also be corrected for.

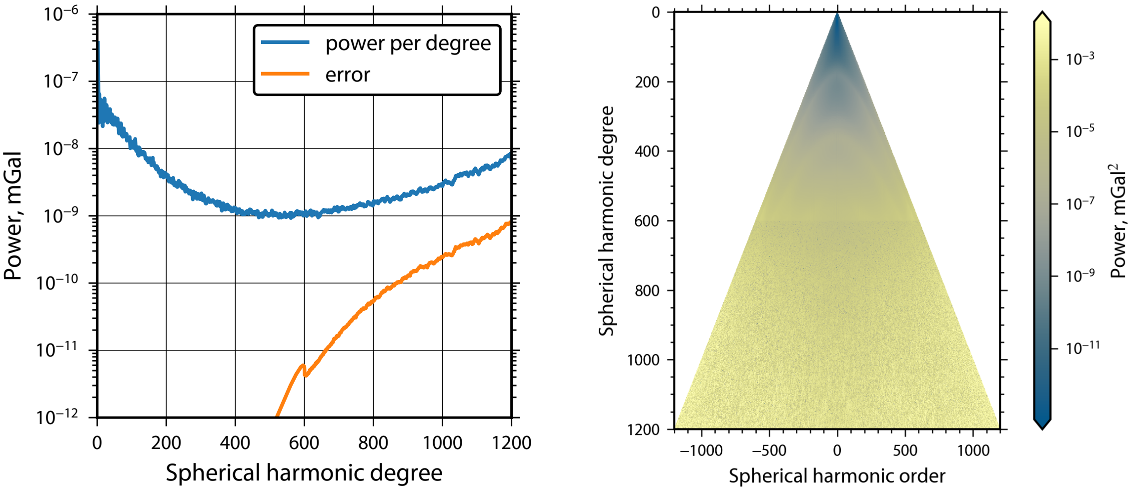

(a)

(b)

Figure 3.5: One- and two-dimensional power spectra for the GRGM1200B $\lambda_{\mathrm{RM1}} = 10$ spherical harmonics model

harmonic model is presented in Figure 3.6. One of the major features of this map are the large positive gravity anomalies on the nearside related to the impact basins, informally called 'mascons' (mass concentrations) (Neumann et al., 2015), surrounded by negative gravity anomaly canals.

The Lunar Orbiter Laser Altimeter (LOLA) onboard the LRO mission has enabled the most recent and most accurate lunar topography models (Smith et al., 2010). The LOLA2600p is a spherical harmonic model of the lunar surface topography expressed in principal-axis coordinates, and is presented in Figure 3.7 where it is referenced to the GRAIL lunar geoid presented in Figure 3.8. One of the major features of the surface topography map is the South Pole-Aitken (SPA) impact basin on the farside. With a diameter greater than 2000 km, and depth relative to its surroundings of 10 km, it is the largest known impact basin in the solar system (Moriarty III and Pieters, 2018). The total range of the surface topography is slightly less than 20 km, whereas the total range of the lunar geoid is more than 1 km, a factor 5 times greater than Earth's geoid (Wieczorek, 2015).

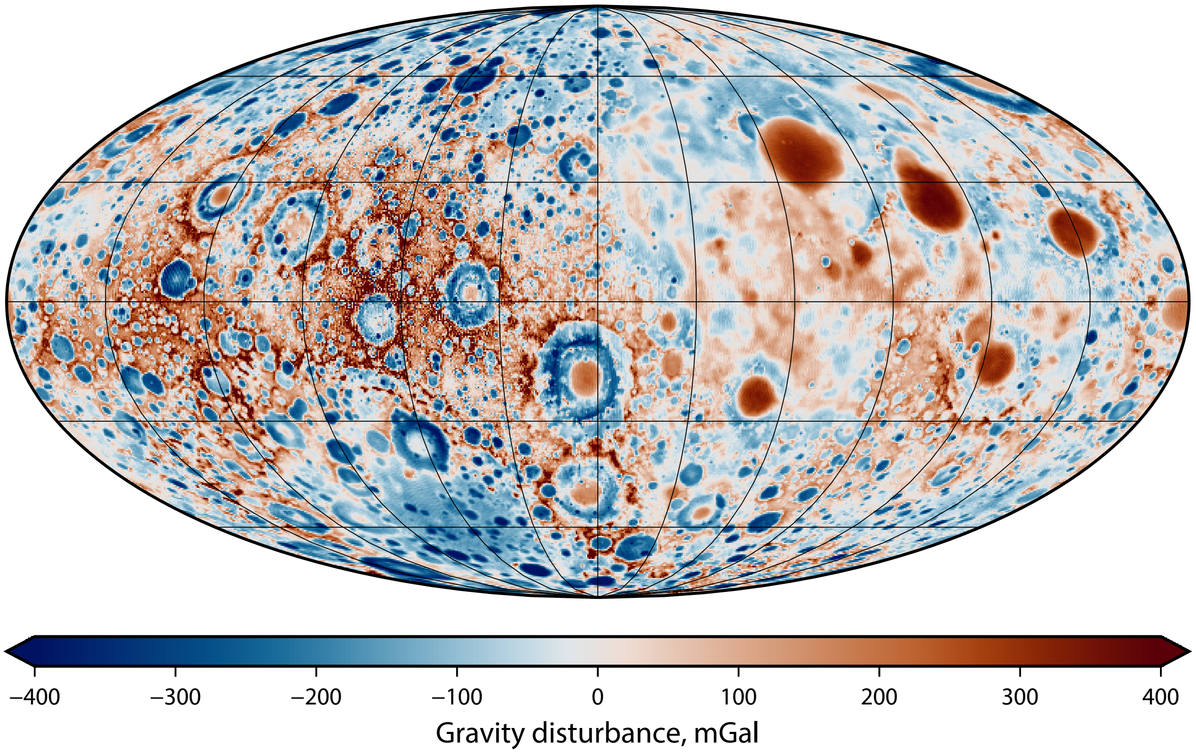
−400
−300
−200
−100
0
100
200
300
400
Gravity disturbance, mGal

Figure 3.6: Global free-air anomaly of the Moon from the GRAIL GRGM1200B RM1 $\lambda_{\mathrm{RM1}} = 10$ spherical harmonic model. The map is presented in a Mollweide equal area projection centered on 270°E longitude and show the farside on the left and nearside on the right.

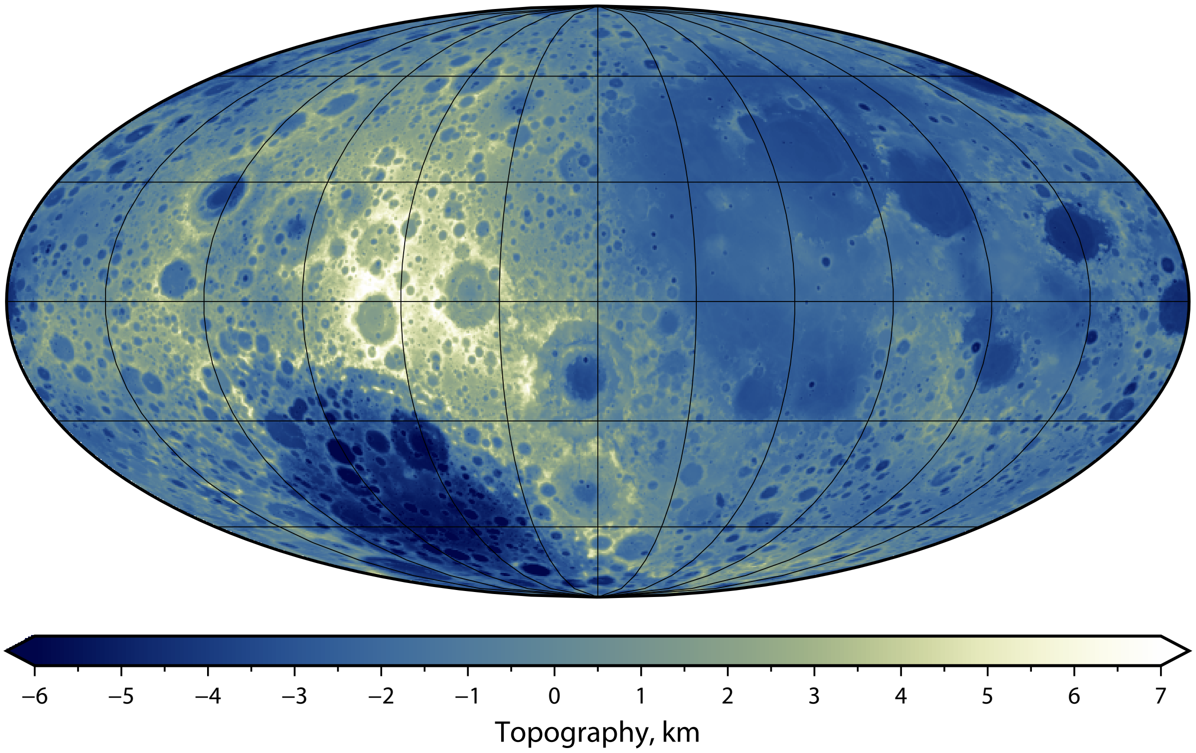
−6
−5
−4
−3
−2
−1
0
1
2
3
4
5
6
7
Topography, km

Figure 3.7: Global surface topography of the Moon from the LOLA2600p spherical harmonic model, referenced to the GRGM1200B $\lambda_{\mathrm{RM1}} = 10$ lunar geoid. The map is presented in a Mollweide equal area projection centered on 270°E longitude and show the farside on the left and nearside on the right.

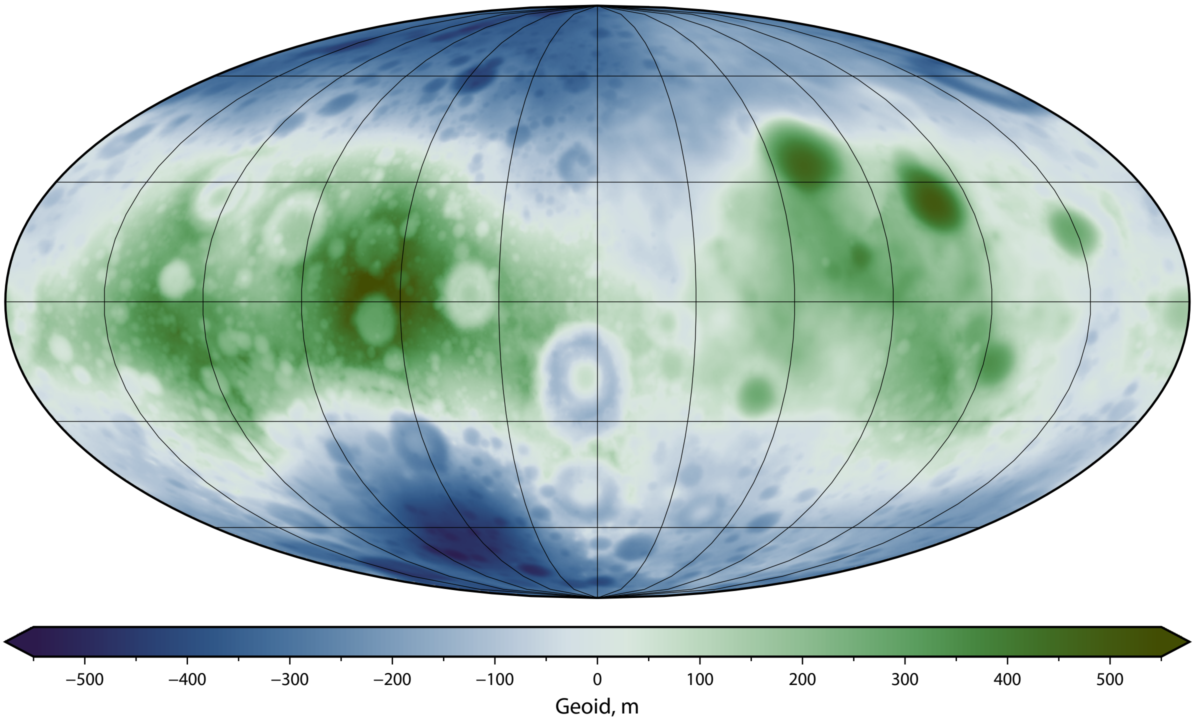
−500
−400
−300
−200
−100
0
100
200
300
400
500
Geoid, m

Figure 3.8: Global lunar geoid from the GRAIL GRGM1200B RM1 $\lambda_{\mathrm{RM1}} = 10$ spherical harmonic model. The map is presented in a Mollweide equal area projection centered on 270°E longitude and show the farside on the left and nearside on the right.

# 4

# Lunar Polarimetry

For a very long time astronomers have studied astronomical bodies using light. In the 18th and 19th centuries the observations were done with the human eye. Since the late 1890s photographic plates made it possible to physically store images. In the 1970s the CCD detector allowed for digital storage and was the beginning of modern astronomy we know today (Karttunen, 2007).

Since then, the inspection of astronomical bodies has been expanded from visible light to the entire electromagnetic spectrum. Based on the wavelength used for an observation, different characteristics of the body are revealed, and many different techniques exist for subsequent analysis. In this work a focus is placed on the *polarimetry* technique.

Polarimetry is the measurement and interpretation of the *polarisation state* of light. Interaction of light with an (astronomical) object will leave a polarisation ”footprint” in the scattered light, which can be studied to deduce information about the surface of the object (Ishiguro et al., 2017). An introduction to polarisation of light is discussed in Section 4.1. The scattered light from the Moon’s surface is completely described by the Stokes parameters, which are also discussed in Section 4.1. Next, a brief history of polarimetry is presented in Section 4.2. Finally, Section 4.3 presents the multi-band polarimetric observations used in this work.

This chapter serves as a more thorough introduction to lunar polarimetry. Readers that are solely interested in the research are referred to the manuscript in Part II.

## 4.1. Introduction to Polarisation

### 4.1.1. Polarisation of Light

Electromagnetic waves describe the behaviour of light. An electromagnetic wave is made up of an electric field $\mathbf{E}$ and a magnetic field $\mathbf{H}$, both oscillating in time. The electric field vector and magnetic field vector are perpendicular to the direction of propagation, as well as each other. These waves are usually expressed in flux ($\mathrm{Wm}^{-2}$) (Stinson, 2016). With this knowledge, the *polarisation is defined to be the direction of the electric field vector* (Hecht and Zajac, 2013).

In order to understand the concept of polarisation, it is perhaps good to start with a practical example. One of the most popular involvements of polarisation is the three-dimensional experience in the cinema. The illusion of a three-dimensional movie is created by wearing three-dimensional glasses. The two lenses in these glasses are essentially polarisation filters, meaning that each lens transmits a different polarisation state. The movie on the screen is transmitted in two different polarisations, each illuminating the movie subject from a slightly different direction. By wearing the three-dimensional glasses, each eye thus sees a slightly different image, creating the perception of a three-dimensional movie.

Light is either unpolarised or polarised, and different types of polarisation exist (Hecht and Zajac, 2013). First of all, *unpolarised light* means that the probability of the direction of the electric field is equal in all directions. Unpolarised is ”broken” into polarised light by interaction with objects. This interaction is formally called scattering. Unpolarised light is also called natural light. An example of unpolarised light is sunlight (Stinson, 2016).

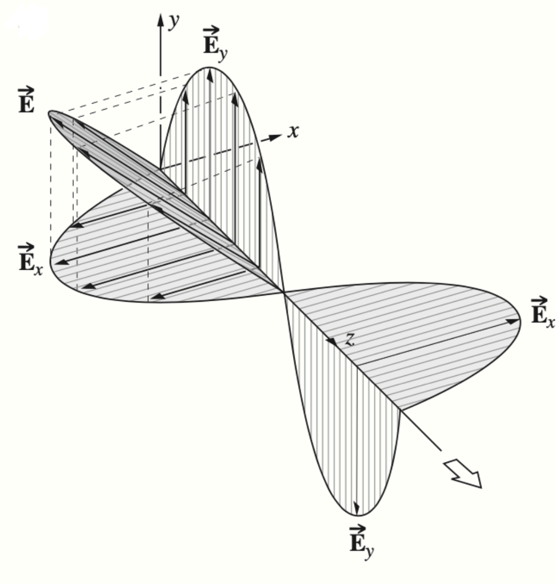

Figure 4.1: Linear polarised light. The electromagnetic wave propagated in the $z$-direction, and the linear polarised light is in the second and fourth quadrants. The magnetic field is not displayed for better interpretability (Hecht and Zajac, 2013).

Second, *linearly polarised light* has an electric field vector with a constant direction. This direction can be arbitrary, as long as its direction is constant with time. Figure 4.1 displays the electric field of linearly polarised light. Note that the magnetic field is not displayed for better interpretability.

Third, *circularly polarised light* has an electric field vector whose direction changes with time. The electric field rotates around the direction of propagation with a constant magnitude. Two distinctions are made: right-circular and left-circular polarised light. The electric field of right-circular polarised light rotates clockwise, and vice-versa for left-circular polarised light.

Finally, *elliptically polarised light* also has an electric field vector whose direction changes with time. In contrast to circular polarised light, the amplitude of the electric field does change with time. The endpoint of **E** will, therefore, trace out an ellipse with time. Linear- and circular polarised light are thus ”special” cases of elliptical polarised light.

### 4.1.2. The Stokes Parameters

Up until this point, polarisation has been treated in terms of the direction of the electric field vector $\mathbf{E}$ of the light wave. Four types of polarisation have been distinguished, with elliptical polarised light being the most general. A mathematical description of the polarisation state of a wave can be described by the four Stokes parameters, introduced by G. G. Stokes in 1852 (McMaster, 1954). The four Stokes parameters are represented by the symbols $I$, $Q$, $U$ and $V$.

Since the definition of the Stokes parameters is dependent on the direction of propagation, a preliminary choice for a reference direction is required. For astronomy observations the reference direction is usually the great circle passing through the celestial sphere and the astronomical body of interest (Stinson, 2016). Many great circles suffice this criteria, but in polarimetry observations it is conventional to pick the great circle passing through the Sun and astronomical body of interest (Landi Degl’Innocenti, E. and Bagnulo, S. and Fossati, L. , 2007).

In a right handed reference system $(x, y, z)$ the $x$-axis is then along the reference direction, and the $z$-axis along the direction of propagation, as displayed in Figure 4.1. Following from the Maxwell equations, the electric field component of the light wave lies in the $(x, y)$ plane, meaning it is fully described by its components in the $x$- and $y$-direction at a fixed point in space[1], as a function of time: $E_x(t)$ and $E_y(t)$, respectively (Griffiths, 2013). The Fourier analogues $\mathcal{E}_x(\omega)$ and $\mathcal{E}_y(\omega)$ for these components are calculated using the usual definition of the Fourier transform (Oppenheim et al., 1996),

---

[1] A fixed point in space can be, for example, the entrance point of an Earth-based telescope.

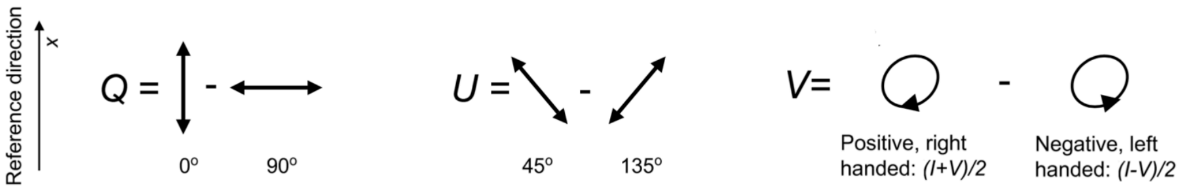
Reference direction
x
Q =
-
0°
90°
U =
-
45°
135°
V=
-
Positive, right handed: (I+V)/2
Negative, left handed: (I-V)/2

Figure 4.2: Visualisation of the physical properties of Stokes parameters $Q$, $U$, and $V$. Stokes $I$ is the total intensity of the wave. The direction of the source is into the paper (Landi Degl'Innocenti, E. and Bagnulo, S. and Fossati, L. , 2007).

$$\begin{aligned}
\mathcal{E}_x(\omega) &= \int_{-\infty}^{\infty} E_x(t)\exp\left(-i\omega t\right)\,\mathrm{d}t,\\
\mathcal{E}_y(\omega) &= \int_{-\infty}^{\infty} E_y(t)\exp\left(-i\omega t\right)\,\mathrm{d}t.
\end{aligned} \tag{4.1}$$

The four Stokes parameters are then described by

$$\begin{aligned}
I(\omega) &= \kappa\left\{\langle\mathcal{E}_x(\omega)^*\mathcal{E}_x(\omega)\rangle + \langle\mathcal{E}_y(\omega)^*\mathcal{E}_y(\omega)\rangle\right\},\\
Q(\omega) &= \kappa\left\{\langle\mathcal{E}_x(\omega)^*\mathcal{E}_x(\omega)\rangle - \langle\mathcal{E}_y(\omega)^*\mathcal{E}_y(\omega)\rangle\right\},\\
U(\omega) &= \kappa\left\{\langle\mathcal{E}_x(\omega)^*\mathcal{E}_y(\omega)\rangle + \langle\mathcal{E}_y(\omega)^*\mathcal{E}_x(\omega)\rangle\right\},\\
V(\omega) &= \kappa\left\{\langle\mathcal{E}_x(\omega)^*\mathcal{E}_y(\omega)\rangle - \langle\mathcal{E}_y(\omega)^*\mathcal{E}_x(\omega)\rangle\right\},
\end{aligned} \tag{4.2}$$

where $\kappa$ is a positive constant, $\langle\ldots\rangle$ means the expectation value and the symbol $*$ means complex conjugate. It should be noted that this definition only holds for the right handed reference system. Using a left handed reference system, the signs of Stokes $U$ and $V$ will change (Landi Degl'Innocenti, E. and Bagnulo, S. and Fossati, L. , 2007).

According to Equation 4.2, the physical interpretation of the Stokes parameters is visualized in Figure 4.2 and can be described as follows. Stokes $I$ is the total intensity of the wave. Stokes $Q$ is the difference in the amount of photons for which the electric field oscillates in the $x$-direction and in the perpendicular $y$-direction. It is therefore a measure of tendency of light to be linearly polarised relative to the reference direction. Stokes $U$ is the difference in the amount of photons for which the electric field oscillates at 45°and at 135°, where the angles are measured counterclockwise with respect to the reference direction $x$. Both Stokes $Q$ and $U$ define the orientation of the polarisation plane through $1/2\cdot\arctan U/Q$. Finally, Stokes $V$ is the difference between right handed circular polarisation and left handed circular polarisation (Shkuratov et al., 2015, Stinson, 2016).

The principle source of knowledge of the lunar surface is captured in Stokes $I$. Stokes $Q$ aids in analysing the lunar surface structure. This parameter has been neglected for a long time, but becomes increasingly popular in lunar polarimetry (Bowell and Zellner, 1974). Stokes $U$ indicates the degree of symmetry in the surface structure. Finally, Stokes $V$ is not related to physical properties, but instead to geometrical factors of the lunar surface. Stokes $V$ is too small and appears not to be useful for lunar polarimetry (Banderman et al., 1972, Jeong et al., 2015).

Thus, only Stokes $I$, $Q$, and $U$ appear to be relevant for lunar polarimetry. In practice, the latter two are combined and subsequently normalised by the total intensity Stokes $I$, expressed as the polarisation degree $P$ as given by (Jeong et al., 2015),

$$P = \frac{\sqrt{Q^2+U^2}}{I}, \tag{4.3}$$

meaning that the value of the positive constant $\kappa$ remains undefined when considering the relative Stokes parameters (Shkuratov et al., 2015).

## 4.2. A Brief History of Lunar Polarimetry

Lunar polarimetry was performed for the first time in the nineteenth century by French astronomer F. Arago. Early studies of the polarisation have not resulted in significant discoveries, albeit the large amplitude of polarisation signal. However, the paper published by another French astronomer Lyot

Table 4.1: The four bands and their corresponding central wavelength of the polarimetric observations carried out by Jeong et al. (2015).

| Band | Central wavelength, nm | Part of spectrum |
|---|---|---|
| U | 373.8 | Ultraviolet |
| B | 443.5 | Blue |
| V | 558.6 | Visible |
| R | 676.3 | Red |

(1929) has laid the foundations of planetary polarimetry and is, even nowadays, often cited. The works of his disciple A. Dollfus are also very important works for planetary polarimetrists (Shkuratov et al., 2015). Both of these astronomers were affiliated with the Paris Observatory.

Polarimetric measurements come in two varieties: discrete and imaging polarimetry. Discrete polarimetry are measurements of selected target sites, whereas imaging polarimetry are measurements of distributions of polarimetric parameters.

Due to lunar sample return missions, discrete lunar polarimetry studies became popular in the 1970s. A detailed study of polarimetric parameters of the lunar surface has been reported by Dollfus and Bowell (1971), made available by the new polarimeters at Paris Observatory. In the 1980s, Kvaratskhelia (1988), affiliated with Georgian National Astrophysical Observatory, presented the results of polarimetric investigations of 100 regions on the lunar surface in combination with investigations of 21 lunar soil samples returned by the *Luna* and *Apollo* missions. Later, between 1985 and 1990, a wide program of polarimetric observations was carried out made possible by a new spectropolarimeter at Kharkiv Observatory in Ukraine. The results were presented in Shkuratov and Opanasenko (1992), Shkuratov et al. (1992). Close correlations were found between the polarisation parameters obtained via remote sensing techniques and physical properties of the lunar samples in the laboratory.

Imaging lunar polarimetry also became popular in the 1970s. Bowell and Zellner (1974) presented distributions of the polarisation parameters of the Moon, along with that of other Solar System bodies. Albeit the relatively low resolution, the different features of the lunar surface, such as the *maria* and *highlands* (see Section 2.1), could be distinguished from the polarisation parameters. In the 1980s a more advanced approach was suggested by Shkuratov (1981), resulting in a more accurate map of lunar surface properties. This approach required to measure the polarisation degree and large phase angles, which was significantly developed in the 1990s. Polarisation distributions and large phase angles were presented by Shkuratov and Opanasenko (1992), and Dollfus (1998) presented a series of papers on this topic in this decade. Since then, the polarisation at large phase angles has been studied extensively and published by Korokhin and Velikodsky (2005), also affiliated with Kharkiv Observatory. In parallel, the approach of measuring polarisation at small phase angles was developed and published by Shkuratov et al. (2008).

## 4.3. Multi-band Polarimetric Observations of the Nearside Lunar Surface

Polarimetric observations of the whole lunar nearside have been carried out by Jeong et al. (2015) at Lick Observatory in California, USA. These observations were done at five passbands: U, B, V, R, and I and phase angles $37^\circ \leq \alpha \leq 121^\circ$. The I band is unsuitable for any quantitative analysis because this band is just beyond the wavelength range of the polarisation filter. Therefore, four bands are used, whose central wavelengths are given in Table 4.1.

The polarisation degree is a function of phase angle. A typical polarimetric phase function for the Moon is presented in Figure 4.3, and it can be seen that it has a maximum near $\alpha_{\max} = 100^\circ$ (Shkuratov et al., 2015). Estimation of $P_{\max}$ from the ample measurements, the empirical functional form of $P(\alpha)$ has been adopted by Jeong et al. (2015), and the position of $P_{\max}$ is subsequently determined by means of $\chi^2$ fitting. However, one big limitation of lunar observation from Earth is that the range of $\alpha$ depends on selenographic longitude $\lambda$. The $\alpha$ range is narrower for smaller $|\lambda|$, because targets at smaller longitudes require smaller phase angles in order to be illuminated. The (theoretical) maximum phase angle at $\lambda = 0^\circ$ is $\alpha = 90^\circ$, and therefore the region $|\lambda| < 15^\circ$ does not include measurements for $\alpha_{\max}(\approx 100^\circ)$. Jeong et al. (2015) used measurements at smaller phase angles and the empirical

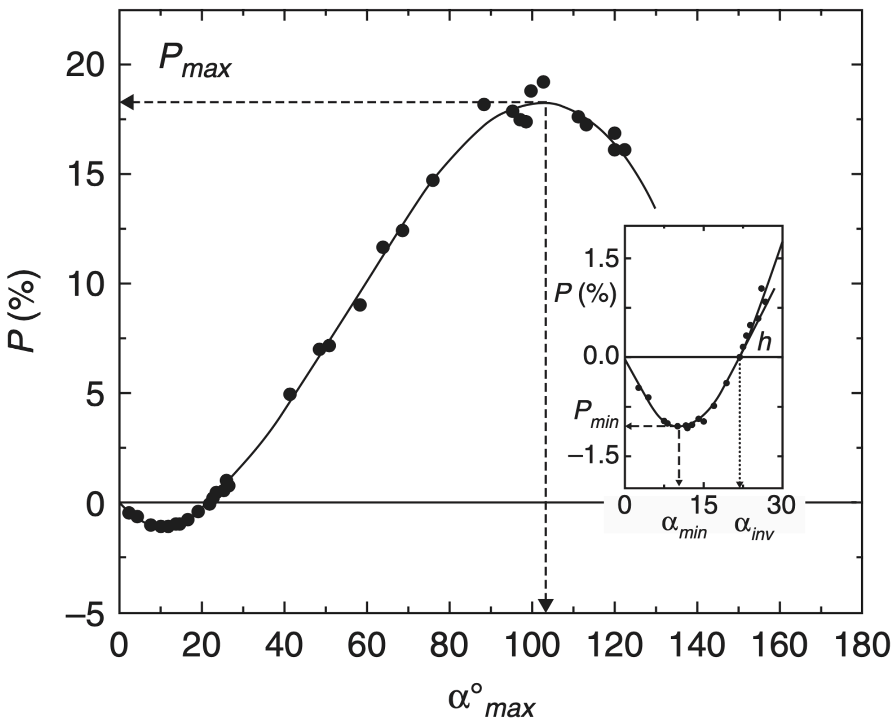

Figure 4.3: Typical polarimetric phase function of the Moon's surface (Kvaratskhelia, 1988).

functional form of $P(\alpha)$ to estimate values for $P_{\max}$ for $|\lambda| < 15°$.

All observations were subjected to standard reduction procedures such as dark subtraction, where correction has been made for the global brightness trend from the edge to the day/night boundary, and therefore the derived quantities are equigonal images (Shkuratov et al., 2011). Lunar libration effects were also corrected for, such that the sun-observer point on the Moon is located at selenographic longitude $\lambda$ and latitude $\beta$ = 0°, and north is up. These observations resulted in (equigonal) albedo and polarisation images of the lunar nearside ranging from $-75° \leq \lambda, \beta \leq 75°$, corresponding to the inner ~97% radius of the lunar disk, with a pixel resolution of 1.1 km at the center. Uncertainties in the measurements are 0.8%$A$ and 0.8%$P_{\max}$ (Jeong et al., 2015).

In Part II the albedo and polarisation maps are presented. The anti-correlation between albedo and maximum polarisation degree is used in the manuscript to derive physical properties of lunar regolith.

# 5

# Research Objective and Question

The research objective should include several key terms which outline the scope of the research. First, the *lunar shallow surface* will indicate that the study will focus on the upper layers of the lunar crust, corresponding to high spherical harmonic degrees and thus short-wavelength features. Second, the *combined gravity and light polarisation study* will indicate what resources will be used for the research. Especially the adjective *combined* is crucial in this statement. The lunar regolith has extensively been studied in the fields of gravimetry and polarimetry separately. It is believed that a combined study will reveal more information about the lunar shallow surface, as both domains are complementary in their nature. The estimated vertical and lateral density distributions of the upper crust from the Moon's gravity field are non-unique. Therefore, different density distributions will also satisfy the gravity constraints posed by the gravity field. It is expected that an additional independent source of information, in this case the polarisation degree of reflected sunlight, will aid to resolve the aforementioned ambiguity. Therefore, the research objective becomes:

> To characterise the lunar shallow surface by means of a combined gravity and light polarisation study of lunar regolith.

This leads to the following research question and sub-questions:

**How can GRAIL's gravitational potential field measurements in combination with lunar polarimetry measurements provide an improved vertical and lateral density and porosity distribution of the Moon's shallow surface compared to existing models?**

1. How can the vertical and lateral density distribution be estimated from the Moon's gravity field?
   (a) What are conventional crustal density models?
   (b) How can the global spherical harmonic gravity field be used to infer local density estimations?
   (c) How does the crustal density structure relate to the density and porosity of lunar regolith?
   (d) What are current density distributions of the Moon's shallow surface?
2. What physical information of lunar regolith can be inferred from lunar polarimetry?
   (a) Can regolith porosity be directly estimated from lunar polarimetry?
   (b) What lunar polarimetry observations are available that match the spatial resolution of the gravity field?
   (c) Are there significant differences between regolith properties in the lunar maria and highlands?
3. What is the correlation between lunar gravimetry and lunar polarimetry?
   (a) What is the relationship between polarimetry-derived properties and porosity?
   (b) How can laboratory photometry of lunar soil samples be used in this study?

(c) What is the relation between lunar nearside observations of regolith and laboratory photometry of regolith analogues?

Answers to these questions are believed to increase the knowledge of lunar regolith properties, relevant for human exploration of the Moon. Furthermore, it will advance small-scale gravity analyses by (partially) resolving its ambiguous nature. If correlations are found between lunar gravimetry and polarimetry, this could mean that future space missions to atmosphere-less astronomical bodies may benefit from both having a gravimeter and polarimeter instrument on board.

# Part II

# Manuscript

# Constraints on the Moon's Crustal Density Structure through Correlation between the Gravity Field and Reflected Surface Sunlight

**A.H.J. Bakx[1] and B.C. Root[1]**

[1]Delft University of Technology, Kluyverweg 1, 2629 HS Delft, The Netherlands

## Key Points:

- We develop a new strategy to constrain the density structure of the Moon's crust
- We find correlations between the Moon's gravity field and reflected sunlight of the lunar surface
- Our method connects laboratory photometry to lunar nearside observations

## Abstract

Previously determined vertical and lateral density distributions of the Moon's crust remain non-unique due to the ambiguous nature of gravity analysis. We use the high-resolution Gravity Recovery and Interior Laboratory (GRAIL) gravity field model to develop models of the spatially varying density structure in the lunar crust through a localised admittance approach. Furthermore, Earth-based telescopic observations of the lunar nearside map the median grain size of lunar regolith. Gravity-derived porosity, polarisation-derived median grain size and albedo of lunar regolith reveal similar dependencies as laboratory photometry of regolith analogues. We can constrain the density structure of the Moon's crust from a triangular correlation study between the aforementioned parameters. The constrained density structure is broadly consistent in bulk density, but differs in regional variations. Corresponding surface porosity values show a general consistency with lunar samples. Our method has only been demonstrated for the lunar nearside due to the lack of farside data. The correlation study performs well in the lunar highlands and has limited applicability for the geological complex lunar maria.

---

Corresponding author: A.H.J. Bakx, `aaronbakx@icloud.com`

# Plain Language Summary

The crustal structure of the Moon is key in deciphering the evolutionary history of the Moon. The main way of investigating the crustal structure is through gravity analysis via spacecraft tracking. Derived density profiles of the lunar crust have improved in resolution over the years, but remain non-unique since multiple density profiles fit the gravity observations. Therefore, we develop a new strategy to constrain the resulting density profiles by addition of an independent information source. We gather this information through analysis of reflected surface sunlight, which we use to add surface constraints to the spatially varying density profiles. Since the same hemisphere of the Moon always faces Earth, our study has only been demonstrated for this side because we use Earth-based telescopic observations to measure the reflected sunlight. Nevertheless, with our method we can substantially constrain the amount of density profiles resulting from the gravity field. Our best density profile is in accordance with previously determined bulk density estimates, while regional variations differ.

# 1 Introduction

New state-of-the-art gravity models of the Moon allow for small-scale gravity studies of the Moon's shallow surface, but their ambiguous nature hinders the determination of spatially varying density structures within the upper crust. As the Moon has been preserved for most of the solar system's age, it is a key for deciphering the evolution of the terrestrial planets, including Earth (Zuber et al., 2012). Understanding the Moon's evolution requires insight into its interior and crustal structure, which can be derived from the Moon's gravity field. The Gravity Recovery and Interior Laboratory (GRAIL) mission was designed to study the lunar interior structure by mapping the Moon's global gravity field at high resolution.

Improvements in the resolution of the GRAIL gravity models have led to high ($>0.9$) correlations between gravity and topography being obtained at smaller scales. High correlations at small scales between gravity and topography are expected as most surface topography is estimated to be uncompensated (Wieczorek, 2015). These high correlations have been exploited to model the density structure of the Moon's crust. Han et al. (2014) and Besserer et al. (2014) have evaluated several density-with-depth models, and found density variations in the crust due to compaction of porosity, and estimated surface porosities of 20% and higher. Additionally, the lunar maria and highlands have been found dissimilar in their vertical density structure. Goossens et al. (2020) have developed improved GRAIL gravity models and extended the results of Besserer et al. (2014) for smaller spatial scales.

They found that the vertical and lateral density profiles remain largely unchanged compared to lower-resolution gravity models, although some locations show lower surface density and therefore higher porosity, which they attributed to the increase in resolution of their gravity models.

However, these vertical and lateral density profiles remain ambiguous as the same gravity model produces non-unique vertical and lateral density structures of the Moon's crust. This ambiguous nature cannot be resolved by gravity data alone (Han et al., 2014). Ideally, an additional source is desired to provide constraints on these density profiles.

Analysis of reflected surface sunlight allows for physical parameters of the lunar regolith to be inferred. Discrete polarimetric observations at the Apollo landing sites in combination with lunar soil samples brought back from these historic missions allowed for maps of physical properties of lunar regolith, such as median grain size (Dollfus & Bowell, 1971). These median grain size estimations are closely related to the length of exposure to space weathering (Jeong et al., 2015).

Laboratory photometry of regolith analogues (e.g. Kaasalainen, S. (2003); Shkuratov et al. (2005); Kar et al. (2016); Labarre et al. (2017)) reveal that the scattered light of a regolith surface can be characterised by physical properties such as grain size, (bulk) porosity, composition, and surface roughness. Although a laboratory environment is a much more controlled environment compared to atmosphereless astronomical bodies such as the Moon, laboratory photometry of regolith analogues are paramount in interpreting remote observations of the Moon. Most importantly, lunar soil samples brought back to laboratories on Earth allow for comparative studies (Kiefer et al., 2012).

Strikingly, the albedo is primarily dependent on grain size and regolith porosity (Kar et al., 2020). Incident light can enter a more porous material deeper, meaning the surface albedo is expected to decrease with increasing porosity. However, the change in grain size will influence the packing density of the grains (Shepard & Helfenstein, 2007). Therefore, the surface albedo, regolith grain size, and regolith porosity are three parameters that are closely interconnected (Kar et al., 2020). Since grain size contains information of the individual grains and porosity contains information of the regolith layer in its entirety, these two parameters are expected to accurately describe the scattering behaviour of light. Besides, other physical properties of a regolith layer can be derived from grain size and porosity such as surface roughness and composition (Sakai & Nakamura, 2005).

In this work, we explore a potential additional information source being the scattering behaviour of sunlight from the lunar surface. We determine vertical and lateral density variations of the Moon's crust from the gravity field from which we estimate surface porosity. We then estimate the median grain size of nearside lunar regolith from telescopic polarimetric observations. A triangular correlation study between albedo, porosity, and grain size of the lunar nearside is then carried out from which we can constrain the density profiles of the Moon's crust.

# 2 Method

We follow the original approach of Besserer et al. (2014) to produce localised effective density spectra and subsequently use these spectra to fit theoretical density-with-depth models. From these models we describe how to obtain surface porosity of the Moon. Then we turn our attention to polarimetric observations and compute the polarimetric anomaly from albedo and polarisation degree, from which we can estimate the median grain size of nearside lunar regolith. Finally, we describe how to constrain the density profiles that emanate from the gravity field by a triangular correlation study between albedo, porosity, and grain size.

## 2.1 Vertical and Lateral Density Variations from the Gravity Field

### 2.1.1 Admittance and Effective Density

The greater part of the Moon's gravity disturbance signal is a result of the lunar surface topography (Zuber et al., 2012). Following Wieczorek et al. (2013), the observed free-air gravity $g$ can be modelled in terms of the gravity contribution induced by topography (Bouguer correction) with unit density, $\hat{g}$, as

$$g_{lm} = \rho_{\text{eff}}\,\hat{g}_{lm} + I_{lm}, \tag{1}$$

where $I_{lm}$ is the part of the observed free-air gravity that is not due to surface topography. We assume that $I_{lm}$ is a random variable uncorrelated with $\hat{g}$. Multiplying both sides of equation (1) by $\hat{g}_{lm}$, summing over all orders $m$, and taking the expectation with respect to $I_{lm}$, an unbiased estimate for the crustal density as a function of spherical harmonic degree $l$, called the effective density, is obtained:

$$\rho_{\text{eff}}(l) = \frac{S_{g\hat{g}}(l)}{S_{\hat{g}\hat{g}}(l)}. \tag{2}$$

Since lower spherical harmonic degrees correspond to gravity signals emanating from deeper within the Moon and from longer-wavelength structures than larger degrees, and vice-versa, the effective density can be interpreted as a depth-dependent density estimation (Besserer et al., 2014).

### 2.1.2 Theoretical Compaction Profiles

The effective density allows for fitting of theoretical density profiles to the observed density profile from gravity and surface topography. We start with a simple density model that varies linearly with depth. Following Besserer et al. (2014), the theoretical effective density spectrum of a linear density-with-depth model can be written as

$$\rho_{\text{eff, lin}}(l) = \rho_{\text{s,lin}} + \frac{a}{k(l)}, \tag{3}$$

where $\rho_{\text{s,lin}}$ is the linear surface density, $a$ is the linear density gradient, and the wavenumber $k(l)$ is related to the spherical harmonic degree $l$ as:

$$k(l) = \frac{1}{R}\sqrt{l(l+1)}, \tag{4}$$

where $R$ is the average radius of the Moon. In the lunar highlands this model has proven to produce realistic results (Goossens et al., 2020), however, this linear density-with-depth model is unrepresentative for the more geologically complex lunar maria. Therefore, we employ a different density-with-depth model in the maria than in the highlands. We model the lunar maria as a high-density basalt overlying a less-dense crust, analogously to impact basins flooded by ancient volcanic eruptions which are known to have formed the lunar maria (Lissauer & Pater, 2013). Following Gong et al. (2016), the theoretical effective density spectrum of this mare basalt model can be written as:

$$\rho_{\text{eff,mare}}(l) = \rho_{\text{b}} + (\rho_0 - \rho_{\text{b}})\left(1 - \frac{T_{\text{b}}}{R}\right)^{l+2} + \sum_{n=1}^{N}(\rho_n - \rho_{n-1})\left(\frac{r_n}{R}\right)^{l+2}, \tag{5}$$

where $\rho_{\text{b}}$ is the constant density of the overlying basalt, $\rho_0$ is the density of the upper lunar crust, $T_{\text{b}}$ is the thickness of the mare basalt, and $\rho_n$ is the density between interfaces $n$ and $n-1$ predicted from the crustal density gradient $a$. A schematic figure explaining both density models is shown in Figure S1.

We assume that the density variations at depth have the same relief at the surface, which is a reasonable assumption in the lunar highlands where density increase is expected as a result of compaction of porosity with depth (Han et al., 2014). This would also be a reasonable assumption in the maria if the basalt thickness is constant within the region of analysis, which is not necessarily the case everywhere in the maria (Wieczorek, 2015). Despite that, if the mare basin is completely flooded the gravity signals emanating from the basalt layer is uncorrelated with surface topography, and the effective density (equation 2) would be statistically unbiased by the presence of underlying impact basin topography (Gong et al., 2016).

In order to make progress in estimating the basalt density from the mare model it is necessary to constrain the other parameters in this model based on a priori information. We adopt basalt thickness estimates by Du et al. (2019), who estimate basalt thicknesses from high-resolution lunar topography by modelling the degradation of partially-buried craters presented in discrete latitude and longitude coordinates. These are translated to a spatial map by linear interpolation within the lunar maria. Maria bounds are taken from the polygon vector map from the Lunar Reconnaissance Orbiter Camera (Nelson et al., 2014).

We assume that the crust underneath the mare basalts are similar to the highland crust. The upper crustal density $\rho_0$ and linear density gradient of the crust $a$ will be constrained using the linear model in the lunar highlands. Characteristic density profile values of $\rho_0 = 2390$ kg/m$^3$ and $a = 21$ kg/m$^3$/km have been found for the lunar highlands (Besserer et al., 2014). However, the spherical cap radius of the localisation window (section 2.1.3) may influence the resulting crustal density profile, and therefore $\rho_0$ and $a$ will be constrained with highland values obtained for the corresponding localisation method.

#### 2.1.3 Localised Spectral Multitaper Approach

The theoretical effective density spectra are least-squares fitted to the observed effective density spectrum, from which the vertical density variations are estimated. Parameters of interest are (in this case) the surface density, which is $\rho_{\mathrm{s,lin}}$ for the linear model and $\rho_{\mathrm{b}}$ for the mare model, and the linear density gradient $a$. We use the GRAIL degree and order 1200 GRGM1200B RM1 $\lambda = 10$ gravity model, and following (Goossens et al., 2020), an upper limit of $l_{\max} = 650$ is posed to ensure sufficient ($> 0.90$) correlation between gravity and topography for accurate effective density spectra. Lithospheric flexure is negligible for spherical harmonic degrees below 170 (Wieczorek et al., 2013). Following Besserer et al. (2014), we take $l_{\min} = 250$ as lower limit for our analysis. The best fitting models for two mare regions and two highland regions are presented in Figure 1, from which it can be seen that the lunar maria are more difficult to model than the highlands.

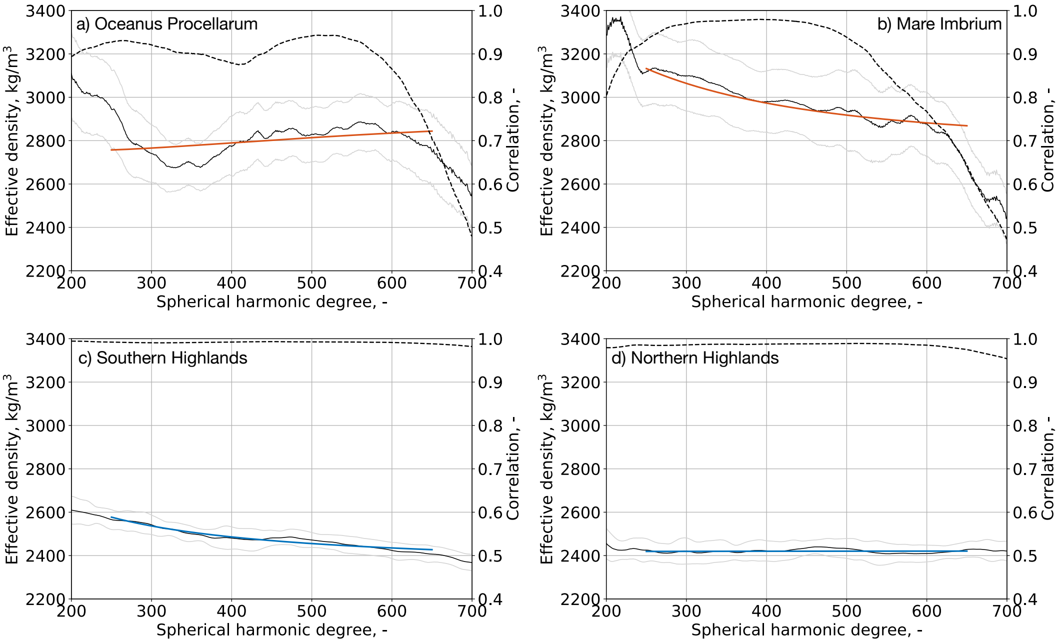

**Figure 1.** Effective density spectra for representative regions in a) Oceanus Procellarum, b) Mare Imbrium, c) Southern Highlands, and d) Northern Highlands. The colored line is the best fitting theoretical model, where red indicates the basalt model, and blue indicates the linear model. The black line represents the local observed effective density spectrum, with the grey lines being the standard deviation of the local spectrum. The dashed line is the spectral correlation between gravity and gravity predicted from topography (Bouguer correction).

We obtain lateral density variations by means of localisation. Local spectra of the effective density are estimated by multiplication of localisation windows concentrated within a spherical cap with a given radius $\theta_{\text{cap}}$ and spherical harmonic bandwidth $l_{\text{win}}$ (Wieczorek & Simons, 2007). The windows are then rotated to an area of interest on the lunar nearside. We use a concentration factor of 0.99 to select the best $k$ tapers (Goossens et al., 2020). The uncertainty in the local effective density spectrum is minimised by treating a large number of spherical caps $k$ (and thus large $l_{\text{win}}$), however, at the same time the effect of spectral leakage is limited by choosing caps with a larger radius $\theta_{\text{cap}}$ (and thus low $l_{\text{win}}$ for same $k$) (Wieczorek & Simons, 2005).

The local power spectrum for each best taper $k$ is calculated by multiplying the global data by the window and expanding the results in spherical harmonics, from which the local effective density spectrum estimate $\rho_{\text{eff}}^{(k)}(l)$ is calculated as

$$\rho_{\text{eff}}^{(k)}(l) = \frac{S_{g\hat{g}}^{(k)}(l)}{S_{\hat{g}\hat{g}}^{(k)}(l)}. \tag{6}$$

The multitaper effective density spectrum estimate $\rho_{\text{eff}}^{(mt)}(l)$ is then obtained by taking the average of the $K$ individual local spectrum estimates,

$$\rho_{\text{eff}}^{(mt)}(l) = \frac{1}{K}\sum_{k=1}^{K} \rho_{\text{eff}}^{(k)}(l). \tag{7}$$

Subsequently, the theoretical effective density spectra (section 2.1.2) are least-squares fitted to the localised effective density spectrum. This procedure is repeated for each 5° latitude and longitude, and cubic interpolation is used to obtain a map of resolution 1° by 1° centered on the lunar nearside. The SHTools software package is used for the localisation analysis (Wieczorek & Meschede, 2018).

We repeat here that the lateral variations are the result of the moving of localisation window. Within the spherical caps the lateral variation is thus constant. The radius of the spherical cap is therefore especially important for geologic complex areas (Deutsch et al., 2019).

A wide range of spherical cap radii is considered, from $\theta_{\text{cap}} = 5^\circ$ to $70^\circ$ (150 to 2150 km), and the window bandwidth $l_{\text{win}}$ is chosen such that $k = 30$ concentrated tapers are obtained with concentration factor 0.99, corresponding to $l_{\text{win}} = 174$ to 13, respectively. The localised spectrum at degree $l$ contains contributions from the global field degrees $l - l_{\text{win}}$ to $l + l_{\text{win}}$.

We validate the localised admittance approach by using the same model parameters as Goossens et al. (2020) ($\theta_{\text{cap}} = 7.5°$ and $15.0°$) and obtain identical distributions for the linear model.

### 2.1.4 Lunar Regolith Grain Density and Porosity

The fraction of void space in the lunar regolith is called the porosity, and can be calculated as:

$$\phi = 1 - \frac{\rho}{\rho_{\text{g}}}, \tag{8}$$

where $\rho$ is the bulk density of regolith and $\rho_{\text{g}}$ is the grain density of the individual grains (Hilst et al., 2002). Surface density estimates from the localised admittance approach are inherently bulk density estimates, and grain density estimates are determined from an empirical relationship with FeO and $TiO_2$ abundances in the regolith:

$$\rho_{\text{g}} = 27.3 \cdot \text{FeO} + 11.0 \cdot \text{TiO}_2 + 2773.0, \tag{9}$$

where FeO and $TiO_2$ are expressed as concentrations in mass fraction wt. % (Huang & Wieczorek, 2012). FeO and $TiO_2$ are taken from Lunar Prospector gamma ray spectrometer measurements and very between 0.0-0.30 and 0.0-0.12 wt. %, respectively (Prettyman et al., 2006). Figure 2 presents a surface density estimate from localisation (section 2.1.3), the grain density map from equation 9, and the resulting porosity by applying equation 8. It can be seen that grain density estimates are generally higher in the maria than in the highlands, but do not necessarily result in higher porosity due to varying surface density.

## 2.2 Polarimetric Anomaly and its Relation to Median Grain Size

In this section we exploit the anti-correlation between albedo and polarisation degree of the lunar nearside to infer median grain size of nearside regolith porosity.

### 2.2.1 Albedo and Polarisation Distributions of the Lunar Nearside

Following Shkuratov et al. (2015), the degree of polarisation, $P$, is expressed in terms of the Stokes parameters as:

$$P = \sqrt{\frac{Q^2 + U^2}{I^2}}, \tag{10}$$

where Stokes $I$, $Q$, and $U$ are defined by:

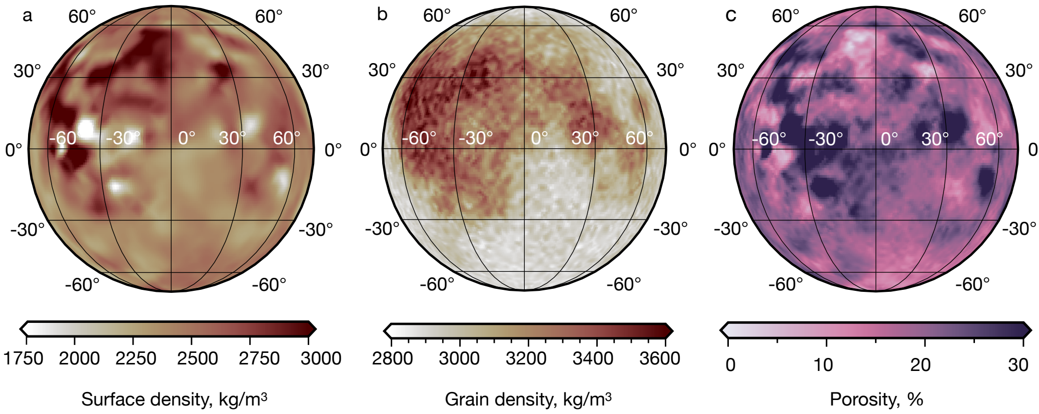

**Figure 2.** Nearside (a) surface density estimates for a linear density-with-depth profile with $\theta_{\text{cap}} = 7.5°$, (b) grain density estimates from Lunar Prospector gamma ray spectrometer, and (c) porosity estimates using equation 8. The maps are presented in an orthographic projection centered on 0° longitude.

$$
\begin{aligned}
I &= (I_0 + I_{45} + I_{90} + I_{135})/2, \\
Q &= I_0 - I_{90}, \\
U &= I_{45} - I_{135},
\end{aligned} \tag{11}
$$

and $I_p$ is the intensity of the light wave at a polarisation angle $p$ in degrees.

We use the multi-band polarimetric observations of the whole lunar nearside by Jeong et al. (2015). Albedo $A$ and maximum polarisation degree $P_{\text{max}}$ images are presented in Figure 3. The lunar nearside albedo image in Figure 3a reveals the prominent dark lunar maria and bright lunar highlands. The maria are smooth low-lying basaltic plains formed by ancient volcano eruptions (Lissauer & Pater, 2013). The lunar highlands are anorthositic in composition and are older than the maria, indicated by the presence of more impact craters (Engelhardt et al., 1976).

#### 2.2.2 Polarimetric Anomaly and its Consequences for Surface Characteristics

The albedo and maximum polarisation images in Figure 3 look like inverted counterparts when using the same gray scale colormap. This observation is a visual confirmation of Umov's effect, which describes the empirical anti-correlation between albedo and polari-

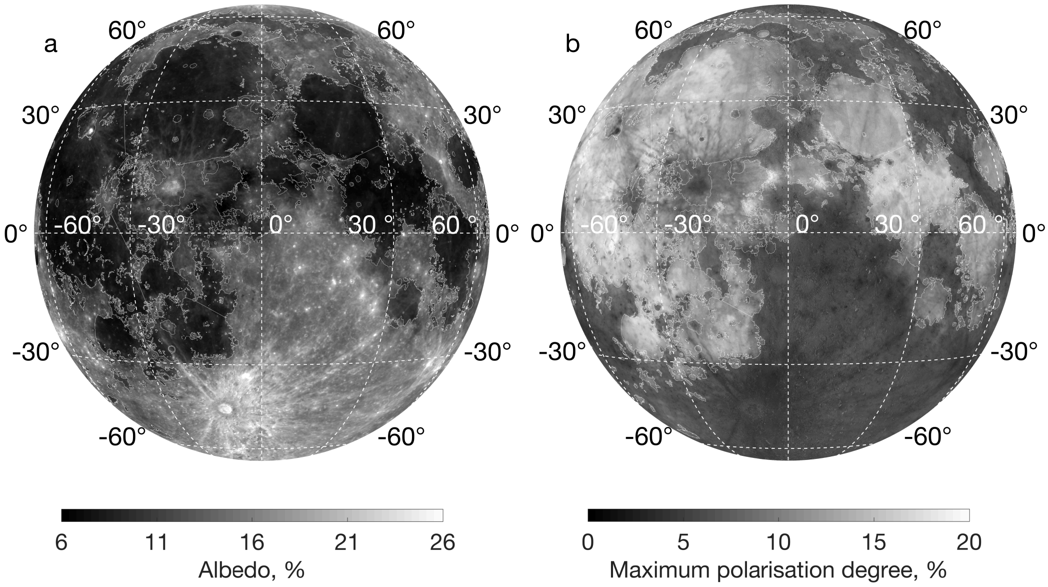

**Figure 3.** Nearside V-band (a) albedo- and (b) maximum polarisation ($P_{\max}$) maps of the Moon measured by Jeong et al. (2015). The maps are presented in an orthographic projection centered on 0° longitude.

sation degree, and is based on the principle that multiply scattered light is barely polarised (Umov, 1905). Multiply scattered light is light that has interacted with multiple grains before it is reflected to Earth. When the grains absorb more light, thus having a lower albedo, the less opportunity the light has to interact with more grains, and therefore it is less multiply scattered. This results in more single scattered light being measured, and since single scattered light is higher polarised than multiply scattered light, the observed polarisation degree tends to be higher (Shkuratov et al., 2011).

However, the anti-correlation between albedo and polarisation degree may not necessarily hold for the whole lunar nearside. For example, if more absorption leads to more light being observed that has scattered with the upper grains, and if these grains naturally have a lower polarisation degree than the underlying grains, the observed polarisation degree will decrease with decreasing albedo (Hapke & Sato, 2015).

Umov's law has been widely studied for the Moon and it is generally recognised that the lunar surface behaves very Umov-like (Shkuratov et al., 2011). The polarimetric observations presented in log $A - \log P_{\max}$ space are given in Figure 4 and indeed reveal a strong anti-correlation between albedo and maximum polarisation degree. Following Dollfus and

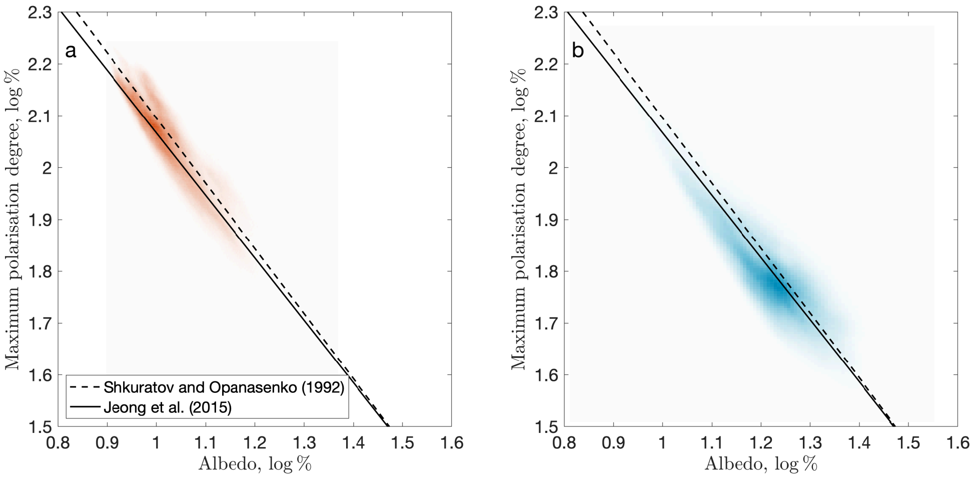

**Figure 4.** Anti-correlation between 630 nm albedo and maximum polarisation degree distributions for the nearside (a) lunar maria and (b) lunar highlands. The regression line is presented with empirical constants determined by Shkuratov and Opanasenko (1992) and from a best fit of the observations by Jeong et al. (2015). A darker colour is associated with a higher density of points.

Bowell (1971), the negative-linear regression line through the log $A - \log P_{\max}$ distribution can be described as:

$$\log A + a \log P_{\max} = b, \tag{12}$$

where $a$ and $b$ are empirical constants which depend on wavelength, and $A$ is represented in units of percent (%) and $P_{\max}$ in units of permilli (‰). Shkuratov and Opanasenko (1992) determined $a = 0.845$ and $b = -1.801$ for 630 nm wavelength. Since the polarimetric observations of Jeong et al. (2015) are more abundant than those by Shkuratov and Opanasenko (1992) the empirical constants are re-evaluated here. Least-squares fitting of the regression line to the observations results in $a = 0.8294 \pm 0.0007$ and $b = -1.885 \pm 0.002$ for 630 nm wavelength. The constant $a \neq 1$ means that there is a small dependence of Stokes $Q$ on $A$ (Shkuratov et al., 2015). The regression line for the two sets of empirical constants is also shown in Figure 4.

Nevertheless, we observe an overall scatter around the regression line. The point scatter may be due to physical characteristics of surface regolith, such as refraction index, grain shape, grain orientation, packing density, and grain size (Shkuratov et al., 2011). The study of surface characteristics with polarimetry is advanced by treating $b$ as a parameter instead of constant, and is formally called the polarimetric anomaly (Shkuratov et al., 2015).

Laboratory polarimetric measurements of lunar soil samples have revealed an empirical relationship between the median grain size $d$ of lunar regolith and polarimetric anomaly (Shkuratov & Opanasenko, 1992):

$$d = 0.03 \cdot \exp\left(2.9 \cdot b\right) \tag{13}$$

We note that equation 13 should be applied carefully. Laboratory determination of median grain size and the scarcity of lunar soil samples result in uncertainties in the empirical relationship between median grain size and polarimetric anomaly. Furthermore, the term 'median grain size of regolith' is conditional since the part of the lunar soil particles are aggregates of fragments and dust (Hapke & Sato, 2015). Therefore, the median grain size values resulting from the empirical relationship with polarimetric anomaly may be slightly biased.

## 2.3 Polarimetric Constraints on the Moon's Crustal Density Structure

Laboratory photometry of regolith analogues reveal a clear dependency between albedo and grain size or albedo and porosity for fixed porosity or fixed grain size, respectively (Kar et al., 2020). We will evaluate each vertical and lateral density structure from the localised admittance approach by a triangular correlation study between gravity-derived porosity, polarisation-derived grain size, and albedo. Therefore, we fix one of these three parameters and subsequently calculate the correlation between the other two.

We then increase the fixed parameter and repeat over the whole range of the fixed parameter. The step size is determined by the extreme values of the fixed parameter, and we aim for approximately 50 steps in total. Extreme values of the fixed parameter go hand in hand with a low amount of data points which naturally leads to a high correlation value with large error. Therefore, a lower-limit of 500 data points is set to ensure statistical significance and minimise error in our results.

This lower-limit translates to median grain sizes between 60 and 100 µm, porosity estimates between 15 and 25%, and albedo values between 8 and 24%. In section 3.3 we will present the obtained correlations between albedo, porosity, and grain size for the lunar nearside.

Correlation between two samples $X$ and $Y$ with equivalent size $n$ is expressed as Pearson product-moment correlation coefficient and Szekely-Rizzo-Bakirov (SRB) distance correlation coefficient,

$$\mathrm{Cor}(X,Y) = \frac{\mathrm{Cov}(X,Y)}{\sqrt{\mathrm{Var}(X)\mathrm{Var}(Y)}} = \frac{\mathrm{Cov}(X,Y)}{\sqrt{\mathrm{Cov}(X,X)\mathrm{Cov}(Y,Y)}} \tag{14}$$

$$\mathrm{Cov}(X,Y) = \begin{cases} \dfrac{1}{n^2}\displaystyle\sum_{i=1}^{n}\sum_{j=1}^{n}\frac{1}{2}(x_i - x_j)(y_i - y_j), & \text{Pearson,} \\ \dfrac{1}{n^2}\displaystyle\sum_{i=1}^{n}\sum_{j=1}^{n} D(x_i, x_j)D(y_i, y_j), & \text{SRB,} \end{cases} \tag{15}$$

where $x_k$ represents instance $k$ of sample $X$ and $D(x_i, x_j)$ is the Euclidean distance in arbitrary dimension between $x_i$ and $x_j$ (analogously for $y$). The SRB correlation coefficient is able to quantify linear and non-linear correlation (Szekely et al., 2007), and the Pearson correlation coefficient which can only quantify linear correlation (Benesty et al., 2009). The difference between the SRB and Pearson correlation coefficients provides insight into the type of correlation used for comparison with laboratory photometry in section 4.1.

# 3 Results

In this section we will present the results in this study. First, we will present the vertical and lateral density and porosity distributions from the gravity field. We then present the median grain size map of nearside lunar regolith. From these results we calculate correlations between albedo, porosity, and grain size for the various density profiles from the gravity field. Finally, we plot a constrained map of the Moon's crustal density and porosity structure.

## 3.1 Density and Porosity Distributions from the Gravity Field

Figure 5 shows spatial distributions of surface density, density gradient, and surface porosity for the lunar nearside resulting from the localised admittance approach (section 2.1.3) for various values of spherical cap radius.

The mare regions are more prone to a change in cap radius than highland regions, probably because the maria are more geologically heterogeneous compared to the highlands. An increasing surface density with decreasing cap radius is observed in Mare Imbrium. Porosity values in this region decrease from 30% to 0% until $\theta_{\mathrm{cap}} \approx 40^\circ$ and become negative (unrealistic) for smaller cap radii. Highland bulk porosity remains constant at about 20%, consistent with lunar highland samples, and only regional variations differ with cap radius. In contrast, mare porosity are either negative or very large $> 30\%$, inconsistent with known porosity of lunar samples from mare regions (Kiefer et al., 2012).

There is an absence of negative density gradients for $\theta_{\text{cap}} > 50°$ and the increasing appearance for smaller cap radii, which could indicate undiscovered mare regions (Besserer et al., 2014).

## 3.2 Median Grain Size of Lunar Regolith from Polarimetry

The multi-band polarimetric observations of Jeong et al. (2015) are interpolated to 630 nm wavelength. Median grain size estimates resulting from the empirical relationship with polarimetric anomaly (equation 13) are presented in Figure 6.

First, we observe a larger median grain size in the lunar maria than in the lunar highlands. It is thought that the compositional difference between anorthosites (highlands) and basalts (maria) result in larger grain sizes in the maria than in the highlands.

Second, many young small (km-sized) craters, as well as larger craters such as Copernicus, Tycho, Aristarchus, Kepler, Langrenus, and Byrgius (indicated in Figure 6), stand out with larger median grain size values than their surroundings, which confirms the proposal by Shkuratov et al. (2015) that the median grain size can be used as a maturity indicator. These large median grain size values are probably due to relative immature local regolith, as regolith surfaces are on average smoother than surfaces that have been subjected to (micro-)meteoroid impact cratering (Dollfus, 1998).

Third, a clear latitude-dependence of the median grain size is observed. A larger flux of space weathering agents in the ecliptic plane result in increasing comminution on the equator compared to the poles (Jeong et al., 2015).

Finally, we observe that the median grain size values are not leveled at selenographic longitude $\lambda = 0°$, which is because the polarimetric observations in the western and eastern halves of the lunar disk are calculated with data from the waning and waxing periods, respectively (Jeong et al., 2015). There are two additional level mismatches at $\lambda = \pm 15°$ arising from the extrapolation of $P_{\max}$ for $|\lambda| < 15°$ due to the corresponding phase angle being $\alpha > 100°$.

## 3.3 Triangular Correlations for Various Regolith Porosity Distributions

Laboratory photometry of regolith analogues reveal that albedo, porosity, and grain size are closely interconnected (section 1). In this section we will re-evaluate this triangular dependency for the lunar nearside, and try to constrain the Moon's crustal density structure through this correlation study.

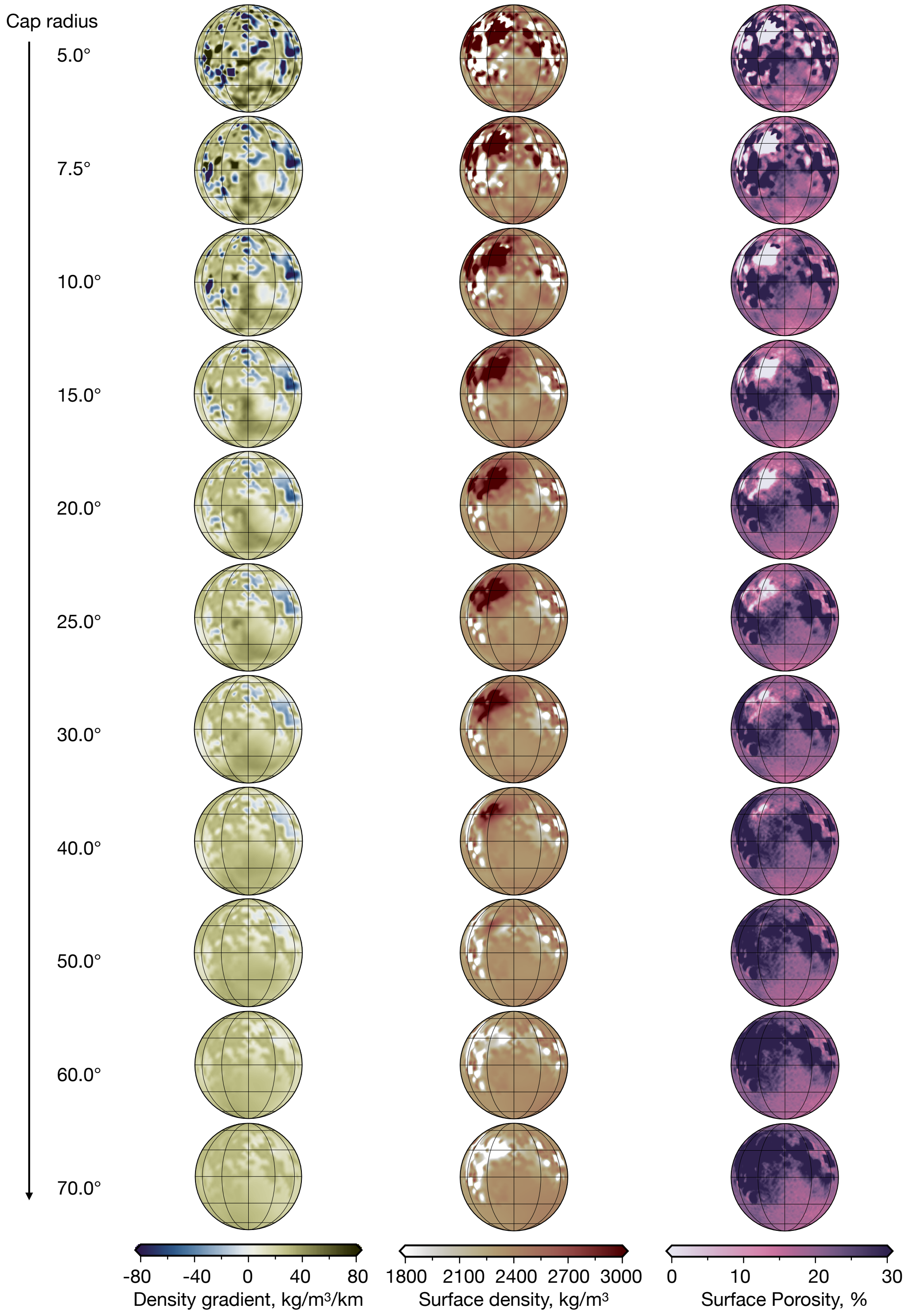
Cap radius
5.0°
7.5°
10.0°
15.0°
20.0°
25.0°
30.0°
40.0°
50.0°
60.0°
70.0°
-80
-40
0
40
80
Density gradient, kg/m³/km
1800
2100
2400
2700
3000
Surface density, kg/m³
0
10
20
30
Surface Porosity, %

**Figure 5.** Overview of the density and porosity structures resulting from the localised spectral multitaper approach for cap radii ranging between 5° (150 km) to 70° (2150 km). The maps are presented in an orthographic projection centered on 0° longitude.

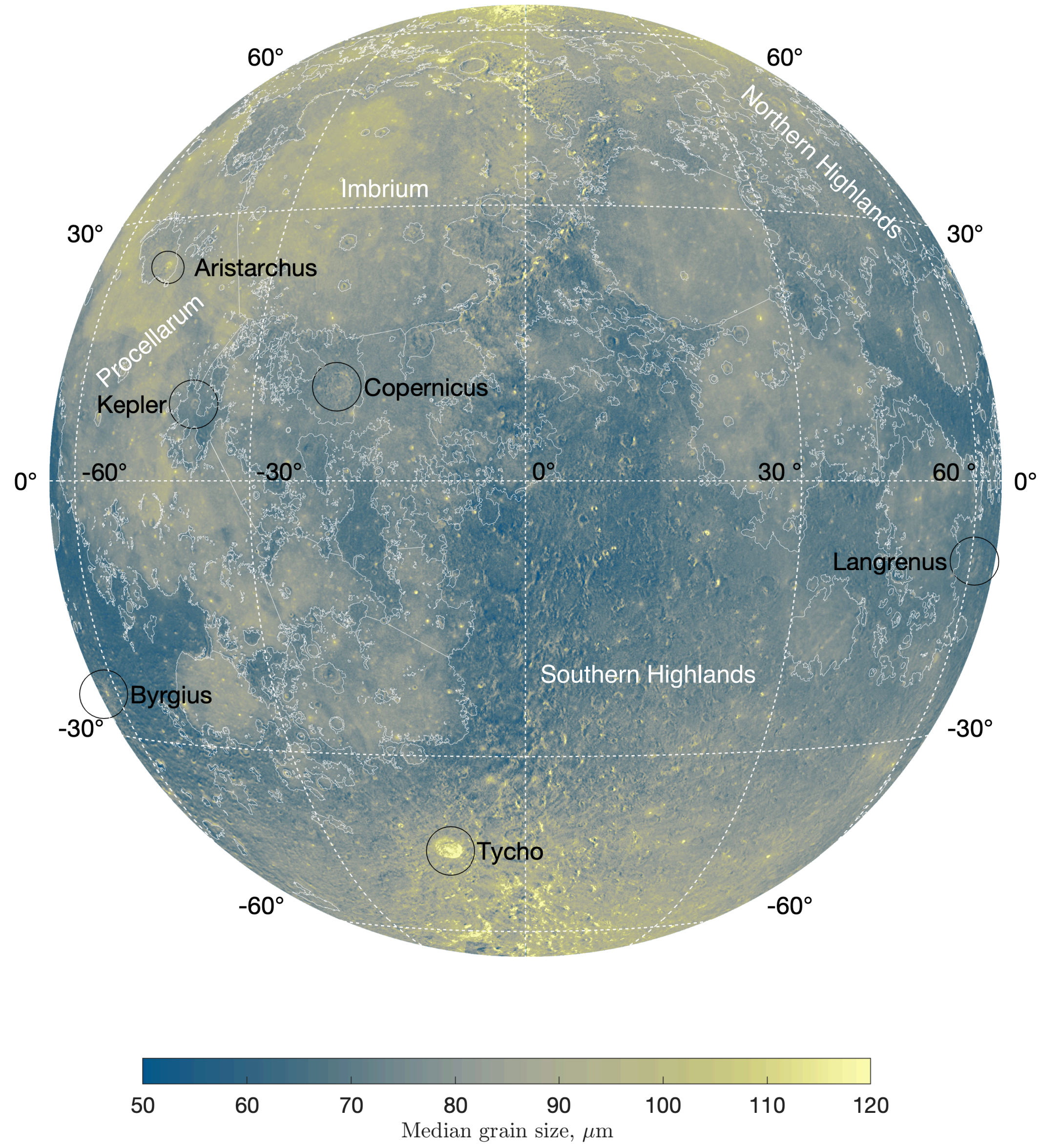
60°
60°
Northern Highlands
Imbrium
30°
30°
Aristarchus
Procellarum
Copernicus
Kepler
0°
-60°
-30°
0°
30 °
60 °
0°
Langrenus
Southern Highlands
Byrgius
-30°
-30°
Tycho
-60°
-60°
50
60
70
80
90
100
110
120
Median grain size, μm

**Figure 6.** Nearside median grain size of lunar regolith estimates of the Moon. The map is presented in an orthographic projection centered on 0° longitude. Lunar maria are outlined by a thin solid white line, and large craters discussed in the text are indicated by a black circle.

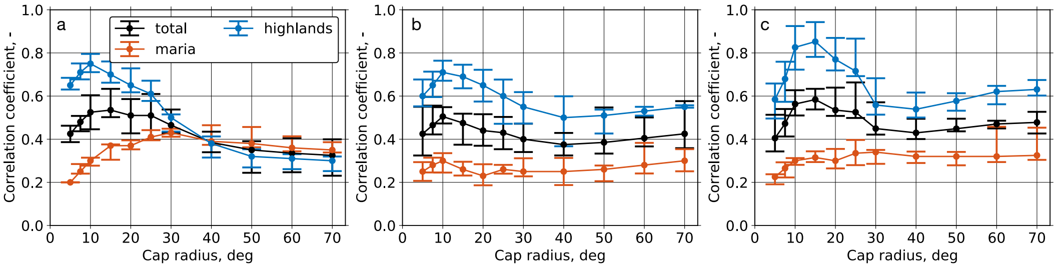

**Figure 7.** Nearside correlation between regolith albedo, polarisation-derived median grain size, and gravity-derived porosity of the Moon. Correlations are calculated between two parameters for a range of fixed values of the third; (a) albedo-porosity, (b) albedo-grain size, and (c) porosity-grain size. Correlation expressed as Szekely-Rizzo-Bakirov (SRB) distance correlation coefficient (Szekely et al., 2007), and presented by median values (dots) and 25th and 75th percentiles (whiskers) as a function of localisation spherical cap radius.

In previous sections we have estimated regolith porosity from the Moon's high-resolution gravity field (section 3.1) and regolith median grain size from telescopic polarimetric observations (section 3.2). We calculate the SRB correlation coefficient for a wide variety of regolith porosity distributions, which are mainly dependent on localisation spherical cap radius (section 2.1), and present them in Figure 7.

We observe that the triangular correlation between albedo, porosity, and median grain size for the lunar nearside is more substantial in the lunar highlands than in the lunar maria. In section 4.3 we elaborate upon the influence of the theoretical density-with-depth models on the correlation results.

The triangular correlation becomes more substantial with decreasing cap radius, and drops again for cap radii smaller than 10°. On the one hand a small localisation window is desired as the density-with-depth model is constant within this window, while on the other hand a smaller window is more prone to spectral noise such as leakage (section 2.1.3). Furthermore, the uncertainty of the local spectrum is minimised by treating a large number of tapers $k$ within the localisation window (equation 7). For constant $k$, the window bandwidth increases as spherical rap radius decreases, resulting in a larger portion of the spherical harmonic degrees being unreliable (Wieczorek & Simons, 2007). Additionally, since the density-with-depth model is constant within the localisation window the cap radius becomes especially important in geological complex areas, such as mare-highland boundaries.

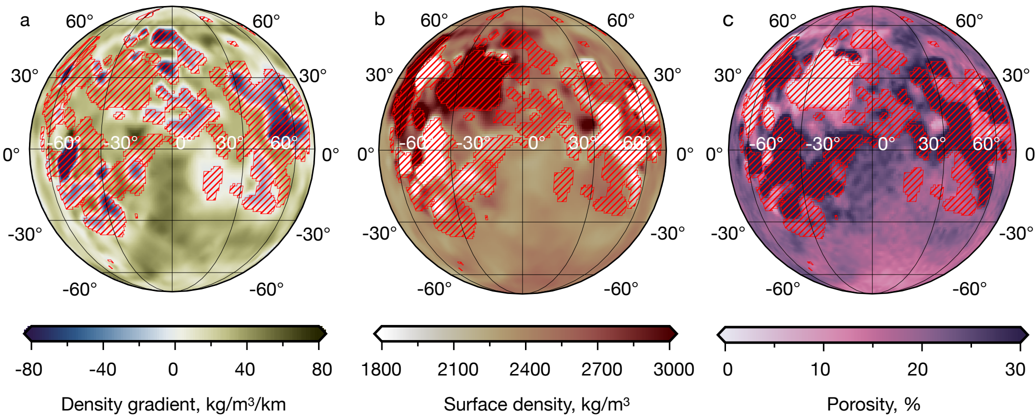

**Figure 8.** Nearside (a) density gradient, (b) surface density, and (c) surface porosity distributions that have highest correlations with polarimetric observations, resulting from the localised spectral multitaper approach for cap radius of 10° (300 km). Regions that are not treated in our analysis are indicated by the red hatch. The maps are presented in an orthographic projection centered on 0° longitude.

Therefore, there is a fine balance between window size and accuracy of local spectra, which we observe in Figure 7.

Even though the high-resolution GRAIL GRGM1200B RM1 $\lambda = 10$ gravity model allows for cap radii up to 5°, we observe that correlation with polarimetry decreases for cap radii smaller than 10°. Overall, we observe that the density structure estimated from a localised admittance approach of the gravity field with cap radius of 10° has the highest correlation with polarimetry. For cap radii larger than 40° ($> 1200$ km) the triangular correlation remain substantial, which is likely because grain density is used to determine porosity (equation 8). Nevertheless, no perfect unity correlation is observed for our models.

### 3.4 Constrained Crustal Density and Porosity Structure

The vertical and lateral density and porosity distribution which have highest correlation with polarimetry are presented in Figure 8.

Surface densities in the lunar highlands are $2396 \pm 33$ kg/m$^3$, and in the lunar maria $2565 \pm 72$ kg/m$^3$. We observe large surface densities of $> 3000$ kg/m$^3$ in Mare Imbrium and parts of Oceanus Procellarum, and in general lower surface densities $< 1800$ kg/m$^3$ in the other mare regions, and these areas correspond with unrealistic porosity values and (partly) negative density gradients. Therefore, our analysis is limited to realistic porosity values ($0 < \phi < 30$ %) and positive density gradients, and density estimates in the mare will be treated with some caution.

Density gradients of $22.9 \pm 4$ kg/m$^3$/km are obtained for highland regions. In and around mare regions these values are also observed because we assume similar crustal structure below the mare basalts (section 2.1.2). Additionally, some areas have *negative* density gradients, even after application of the basalt model.

Comparing our estimates with those by Goossens et al. (2020), our surface density estimates in the highlands are slightly larger (+72 kg/m$^3$), while density gradients in these regions are similar (-4.4 kg/m$^3$/km). Our surface density estimates in the maria are much lower (-271 kg/m$^3$).

Highland porosities of $18.4 \pm 1$ % are consistent with those of lunar highland samples (averaging about 20%), while porosity values of in the mare average at $19.7 \pm 2$ %, compared to porosities of 6-11% of mare soil samples (Kiefer et al., 2012).

# 4 Discussion

## 4.1 Type of Correlation and Comparison with Laboratory Photometry

We also calculate the Pearson product-moment correlation coefficient for the various porosity distributions as shown in Figure S2. The discrepancy between the SRB and Pearson coefficients allows us to gain insight into the type of correlation.

From Figure S2 we observe an anti-correlation between albedo and porosity for fixed grain size. Correlations tend to be almost negative-linear, while becoming slightly concave down for regolith models with spherical cap radius smaller than 10°. An anti-correlation between albedo and porosity is in accordance with laboratory photometry of regolith analogues (Kar et al., 2020). An increasing porosity results in a decreasing albedo because incident light can enter a more porous material deeper, increasing the probability of absorption (Hapke, 2008).

Furthermore, we observe albedo and grain size to be anti-correlated for fixed porosity values, which is in accordance with laboratory photometry of regolith analogues (Kar et al., 2020). Albedo probably decreases with increasing grain size as larger grains produce a more prominent shadow than smaller grains, as well as larger grains offer less multiple scattering than smaller grains (Hapke & Sato, 2015).

Finally, we observe porosity and grain size to be anti-correlated for fixed albedo values. In theory, porosity is independent of grain size for well-sorted grains. However, grain size probably affects porosity because deformation from a spherical shape increases with decreasing grain size (Ogolo et al., 2015). Porosity decreases as sphericity increases due to tighter packing with spherical grains, and therefore we expect porosity and grain size to be anti-correlated.

## 4.2 Selenographic Latitudinal Dependency

From our median grain size map (Figure 6) we noted a dependency on selenographic latitude. In this section we will elaborate on the influence of the selenographic latitude on our results.

We present the median grain size as a function of selenographic latitude $\beta$ in Figure 9. We observe an increasing median grain size with increasing latitude, which is probably because there is a larger flux of space weathering agents on the equator than on the poles. Weathering agents include solar wind particles and micrometeoroids, which are primarily along the ecliptic plane (Hemingway et al., 2015). Repeated bombardment of microscopic meteoroids causes the regolith grains to break up, and that of solar wind particles causes production of nanophase reduced iron (npFe$^0$) particles on regolith grain surfaces (Pieters et al., 2000). An increased flux of weathering agents directly results in an increase in comminution of regolith (Horz et al., 1984).

Furthermore, we observe smaller median grain size values in the lunar highlands than in the lunar maria for the same latitude band. The same observation has been reported previously by Shkuratov et al. (2007) and Jeong et al. (2015), who accounted this phenomenon due to the compositional difference between the highlands and the maria, meaning anorthosites (highlands) comminute more than basalts (maria) for similar flux of space weathering agents (Engelhardt et al., 1976). Since distributions for $|\beta| > 50°$ show similar median grain size values, lunar soils in the maria and highlands probably start with similar grain size, and the decreasing evolution of grain size with takes place more rapidly in the highlands than in the maria. Taking into account that the highlands are older than the maria, 4.4 Gyr compared to 3.1-3.9 Gyr (Papike et al., 1998), we estimate from the slopes in Figure 9 that the highlands are 8 to 35% more sensitive to comminution than the maria due to the difference in composition.

Next, we investigate the influence of selenographic latitude on the triangular correlation between albedo, porosity, and grain size. We present SRB correlations as a function of latitude for 10° cap radius porosity model in Figure 10, and obtain similar trends for all other porosity models. We observe an increasing correlation with latitude in the highlands,

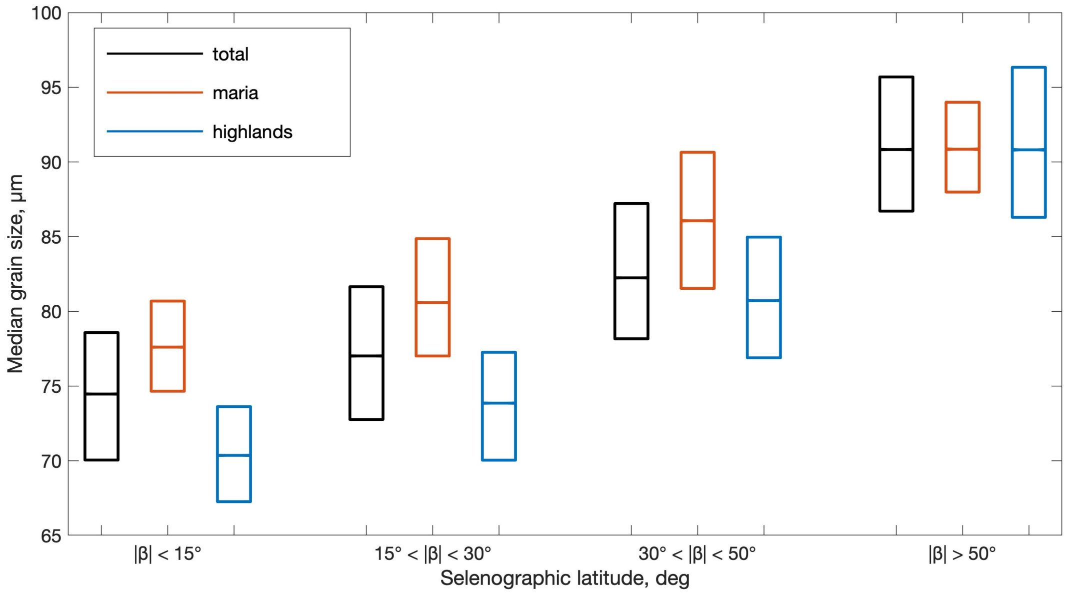

**Figure 9.** Boxplots of nearside median grain size for the maria (red), highlands (blue), and total nearside (black) of the Moon, as a function of selenographic latitude $\beta$. The central lines within the boxes are the median values, and the boxes range from 25th to 75th percentiles.

and a constant correlation as a function of latitude in the maria. An increasing correlation with latitude could be a combination of the following causes.

First, the decrease in grain size for decreasing latitude results in the grains being more deformed from a spherical shape (Ogolo et al., 2015). Therefore, the behaviour of the scattered light at lower latitudes could be more dependent on particle shape, resulting in a decrease in correlation between albedo, porosity, and grain size.

Second, the regolith porosity is estimated by fitting an assumed density profile to the gravity signals emanating from the Moon's crust (section 2.1.2). The regolith is estimated to be about 5 m thick in the maria and between 10 and 15 m thick in the nearside highlands (Fa & Wieczorek, 2012), however, the upper few centimeters of the regolith dominate the behaviour of scattered light (Hapke & Sato, 2015). Gravity signals emanating from the regolith layer are probably weaker compared to the signals from the remaining crust, and therefore the porosity of this upper layer is likely primarily estimated from extrapolation of the density profile of the underlying crust. Probably the upper regolith layer of regolith is affected more by weathering agents, meaning a larger flux at lower latitudes translates to the porosity estimations corresponding less to the real values. This argument is reinforced because we observe no latitudinal dependency of porosity in any model (Figure 5).

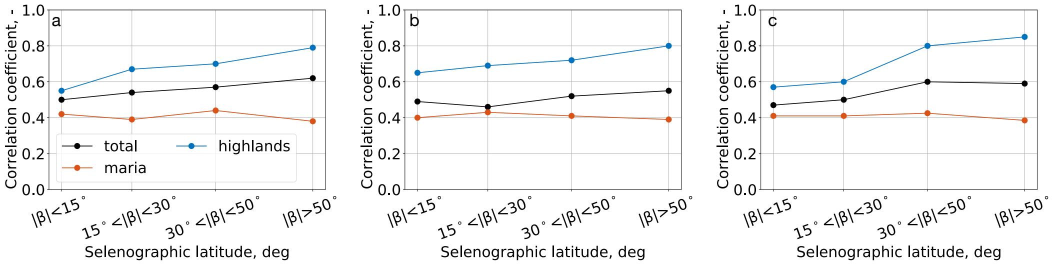

**Figure 10.** Nearside correlation between regolith albedo, polarisation-derived median grain size, and gravity-derived porosity of the Moon as a function of selenographic latitude. Correlations are calculated for $\theta_{\text{cap}} = 10^\circ$ for each latitude band between two parameters for a range of fixed values of the third; (a) albedo-porosity, (b) albedo-grain size, and (c) porosity-grain size.

Therefore, a decrease in triangular correlation with decreasing latitude may also be due to imprecise porosity estimations where the flux of weathering agents is high.

We presume that the basalt model in the lunar maria is not sufficient for its geological complex nature, and therefore we treat the results in the maria with some caution.

## 4.3 Theoretical Density Models for Moon's Crust

For the lunar highlands we have employed a linear density-with-depth model. However, other models, such as an exponential density-with-depth model, are more physically meaningful for increasing density due to compaction (Han et al., 2014). Goossens et al. (2020) have compared results in the lunar highlands for the linear and exponential density-with-depth models and concluded that surface densities resulting from the linear model appear more reasonable. Furthermore, since the lunar nearside are substantially covered by maria the linear model can handle density inversions and can distinguish between mare and non-mare regions (Besserer et al., 2014), whereas the exponential model breaks down in regions where density decreases with depth.

For the lunar maria we have employed a two-layered basalt-crust model. Previous studies into the Moon's crustal structure have commonly omitted the mare regions in their analysis. For the mare regions in our surface porosity models (Figure 5) we mostly observe a very high ($> 30\%$) or negative surface porosity, while a porosity of 6-11% is expected (Kiefer et al., 2012). Furthermore, correlation of mare porosity with polarimetry is low compared to the highlands. Therefore, we can conclude that either the two-layered basalt model may not be sufficient to model the geologic complex maria, or our model parameters are incorrect.

The model-argument is supported by the observed spectra not being precisely fitted by the theoretical spectra (Figure 1). The parameter-argument is split into two parts; one to account for incorrect basalt thickness, and one to account for incorrect assumptions for the crust underneath the basalts.

First, the basalt thickness map from degradation of partially-buried craters by Du et al. (2019) may be incomplete or incorrectly translated to a spatial map. Incompleteness of mapping of basalt thicknesses is supported by the observation of negative density gradients in our map (Figure 8). Lower basalt thicknesses naturally leads to larger basalt densities, and vice-versa, to account for the same gravity signals. A very large basalt density may result in negative porosity values, and very low basalt densities may result in very high porosity values (equation 8). We have varied the basalt thickness estimates of Du et al. (2019) with 50% around their nominal values, however, the differences in resulting surface porosity distributions are not noteworthy.

Second, we have assumed that the crust underneath the mare basalts are similar to highland crust (section 2.1.2). However, if the crust underneath a mare region differs from highland crust, the estimated basalt density is inherently affected to account for the same gravity signals. For example, Gong et al. (2016) have estimated the crust underneath Mare Imbrium to be abnormally high in density (about 3000 kg/m$^3$). Since we have assumed a lower-density crust (about 2400 kg/m$^3$), our estimates for basalt density could therefore be too large to compensate for the high crustal density.

The effective density requires high correlation between gravity and topography (section 2.1.1). For highland regions this correlation remains very high ($> 0.9$) for the spherical harmonic degree range of 250-650 (Figure 1). However, in mare regions this correlation drops 0.9 for spherical harmonic degrees $> 500$. This decrease in correlation could also be a factor of less-accurate density estimates in the lunar maria. Further studies could decide to determine the spherical harmonic degree range used for fitting of theoretical density models based on correlation between gravity and topography.

## 4.4 Possible Causes for Non-unity Correlation

Apart from effects of space weathering and grain shape (section 4.2), and the admissibility of the density-with-depth models (section 4.3), we elaborate here upon other possible causes for non-unity triangular correlation.

First, variations of regolith grain size are modelled in terms of the *median* grain size of regolith in an area. It may well be that the light scattering properties of regolith are affected by grains that deviate in size from the area's median. Additionally, each albedo, porosity, and grain size data point is spaced on a latitude and longitude grid by 1°, corresponding to a spatial resolution of 30 km. It remains undetermined how large the variations in these properties are, which may affect the obtained correlations between albedo, porosity, and grain size.

Second, some areas on the lunar surface may be covered by a negligible regolith layer, or bare rock is exposed at the surface. This means that the estimated regolith properties are unsuitable for these areas, which may cause a decrease in triangular correlation. These areas are most commonly located at mountain ranges or crater rims (Hapke & Sato, 2015). The immature regolith in these areas have large median grain size ( $>$ 110 µm, Figure 6), and since we require a sufficient amount of data points for each fixed-parameter set, median grain sizes larger than 100 µm remain inevitably untreated (section 2.3).

Third, apart from grain size and porosity, other physical parameters of regolith also affect the scattering behaviour of light, including grain shape, composition, and surface roughness, which could cause the obtained correlations to deviate from unity. We expect that grain size and regolith porosity accurately describes the photometric properties of regolith, as the grain size influences photometric properties of individual grains, and regolith porosity considers the photometric properties of all grains that make up the regolith layer. Additionally, grain size and porosity are affected by grain shape, composition, and surface roughness (Kar et al., 2016; Labarre et al., 2017), and therefore the latter properties are indirectly included in our analysis. As discussed, grain shape may influence the obtained correlations up to 20%.

Finally, individual grains have been assumed compact or solid, however, the grains in a regolith layer may be porous as well, which in turn affects composition through variations in complex refractive indices (Sen et al., 2017). Furthermore, it is unknown how the albedo of a single constituent grain is related to the surface albedo of the regolith on the Moon.

### 4.5 Polarimetric Limitations

Hitherto, we have presented and discussed correlations between the *nearside* gravity field and reflected surface sunlight, primarily because lunar polarimetry has never been carried out from lunar orbit (Jeong et al., 2015). The observations used in this study are taken by Earth-based telescopes, which are not exposed to the lunar farside due to the synchronous rotation of the Moon around Earth (Srivastava & Varatharajan, 2016).

However, the Wide-Angle Polarimetry Camera (PolCam) onboard Korea Pathfinder Lunar Orbiter (KPLO) is scheduled to launch in July 2022 and will measure the polarimetric properties of the lunar surface from orbit for the first time (Sim et al., 2020). These observations can extend this study by including farside observations, and since the farside is dominated by highlands (Petro & Pieters, 2004), our method is expected to work well for the farside.

Furthermore, polarimetry from lunar orbit will cover a large range of phase angles resulting in global high-resolution polarimetric phase curves of the Moon's surface. Photometric modelling of these curves allows for inversion of physical properties of lunar regolith such as porosity (Hapke & Sato, 2015). Polarimetric-derived porosity can be translated to surface density (section 2.1.4), which can directly serve as surface constraints to the density structures resulting from the gravity field.

# 5 Conclusion

We have determined vertical and lateral density distributions of the Moon's crust from the gravity field by means of localisation. The high-resolution GRGM1200B RM1 $\lambda = 10$ gravity model has a stable global effective density spectrum up to spherical harmonic degree $l = 650$, after which the correlation between gravity and topography decreases rapidly. The variations in the effective density spectrum can be used to infer vertical density variations in the Moon's crust. We used a localised spectral analysis to determine lateral variations in the Moon's crust by determining local effective density spectra for areas on the Moon. Subsequently, we fitted theoretical models for density variation with depth to these spectra and determined the surface density and density gradient from the localised spectra. We applied different theoretical models in the maria and highlands: one where a high-density basalt overlies a lower-density crust (maria), and one where density varies linearly with depth (highlands). We constructed the localisation windows as a spherical cap and varied its radius from 150 to 2150 km, which resulted in ample vertical and lateral density distributions of the Moon's crust.

Subsequently, we determined the median grain size of lunar regolith from albedo and polarisation degree distributions of the Moon's surface. Since these polarimetric observations are taken by Earth-based telescopes we are limited to analysis of the nearside because the Moon is in tidal-lock with Earth. We exploit the anti-correlation between albedo and polarisation degree to calculate the polarimetric anomaly, which can be linked to the median grain size of the regolith by means of an empirical relationship, established by rock and soil samples brought back from the Moon. The exact values of median grain size resulting from this empirical relationship should be treated with some care, however, the overall variation is admissible.

We presented a median grain size map of the lunar nearside and is broadly consistent with earlier findings, albeit a small shift in median grain size due to a new set of empirical parameters determined in this study. Overall, median grain size are larger in the maria than in the highlands, probably the difference in composition results in an increased sensitivity to comminution due to continuous bombardment of weathering agents in the highlands compared to the maria.

Next, we translated surface density estimates from our vertical and lateral density profiles to surface porosity by accounting the difference in bulk density and grain density to be due to porosity closures. Since high correlations between albedo, porosity, and grain size have been found in laboratory photometry of regolith analogues, we re-evaluated these for the lunar nearside by a triangular correlation study between gravimetry-derived porosity, polarimetry-derived grain size, and albedo. We found that the scattering properties of lunar regolith are very similar to those of regolith analogues on Earth.

From the degree of triangular correlation between these three aforementioned parameters we could constrain the possible density profiles resulting from the gravity field, and found a tendency for small localisation windows (300-450 km radius) to be most accurate with polarimetry. The constrained density structure of the Moon's crust resulted in highland surface densities of $2396 \pm 33$ kg/m$^3$ and mare surface densities averaging at $2565 \pm 72$ kg/m$^3$. Highland estimates are slightly larger (+72 kg/m$^3$) than previously determined by Goossens et al. (2020), while mare estimates are much lower ($-271$ kg/m$^3$), albeit a large uncertainty we attributed to the geologically complex nature of the maria.

We investigated the influence of other physical properties of regolith such as grain shape, and observed an influence to the triangular correlation of 20% to be due to grain shape. Other parameters such as composition and surface roughness are indirectly included since grain size and porosity are affected by these. We found that our analysis performs well for the lunar highlands and has limited applicability for the lunar maria, probably due to its geological complexity.

Global lunar polarimetry observation missions are designed to launch in the near present, and allows for extension of this analysis for the lunar farside. Since the farside is dominated by highlands we expect that our method is suitable here. These missions will cover a large range of phase angles, which enables surface density to be directly inferred from polarimetry, and will likely add more constraints the Moon's crustal density structure.

**Acknowledgments**

The gravity data used in this study is available in the Geosciences Node of the NASA Planetary Data System, as well as the Planetary Geodynamics Data Archive of NASA GSFC (Goossens et al., 2020). The polarisation data used in this study is available in FITS files format as online-only material (Jeong et al., 2015). We used the freely available SHTools software for localisation (Wieczorek & Meschede, 2018). Courtesy to Fabio Crameri for the perceptually uniform scientific colormaps that are used for all figures (Crameri et al., 2020). We sincerely thank Daphne Stam for discussions about lunar polarimetry and Shengxia Gong for assistance with implementation of the mare basalt model.

# References

Benesty, J., Chen, J., Huang, Y., & Cohen, I. (2009). *Noise Reduction in Speech Processing - Pearson Correlation Coefficient.* Springer-Verlag Berlin Heidelberg.

Besserer, J., Nimmo, F., Wieczorek, M., Weber, R., Kiefer, W., McGovern, P., … Zuber, M. (2014). GRAIL gravity constraints on the vertical and lateral density structure of the lunar crust. *Geophysical Research Letters*, *41*(16), 5771-5777.

Crameri, F., Shephard, G., & Heron, P. (2020). The misuse of colour in science communication. *Nature Communications*, *11*(1), 5444.

Deutsch, A., Neumann, G., Head, J., & Wilson, L. (2019). GRAIL-identified gravity anomalies in Oceanus Procellarum: Insight into subsurface impact and magmatic structures on the Moon. *Icarus*, *331*, 192–208.

Dollfus, A. (1998). Lunar Surface Imaging Polarimetry: I. Roughness and Grain Size. *Icarus*, *136*(1), 69 - 103.

Dollfus, A., & Bowell, E. (1971, January). Polarimetric Properties of the Lunar Surface and its Interpretation. Part I. Telescopic Observations. , *10*, 29.

Du, J., Fa, W., Wieczorek, M., Xie, M., Cai, Y., & Zhu, M. (2019). Thickness of Lunar Mare Basalts: New Results Based on Modeling the Degradation of Partially Buried Craters. *Journal of Geophysical Research. Planets*, *124*(9), 2430-2459.

Engelhardt, W. v., Hurrle, H., & Luft, E. (1976, April). Microimpact-induced changes of textural parameters and modal composition of the lunar regolith. *Lunar and Planetary Science Conference Proceedings*, *1*, 373-392.

Fa, W., & Wieczorek, M. (2012). Regolith thickness over the lunar nearside: Results from earth-based 70-cm arecibo radar observations. *Icarus*, *218*(2), 771-787.

Gong, S., Wieczorek, M., Nimmo, F., Kiefer, W., Head, J., Huang, C., … Zuber, M. (2016). Thicknesses of mare basalts on the Moon from gravity and topography. *Geophysical Research Letters*, *121*, 854-870.

Goossens, S., Sabaka, T., Wieczorek, M., Neumann, G., Mazarico, E., Lemoine, F., … Zuber, M. (2020, 11). High Resolution Gravity Field Models from GRAIL Data and Implications for Models of the Density Structure of the Moon's Crust. *Journal of Geophysical Research: Planets*, *125*.

Han, S., Schmerr, N., Neumann, G., & Holmes, S. (2014). Global characteristics of porosity and density stratification within the lunar crust from GRAIL gravity and Lunar Orbiter Laser Altimeter topography data. *Geophysical Research Letters*, *41*(6), 1882-1889.

Hapke, B. (2008). Bidirectional reflectance spectroscopy: 6. Effects of porosity. *Icarus*, *195*(2), 918 - 926.

Hapke, B., & Sato, H. (2015). The porosity of the upper lunar regolith. *Icarus*, *273*, 75 - 83.

Hemingway, D., Garrick-Bethell, I., & Kreslavsky, M. (2015). Latitudinal variation in spectral properties of the lunar maria and implications for space weathering. *Icarus*, *261*, 66-79.

Hilst, R. v. d., Simons, F., & Zuber, M. (2002). The Earth's Gravitational Field. In *Essentials of Geophysics - Lecture Notes.* Massachusetts Institute of Technology.

Horz, F., Cintala, M., & See, T. (1984, 02). Grainsize evolution and differential comminution in an experimental regolith.

Huang, Q., & Wieczorek, M. (2012). Density and porosity of the lunar crust from gravity and topography. *Journal of Geophysical Research: Planets*, *117*(E5).

Jeong, M., Kim, S., Garrick-Bethell, I., Park, S., Sim, C. K., Jin, H., … Choi, Y. (2015, nov). Multi-band Polarimetry of the Lunar Surface. I. Global Properties. *The Astrophysical Journal Supplement Series*, *221*(1), 16.

Kaasalainen, S. (2003). Laboratory photometry of planetary regolith analogs - i. effects of grain and packing properties on opposition effect. *Astronomy & Astrophysics*, *409*(2), 765-769.

Kar, A., Sen, A., & Gupta, R. (2016). Laboratory photometry of regolith analogues: Effect of porosity. *Icarus*, *277*, 300 - 310.

Kar, A., Sen, A., & Gupta, R. (2020). ”laboratory photometry of regolith analogues: Effect of porosity-ii”. *Icarus*, 114211.

Kiefer, W., Macke, R., Britt, D., Irving, A., & Consolmagno, G. (2012). The density and porosity of lunar rocks. *Geophysical Research Letters*, *39*(7).

Labarre, S., Ferrari, C., & Jacquemoud, S. (2017, 03). Surface roughness retrieval by inversion of the hapke model: A multiscale approach. *Icarus*, *290*, 63-80.

Lissauer, J., & Pater, I. d. (2013). *Fundamental Planetary Science - Physics, Chemistry and Habitability.* Cambridge University Press.

Nelson, D. M., Koeber, S. D., Daud, K., Robinson, M. S., Watters, T. R., Banks, M. E., & Williams, N. R. (2014, March). Mapping Lunar Maria Extents and Lobate Scarps Using LROC Image Products. In *Lunar and planetary science conference* (p. 2861).

Ogolo, N., Akinboro, O., Inam, J., Akpokere, F., & Onyekonwu, M. (2015, 08). Effect of grain size on porosity revisited.. doi: 10.2118/178296-MS

Papike, J., Ryder, G., & Shearer, C. (1998). Lunar Samples. *Reviews in Mineralogy and Geochemistry*, *36*, 5.1-5.234.

Petro, N., & Pieters, C. (2004, 06). Surviving the heavy bombardment: Ancient material at the surface of South Pole-Aitken Basin. *J. Geophys. Res*, *109*.

Pieters, C., Taylor, L., Noble, S., Keller, L., Hapke, B., Morris, R., … Wentworth, S. (2000, September). Space weathering on airless bodies: Resolving a mystery with lunar samples. *Meteoritics and Planetary Science*, *35*(5), 1101-1107.

Prettyman, T. H., Hagerty, J. J., Elphic, R. C., Feldman, W. C., Lawrence, D. J., McKinney, G. W., & Vaniman, D. T. (2006). Elemental composition of the lunar surface: Analysis of gamma ray spectroscopy data from Lunar Prospector. *Journal of Geophysical Research: Planets*, *111*(E12).

Sakai, T., & Nakamura, A. (2005). Quantification of porosity and surface roughness in laboratory measurements of the bidirectional reflectance of asteroid surface analogues. *Earth, Planets and Space*, *57*(1), 71-76.

Sen, A., Botet, R., Vilaplana, R., Choudhury, N. R., & Gupta, R. (2017). The effect of porosity of dust particles on polarization and color with special reference to comets.

*Journal of Quantitative Spectroscopy and Radiative Transfer*, *198*, 164-178.

Shepard, M. K., & Helfenstein, P. (2007). A test of the hapke photometric model. *Journal of Geophysical Research: Planets*, *112*(E3).

Shkuratov, Y., Kaydash, V., Korokhin, V., Velikodsky, Y., Opanasenko, N., & Videen, G. (2011). Optical measurements of the Moon as a tool to study its surface. *Planetary and Space Science*, *59*(13), 1326 - 1371.

Shkuratov, Y., & Opanasenko, N. (1992). Polarimetric and photometric properties of the moon: Telescope observation and laboratory simulation: 2. The positive polarization. *Icarus*, *99*(2), 468 - 484.

Shkuratov, Y., Opanasenko, N., & Korokhin, V. (2015). The Moon. In (p. 303-319). Cambridge University Press.

Shkuratov, Y., Opanasenko, N., Zubko, E., Grynko, Y., Korokhin, V., Pieters, C., ... Opanasenko, A. (2007). Multispectral polarimetry as a tool to investigate texture and chemistry of lunar regolith particles. *Icarus*, *187*(2), 406-416.

Shkuratov, Y., Stankevich, D., Petrov, D., Pinet, P., Cord, A., Daydou, Y., & Chevrel, S. (2005). Interpreting photometry of regolith-like surfaces with different topographies: shadowing and multiple scattering. *Icarus*, *173*(1), 3-15.

Sim, C., Kim, S., Jeong, M., Choi, Y., & Shkuratov, Y. (2020). Lunar Polarimetry from its Orbit with KPLO/POLCAM: Phase-angle Coverage. *Lunar and Planetary Science Conference*, *51*.

Srivastava, N., & Varatharajan, I. (2016). Geomorphology of Lowell crater region on the Moon. *Icarus*, *266*, 44-56.

Szekely, G., Rizzo, M., & Bakirov, N. (2007). Measuring and testing dependence by correlation of distances. *The Annals of Statistics*, *35*(6), 2769 – 2794.

Umov, N. (1905). Chromatische depolarisation durch Lichtzerstreuung. *Physikalische Zeitschrift*, *6*, 674-676.

Wieczorek, M. (2015, 01). Gravity and Topography of the Terrestrial Planets. *Treatise on Geophysics*(2), 153-193.

Wieczorek, M., & Meschede, M. (2018). SHTools: Tools for Working with Spherical Harmonics. *Geochemistry, Geophysics, Geosystems*, *19*(8), 2574-2592.

Wieczorek, M., Neumann, G., Nimmo, F., Kiefer, W., Taylor, G., Melosh, J., ... Zuber, M. (2013, 12). The crust of the moon as seen by GRAIL. *Science (New York, N.Y.)*, *339*.

Wieczorek, M., & Simons, F. (2005, sep). Localized spectral analysis on the sphere. *Geophysical Journal International*, *162*(3), 655–675.

Wieczorek, M., & Simons, F. (2007). Minimum-Variance Multitaper Spectral Estimation on the Sphere. *Journal of Fourier Analysis and Applications*, *13*(6), 665–692.

Zuber, M., Smith, D., Watkins, M., Asmar, S., Konopliv, A., Lemoine, F., ... Yuan, D. (2012, 12). Gravity Field of the Moon from the Gravity Recovery and Interior Laboratory (GRAIL) Mission. *Science (New York, N.Y.)*, *339*.

# 6 Supplementary Materials

## 6.1 Theoretical Density Models

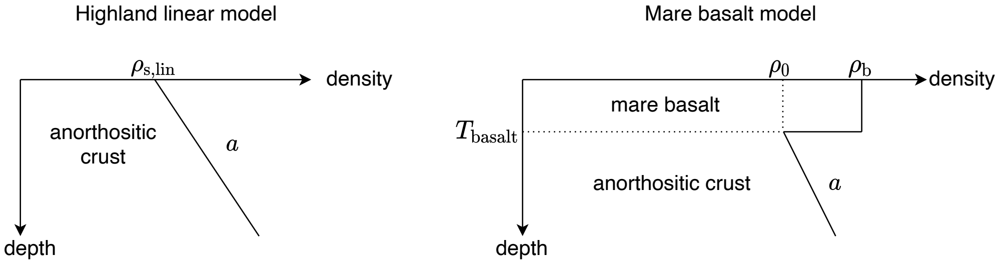
Highland linear model
$\rho_{\mathrm{s,lin}}$
density
anorthositic crust
$a$
depth
Mare basalt model
$\rho_0$
$\rho_{\mathrm{b}}$
density
mare basalt
$T_{\mathrm{basalt}}$
anorthositic crust
$a$
depth

**Figure S1.** Theoretical density models of the lunar highlands and maria. The highlands are modelled as density varying linearly with depth, with a surface density $\rho_{\mathrm{s,lin}}$ and density gradient $a$. The maria are modelled as a high-density basalt overlying a less-dense crust. The basalt has constant density $\rho_{\mathrm{b}}$ and thickness $T_{\mathrm{b}}$, and the crust underneath has an upper density of $\rho_0$ and density gradient $a$.

## 6.2 Pearson Correlation

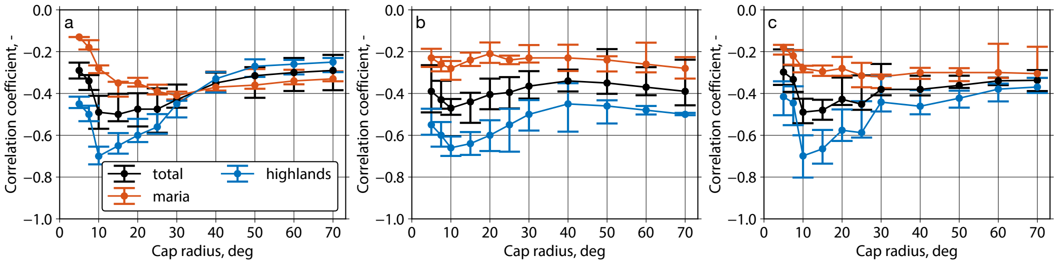

**Figure S2.** Nearside correlation between regolith albedo, polarisation-derived median grain size, and gravity-derived porosity of the Moon. Correlations are calculated between two parameters for a range of fixed values of the third; (a) albedo-porosity, (b) albedo-grain size, and (c) porosity-grain size. Correlation expressed as Pearson product-moment correlation coefficient (Szekely et al., 2007), and presented by median values (dots) and 25th and 75th percentiles (whiskers) as a function of localisation spherical cap radius.

# Part III

# Discussion and Conclusion

# 1

# Validation and Verification

Validation and verification steps that have been taken in this work are presented in this chapter. In Section 1.1 the steps are discussed for data preparation, followed by validation and verification of the median grain size estimates from lunar polarimetry in Section 1.2 and Section 1.3. Next, the theoretical density model employed in the maria is verified in Section 1.4. Finally, Section 1.5 presents the validation and verification of the linear density-with-depth model and the localisation approach.

## 1.1. Data Preparation

In this work use has been made of the verified software package Spherical Harmonic Tools (SHTools) Wieczorek and Meschede (2018). This is an archive of code that can be used to work with spherical harmonics, such as transformations, multitaper spectral analysis, expansions of coefficients to grid (and vice-versa), and standard operations on global gravitational data. The software package also included many verified and validated gravity and topography datasets such as the most recent ones of the Moon. Therefore, all spherical harmonic operations used for data preparation in this work are considered verified when using SHTools.

## 1.2. Comparison of Polarimetric Anomaly

In the manuscript the polarimetric anomaly is used to compute the median grain size through an empirical relationship. Therefore, median grain size estimates can partly be validated by comparison of the polarimetric anomaly and the empirical constants.

The polarimetric anomaly is compared to those made by Jeong et al. (2015) and Shkuratov et al. (2007), which are presented in Figure 1.1. The three images are in general agreement, in particular those made in this work and made by Jeong et al. (2015), even though the latter used a different albedo map from Velikodsky et al. (2011). The craters and shadows are more prominent in the polarimetric anomaly image by Shkuratov et al. (2007), which is thought to be due to their measurements being taken at one phase angle, and those by Jeong et al. (2015) at multiple phase angles (see Section 4.3).

An overview of the empirical constants determined in this study are given in Table 1.1, which are slightly different from those determined in previous studies for the same wavelength, which are also given in Table 1.1. The bias is slightly lower, but combined with a larger trend the regression lines are fairly similar, as we presented in the manuscript. The constant $a \neq 1$ means that there is a small dependence of Stokes $Q$ on $A$.

## 1.3. Median Grain Size Estimates

### By Comparison with Jeong et al. (2015)

The median grain size map presented in the manuscript is compared to the map obtained by Jeong et al. (2015). Both maps are in overall agreement; larger values in the lunar maria than in the highlands; a clear latitudinal dependency; craters show up as larger grain size values compared to their surroundings. Even though Jeong et al. (2015) used a different value for $a$ based on Shkuratov and

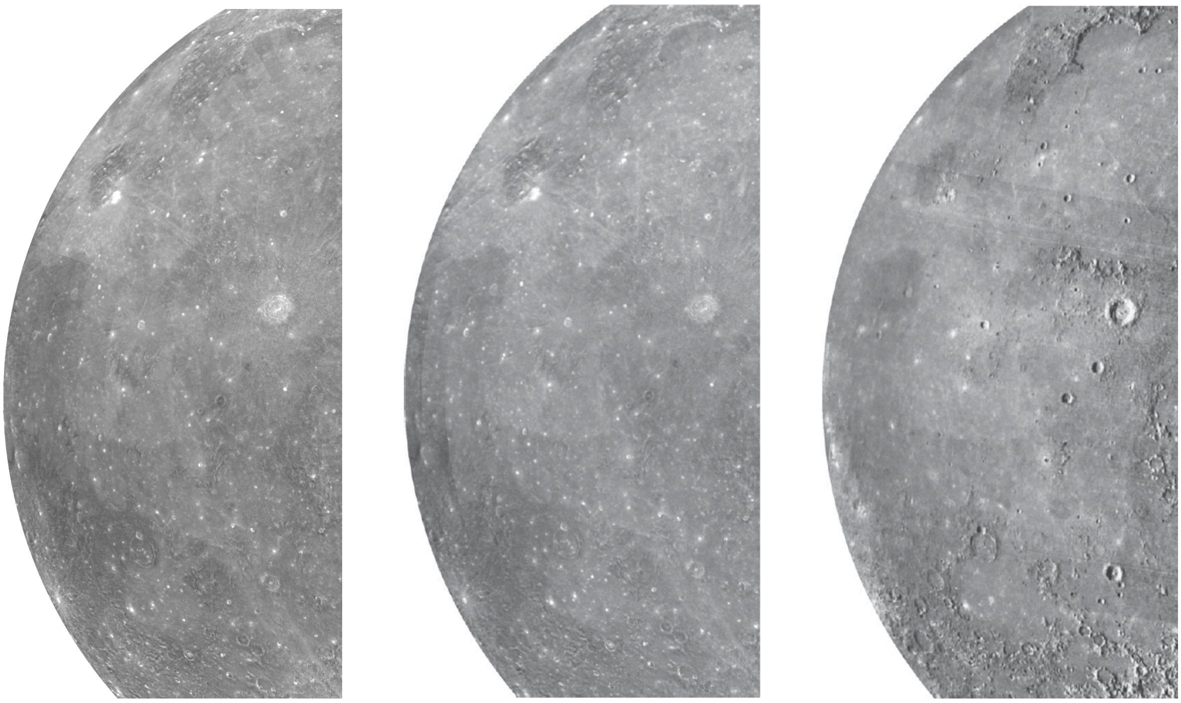

(a) B-band (b) Jeong et al. (2015) (c) Shkuratov et al. (2007)

Figure 1.1: Comparison of the polarimetric anomaly $(P_{\max})^a A$ between the (a) B-band polarimetry with $a = 0.795$, (b) same B-band polarimetry by Jeong et al. (2015), and (c) 420 nm polarimetry by Shkuratov et al. (2007), for the western portion of the lunar disk. Light colors represent a higher value for the polarimetric anomaly, and vice-versa.

Table 1.1: Determined empirical constants $a$ and $b$ with corresponding wavelength used for the regression line in log-log scale between albedo and maximum polarisation.

| $a$ | $b$ | Wavelength, nm | Source |
|---|---|---|---|
| 0.724 | -1.81 | 600 | Dollfus and Bowell (1971) |
| 0.845 | -1.801 | 630 | Shkuratov and Opanasenko (1992) |
| 0.795 | -1.871 | 430 | |
| $0.8294 \pm 0.0007$ | $-1.885 \pm 0.002$ | 630 | see manuscript |

Table 1.2: Median grain size of Apollo soil samples and estimates at the Apollo landing site locations, for both $a = 0.8294 \pm 0.0007$ and $a = 0.845$ at 630 nm, together with polarimetric properties $A$ and $P_{\max}$. An assumed uncertainty of $\delta a = 0.001$ is assumed for the latter $a$ value.

| Mission site | $d$, μm | | | $A$, % | $P_{\max}$, ‰ |
|---|---|---|---|---|---|
| | soil samples | $a = 0.8294$ | $a = 0.845$ | | |
| Apollo 11 | 64 | $81 \pm 4$ | $89 \pm 6$ | $9.53 \pm 0.08$ | $127 \pm 1$ |
| Apollo 12 | 80-96 | $79 \pm 4$ | $87 \pm 6$ | $10.14 \pm 0.08$ | $115.5 \pm 0.9$ |
| Apollo 14 | 64 | $67 \pm 3$ | $73 \pm 4$ | $12.9 \pm 0.1$ | $74.2 \pm 0.6$ |
| Apollo 15 | 52-86 | $73 \pm 1$ | $79 \pm 1$ | $11.36 \pm 0.09$ | $92.7 \pm 0.7$ |
| Apollo 16 | 78 | $73 \pm 2$ | $79 \pm 4$ | $19.8 \pm 0.2$ | $48.1 \pm 0.4$ |
| Apollo 17 | 47-67 | $71 \pm 4$ | $77 \pm 7$ | $11.25 \pm 0.09$ | $91.5 \pm 0.7$ |

Opanasenko (1992), similar map values and features are observed. This is expected since the polarimetric anomalies in Figure 1.1 are in agreement as well, albeit at a different wavelength.

### By Comparison with Lunar Soil Samples

To check the validity of the procedure in determining the median grain size, the values for $d$ are compared to median grain size values of Apollo lunar soil samples which have been polarimetric analysed by Dollfus (1998), for both values of $a$ used in Jeong et al. (2015), and determined in this study. Median grain size estimates and polarimetric properties for Apollo mission site locations are presented in Table 1.2. Determination of the uncertainties is discussed in detail in Appendix B.

Comparing the median grain size estimates at the Apollo landing sites with samples obtained by the corresponding mission in Table 1.2, it is observed that the median grain size estimates are in general agreement with the values of the lunar soil samples at the Apollo sites on a logarithmic scale. The same holds for the polarimetric properties $A$ and $P_{\max}$ at those sites. Furthermore, there is a constant difference between the estimates using different values for $a$, however, the overall variation of the grain size estimates is similar.

## 1.4. Mare Basalt Model

The mare basalt model introduced in the manuscript is verified by analysing the influence of various model parameters to ensure proper implementation. Theoretical effective density profiles are generated for various model parameters and are presented in Figure 1.2.

As can be seen in Figure 1.2, the effect of various model parameters on the theoretical effective density profile is clearly visible. Similar plots have been presented by Gong et al. (2016).

First, the upward trend of the effective density with increasing upper crustal density in 1.2a is expected since the surface density acts as a bias to the effective density. It can be seen that the effective density profile asymptotically approaches $\rho_0$ for increasing spherical harmonic degree.

Second, 1.2b shows a decreasing effective density profile with spherical harmonic degree for positive linear density gradients, and vice-versa for negative linear density gradients. This is expected since increasing spherical harmonic degrees are associated with decreasing depths below the surface (see manuscript). Therefore, a decreasing effective density with spherical harmonic degree translates to increasing density with depth, as is the case for a positive density gradient, and vice-versa. It is noted that a zero density gradient does not result in a constant effective density with spherical harmonic degree, but in an increasing effective density profile with spherical harmonic degree. This is the case since a dense mare basalt overlies the lower-density crust, and therefore the density profile increases towards the surface.

Third, an increasing basalt density influences the minimum point of the effective density profile, as can be seen from 1.2c. The density profile for a dense mare basalt overlying a lower-density crust with increasing density with depth is composed into a decreasing and subsequent increasing profile with spherical harmonic degree. An increasing basalt density thus results in a density increase at lower degrees with the same basalt thickness and upper crustal density, which is observed in 1.2c. However, the overall influence of the basalt density on the resulting effective density profile is smaller than for the upper crustal density.

Finally, an increasing basalt thickness exerts influence on the slope of the effective density profile,

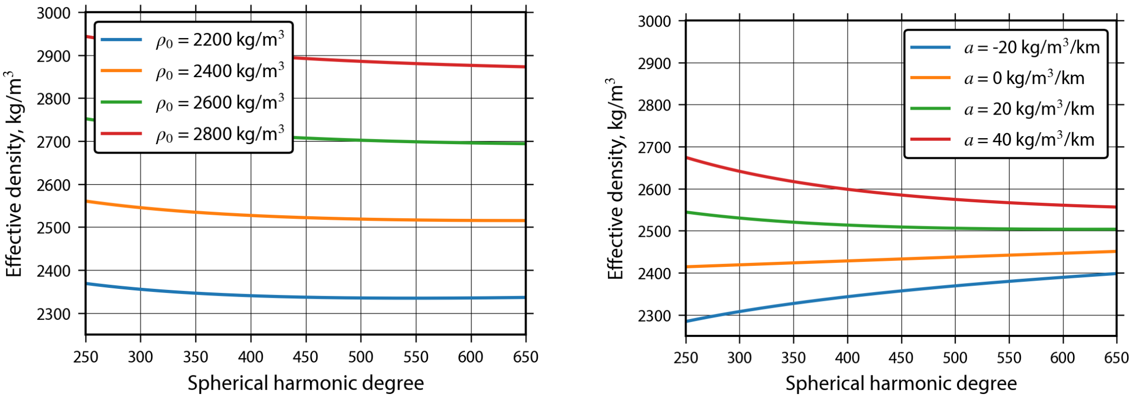

(a) Upper crustal density

(b) Crustal linear density gradient

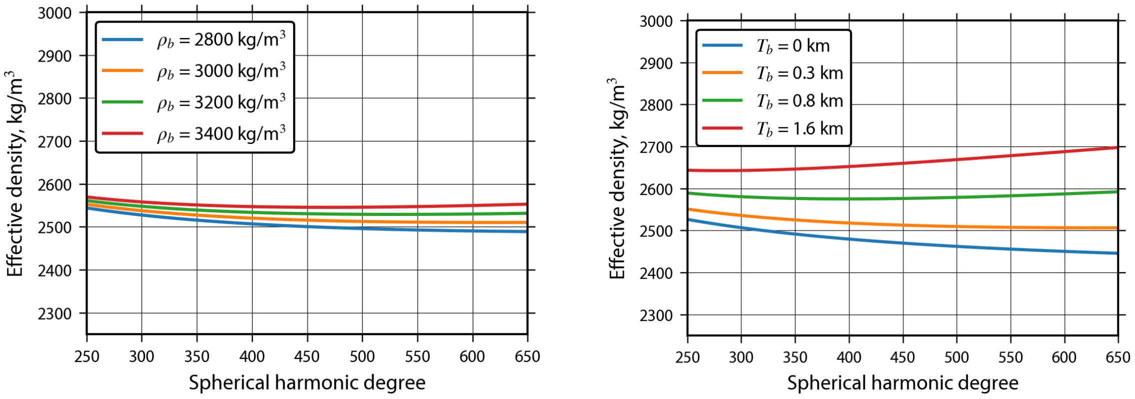

(c) Basalt density

(d) Basalt thickness

Figure 1.2: Theoretical effective density for various upper crustal densities (a), crustal linear density gradients (b), basalt densities (c), and basalt thicknesses (d) for the two-layer density model. Unless stated otherwise, an upper crustal density $\rho_0 = 2390$ kg/m$^3$, crustal linear density gradient $a = 21$ kg/m$^3$/km, basalt density $\rho_b = 2963$ kg/m$^3$, and basalt thickness $T_b = 0.3$ km is used for the model (Gong et al., 2016).

as observed in 1.2d. With no basalt layer ($T_{\mathrm{basalt}} = 0$ km), a decreasing effective density with increasing spherical harmonic degree is observed, corresponding to an increasing density with depth profile, as expected for a positive crustal density gradient. However, as the basalt thickness increases, the slope of the effective density profile changes, ultimately to an increasing effective density with spherical harmonic degree for larger $T_{\mathrm{basalt}}$ ($\gtrapprox 0.8$ km). This is expected since a thicker dense basalt layer means a larger density exists at greater depths, corresponding to an increase in effective density at lower degrees with increasing $T_{\mathrm{basalt}}$.

In conclusion, the plots and observations presented here are implemented correctly and have also been reported by Gong et al. (2016). Therefore, the mare theoretical density profile is considered verified and can be fitted to the observations to model the vertical and lateral density distribution in the maria.

## 1.5. Highland Linear Model and Spectral Localisation Approach

Validation of the localisation analysis method is achieved by providing the same input to the localisation code as Goossens et al. (2020). The input parameters include cap radius $\theta_{\mathrm{cap}}$, degree bandwidth $l_{\mathrm{win}}$ and the grid resolution $r$. For the degree range $250 \leq l \leq 650$ Goossens et al. (2020) present maps for $r = 5^{\circ}$, $\theta_{\mathrm{cap}} = 15.0^{\circ}$, $l_{\mathrm{win}} = 58$ and $r = 5^{\circ}$, $\theta_{\mathrm{cap}} = 7.5^{\circ}$, $l_{\mathrm{win}} = 116$.

The aforementioned validation parameters are provided as input to the localisation code. The results are presented in Figure 1.3.

Goossens et al. (2020) found for $\theta_{\mathrm{cap}} = 15.0^{\circ}$ and $l_{\mathrm{win}} = 58$ that the lunar maria have higher values for the surface density, around 2600-2700 kg/m$^3$, and negative density gradients of approximately -50 kg/m$^3$/km. The highlands on the nearside were found to have lower surface densities of approximately 2300 kg/m$^3$, and positive density gradients of around 20-40 kg/m$^3$/km. A higher surface density near 2800 km/m$^3$ was found for the northern part of Mare Imbrium and the northern and eastern parts of Oceanus Procellarum, and a lower surface density between Mare Insularum and Mare Cognitum of 2000 kg/m$^3$. Two extremes of the density gradient (approximately $\pm 80$ kg/m$^3$/km) had been found inside Mare Imbrium. The same observations can be concluded from Figure 1.3a and Figure 1.3b.

Furthermore, the findings by Goossens et al. (2020) for $\theta_{\mathrm{cap}} = 7.5^{\circ}$ and $l_{\mathrm{win}} = 116$ show a larger contrast between the lunar maria and the highlands than for the previous case; surface densities of 2800-3000 kg/m$^3$ in the maria and surface densities in the highlands of approximately 2300-2400 kg/m$^3$. The density gradient show more extreme values and is more heterogeneous than for a larger cap radius. Overall, the same structures and values are observed in Figure 1.3c, Figure 1.3d, and Goossens et al. (2020). Particularly, the negative and positive density gradient patterns, the six positions of low surface density, and the large surface density patterns in Mare Imbrium and Oceanus Procellarum.

In conclusion, the results shown by Goossens et al. (2020) can be reproduced by providing the same input parameters to the localisation code.

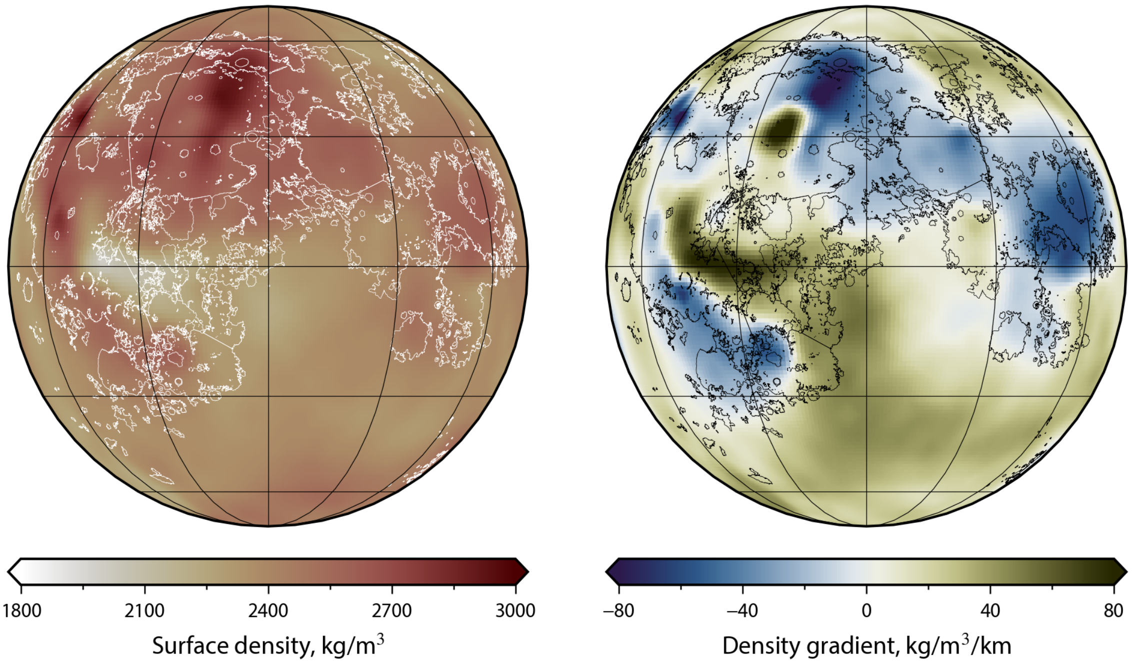

(a) $r = 5°$, $\theta_{\text{cap}} = 15.0°$, $l_{\text{win}} = 58$ (b) $r = 5°$, $\theta_{\text{cap}} = 15.0°$, $l_{\text{win}} = 58$

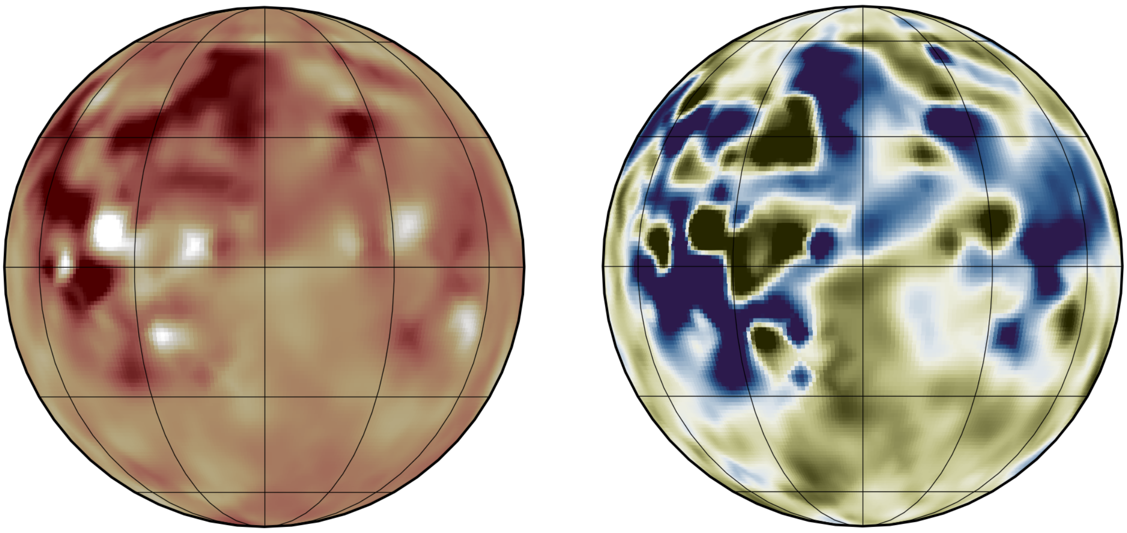

(c) $r = 5°$, $\theta_{\text{cap}} = 7.5°$, $l_{\text{win}} = 116$ (d) $r = 5°$, $\theta_{\text{cap}} = 7.5°$, $l_{\text{win}} = 116$

Figure 1.3: Validation of nearside linear surface density (a,c) and linear density gradient (b,d) estimates of the Moon. Lateral variations determined by a multitaper approach where 30 spherical caps are 99% concentrated each $r$ degrees in latitude and longitude, with various cap radii $\theta_{\text{cap}}$ and bandwidth $l_{\text{win}}$ indicated in the subcaptions. The same input parameters as used by Goossens et al. (2020) are used. Maps are presented in an orthographic projection centered on 0° longitude. Boundaries of the lunar maria are indicated by in (a) and (b) by a solid white and black line, respectively.

# 2

# Supplementary Discussion

In addition to the discussions presented in the manuscript, other discussion that are not in the scope of the manuscript are presented here. Section 2.1 will elaborate upon the different polarimetric behaviour of the lunar maria and highlands. The density modelling approach is discussed in Section 2.2, together with a discussion about the effect of crustal thickness variations. Next, Section 2.3 will discuss the robustness of the localised spectral approach, after which the possibility of inaccuracies in the albedo observations is discussed in Section 2.4. Finally, the determination and sensitivity of basalt thickness estimates is discussed in Section 2.5.

## 2.1. The Different Behaviour of the Lunar Maria and Highlands

The total distributions of albedo and maximum polarisation degree are presented in Figure 2.1, and it can be seen that these are clearly bimodal due to the different behaviour of the maria and highlands in $A$- and $P_{\text{max}}$-space. Therefore, it is desirable to separate the analysis for the aforementioned regions.

In order to distinguish the $A$ and $P_{\text{max}}$ values for the maria and the highlands, use has been made of the polygon vector map from the Lunar Reconnaissance Orbiter Camera (LROC) (Nelson et al., 2014), which is presented in Figure 2.2.

The anti-correlation observed in the albedo and maximum polarisation images presented in the manuscript is further expanded upon by presenting box-and-whisker plots for all bands, presented in Figure 2.3. It can be seen that for all bands, albedo values are significantly higher for the maria than for the highlands, and vice-versa for the maximum polarisation values. The 75th percentile boundaries do not overlap for all bands for both $A$ and $P_{\text{max}}$, and this separation is even larger for $P_{\text{max}}$ than $A$. Furthermore, an increasing wavelength results in increasing albedo values and decreasing maximum polarisation values, which is thought to be due to more transparent grains for larger wavelength, and a larger portion of the reflected light is multiply scattered (Jeong et al., 2015).

The box-and-whisker plots are nearly identical to those presented by Jeong et al. (2015). The only difference in the distributions presented by Jeong et al. (2015) is the smaller length of the whiskers for each box, meaning that the standard deviation of the $A$ and $P_{\text{max}}$ distributions for each band are smaller. An explanation may be that Jeong et al. (2015) use a different approach to separate maria and highlands regions, namely based on the bimodal FeO distribution, estimated by taking the ratio of two albedo bands. The classification of aforementioned regions was based on two empirical FeO content values, and values in between were not treated in their analysis. Thus, since their classification is based solely on albedo, and regions that they were uncertain of were left out, it is expected that a larger separation between the box-and-whisker plots through a smaller standard deviation is expected.

## 2.2. Modelling Approach and Effect of Crustal Thickness Variations

The lunar crust is decomposed in a series of thin constant density layers, as depicted by Figure 2.4. The crust has a surface topography $h(x)$ and a depth-only density distribution $\rho(z)$, where $z$ is the depth below the surface, and $x$ an arbitrary lateral coordinate. A Cartesian geometry is a valid assumption for as the sphericity of the Moon is negligible for the short-wavelength analysis in this work (Besserer et al., 2014).

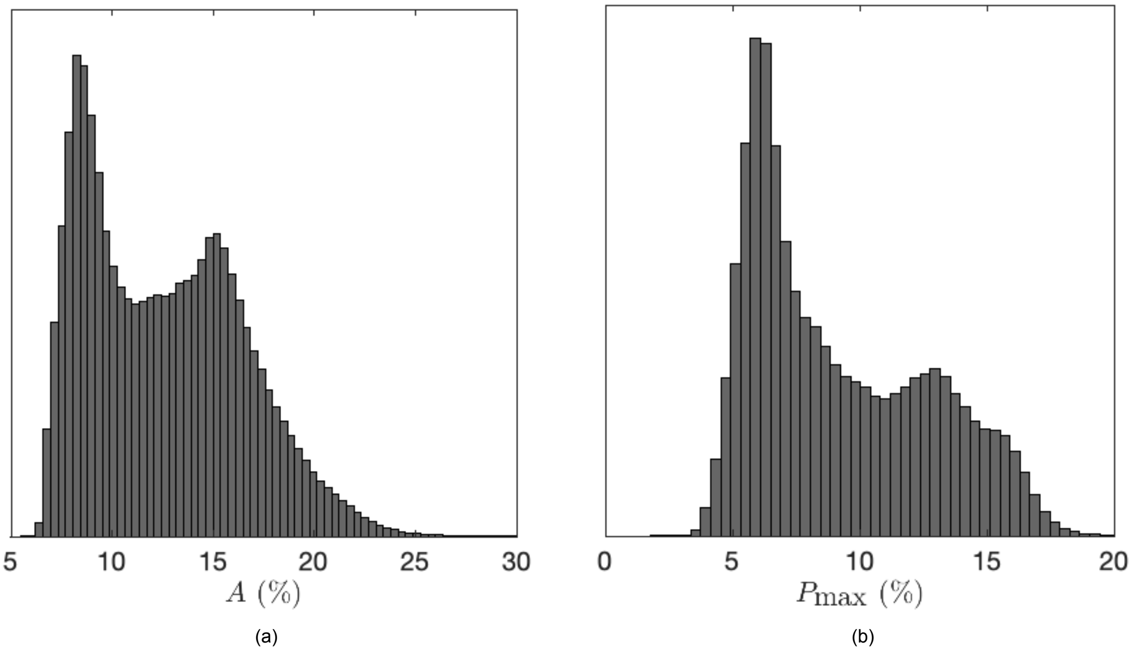

(a)

(b)

Figure 2.1: Total nearside (a) albedo- and (b) maximum polarisation distributions of the Moon.

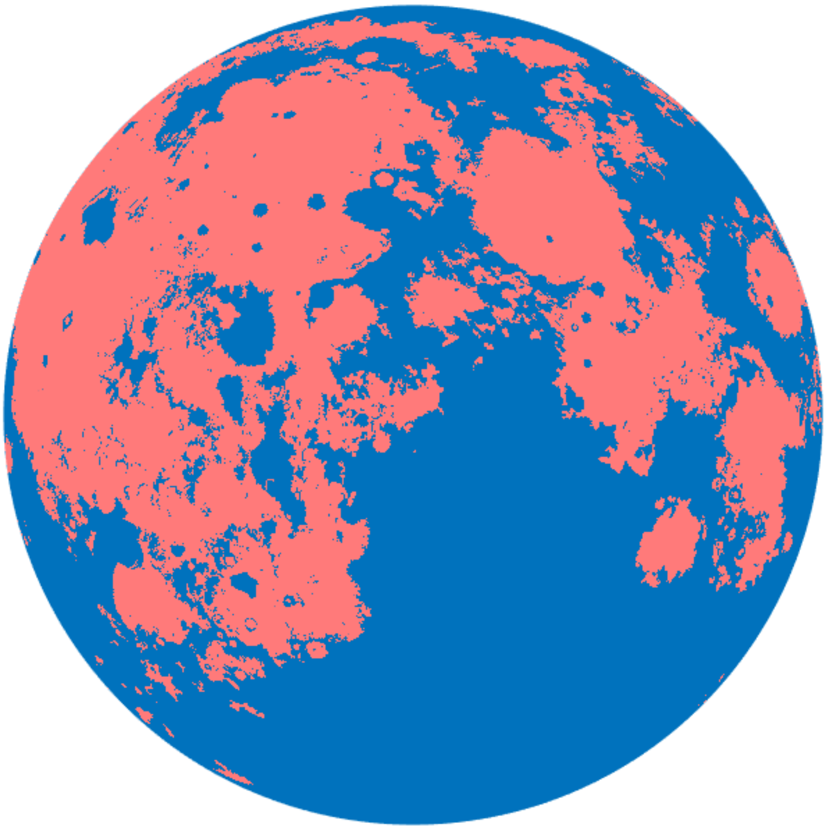

Figure 2.2: Nearside maria (red) and highlands (blue) regions of the Moon (Nelson et al., 2014). The map is presented in an orthographic projection centered on 0° longitude.

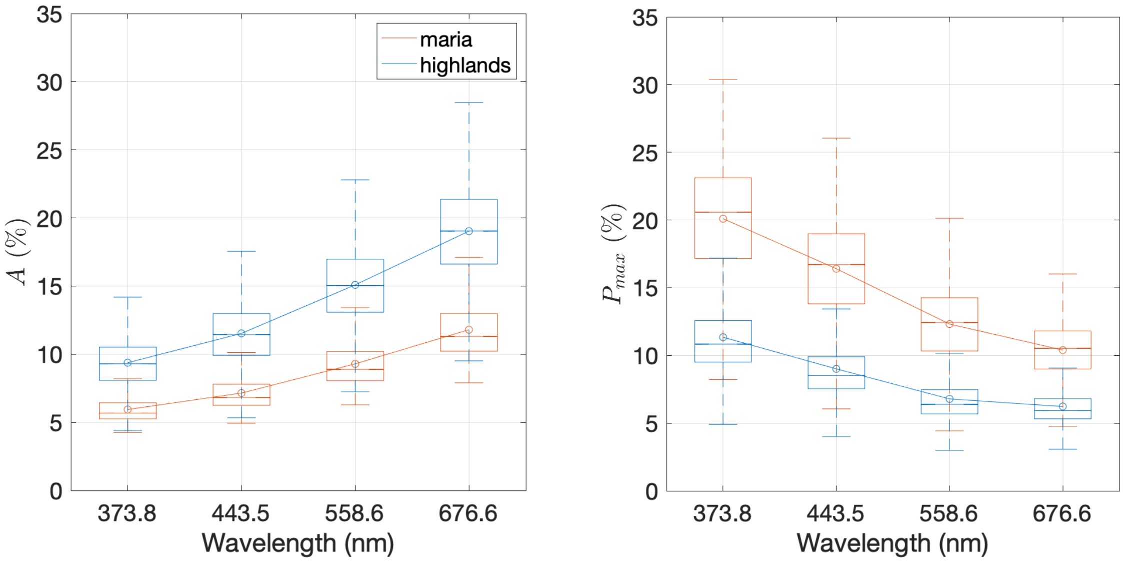

(a) (b)

Figure 2.3: Box-and-whisker plots of nearside albedo (a) and maximum polarisation (b) for the maria (red) and highlands (blue) of the Moon, as a function of central wavelength of the four bands. The central lines within the boxes are the median values, the boxes range from 25th to 75th percentiles, and the whiskers range from 5th to 95th percentiles. The mean values are represented by open circles, and are connected by a solid line.

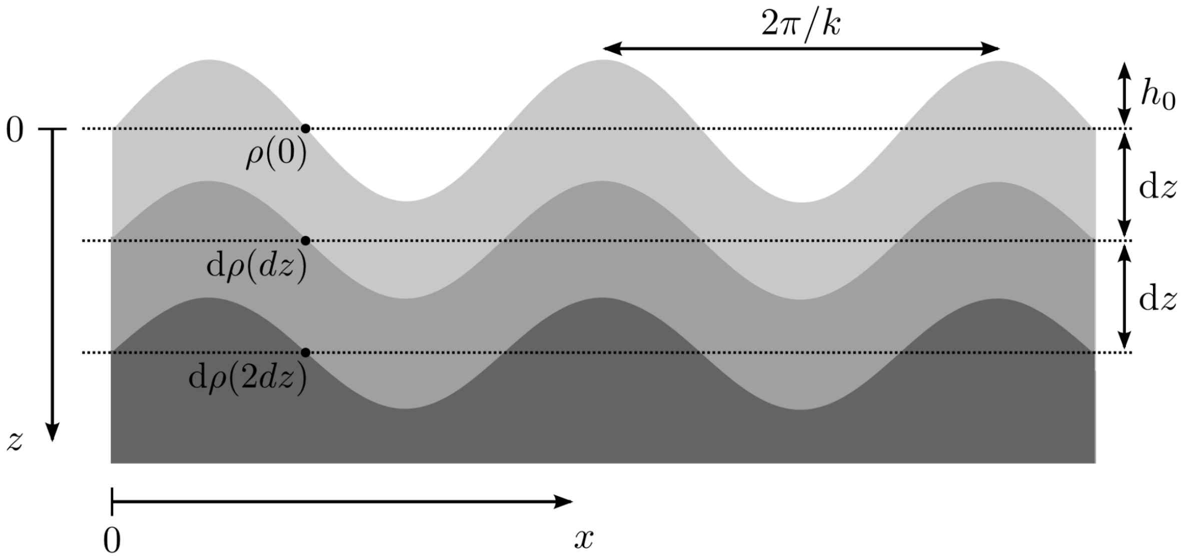

Figure 2.4: The first three layer interfaces of a vertically layered crust with density distribution $\rho(z)$ and surface topography $h(x)$ for a given wavelength $2\pi/k$. Each layer has a constant density and each interface has a density contrast $d\rho = \frac{\partial\rho}{\partial z}\mathrm{d}z$, where $\mathrm{d}z$ is the infinitesimal distance between consecutive layers (Besserer et al., 2014).

In this work, only shallow depths (i.e. high degrees) are considered, even though density anomalies extend down to the mantle (Besserer et al., 2014). Low degrees are not treated because of the influence of flexure. Wieczorek et al. (2013) determined that $l > 170$ is sufficient to neglect flexural signals. The main constraint for the upper degree limit is the correlation between the gravity and topography, especially for the localised spectra, as was discussed in the manuscript. The assumed in-phase nature of the density layers in Figure 2.4 is a reasonable assumption since the correlation between observed gravity and topography-induced gravity is close to unity.

Still the lunar crust-mantle boundary density contrasts contributes to the observed gravity, and thus might influence the (slope of the) effective density spectrum. Similarly, sharp transitions in density with depth, such as the basalt-crust interface in the lunar maria, may also effect that spectrum. An investigation in the effect of these density contrasts is achieved using an admittance approach.

Consider two sinusoidal interfaces, for example, the lunar surface and crust-mantle interface. These interfaces are vertically separated by a mean distance denoted as $z_{\text{upper}}$, and have a phase offset $\varphi$. The upper interface is characterised by its density contrast $\rho_{\text{upper}}$ and topographic amplitude $h_0$. Similarly, the lower interface is characterised in the same manner by $\Delta\rho_{\text{lower}}$ and $h_1$ (Besserer et al., 2014). The free-air gravity anomalies due to the upper ($\Delta g_{\text{upper}}$) and lower ($\Delta g_{\text{lower}}$) interfaces are

$$\Delta g_{\text{upper}} = 2\pi G \rho_{\text{upper}} h_0 \cos kx, \tag{2.1}$$

and

$$\Delta g_{\text{lower}} = 2\pi G \Delta\rho_{\text{lower}} h_1 \exp\left(-k z_{\text{upper}}\right) \cos\left(kx + \varphi\right), \tag{2.2}$$

where $k$ is the wavenumber, $x$ an arbitrary lateral coordinate, and $G$ the gravitational constant. The admittance of the net surface gravity $\Delta g = \Delta g_{\text{upper}} + \Delta g_{\text{lower}}$ to the surface topography $h$ is calculated as

$$Z(k) = \frac{\overline{\mathrm{h}(k)\Delta\mathrm{g}(k)}}{\overline{\mathrm{h}^2(k)}}, \tag{2.3}$$

where $\mathrm{h}(k)$ and $\Delta\mathrm{g}(k)$ are the Fourier components of $h(k)$ and $\Delta g(k)$, respectively, and the overlines represent an average over $k$ (Audet, 2014).

Assuming $h_0$ and $h_1$ are independent of $\varphi$ and of each other, and $\varphi$ is independent of $k$ (Audet, 2014), Equation 2.3 becomes

$$Z = 2\pi G \left( \rho_{\text{upper}} + \frac{h_1}{h_0} \Delta\rho_{\text{lower}} \exp\left(-k z_{\text{upper}}\right) \cos\varphi \right). \tag{2.4}$$

At short wavelengths the lunar surface topography, mainly caused by meteoroid impacts, is not expected to be correlated with the crust-mantle topography. Furthermore, other processes in the mantle affect the crust-mantle topography and not surface topography at high degrees, such as mantle convection (Wieczorek et al., 2013). Therefore it can be reasonably assumed that the phase offset between the surface topography and crust-mantle topography is a random variable uncorrelated with $k$ (Audet, 2014). This means that the ensemble average of Equation 2.4 over $\varphi$ results in an admittance expression independent of the crust-mantle crust-mantle topography and density contrasts. Since effective density is a normalised admittance approach, the effective density will be unbiased by the crust-mantle interface.

## 2.3. Localisation Robustness Analysis

In order to determine the influence of the input parameters to the resulting surface density and density gradient maps, various combinations for $\theta_{\text{cap}}$, $l_{\text{win}}$, and $r$ are provided as input to the localisation code. The chosen value for the bandwidth $l_{\text{win}}$ depends on the cap radius $\theta_{\text{cap}}$, such that 30 best spherical caps are created for each latitude and longitude rotation point. The meaning of 'best' in this context is a spherical cap whose power is >99% concentrated within its area (Wieczorek and Simons, 2007).

The linear surface density and linear density gradient for various combinations of $r$ (1-10°) and $\theta_{\text{cap}}$ (2.5-30°) are presented in Figure 2.5 and Figure 2.6, respectively.

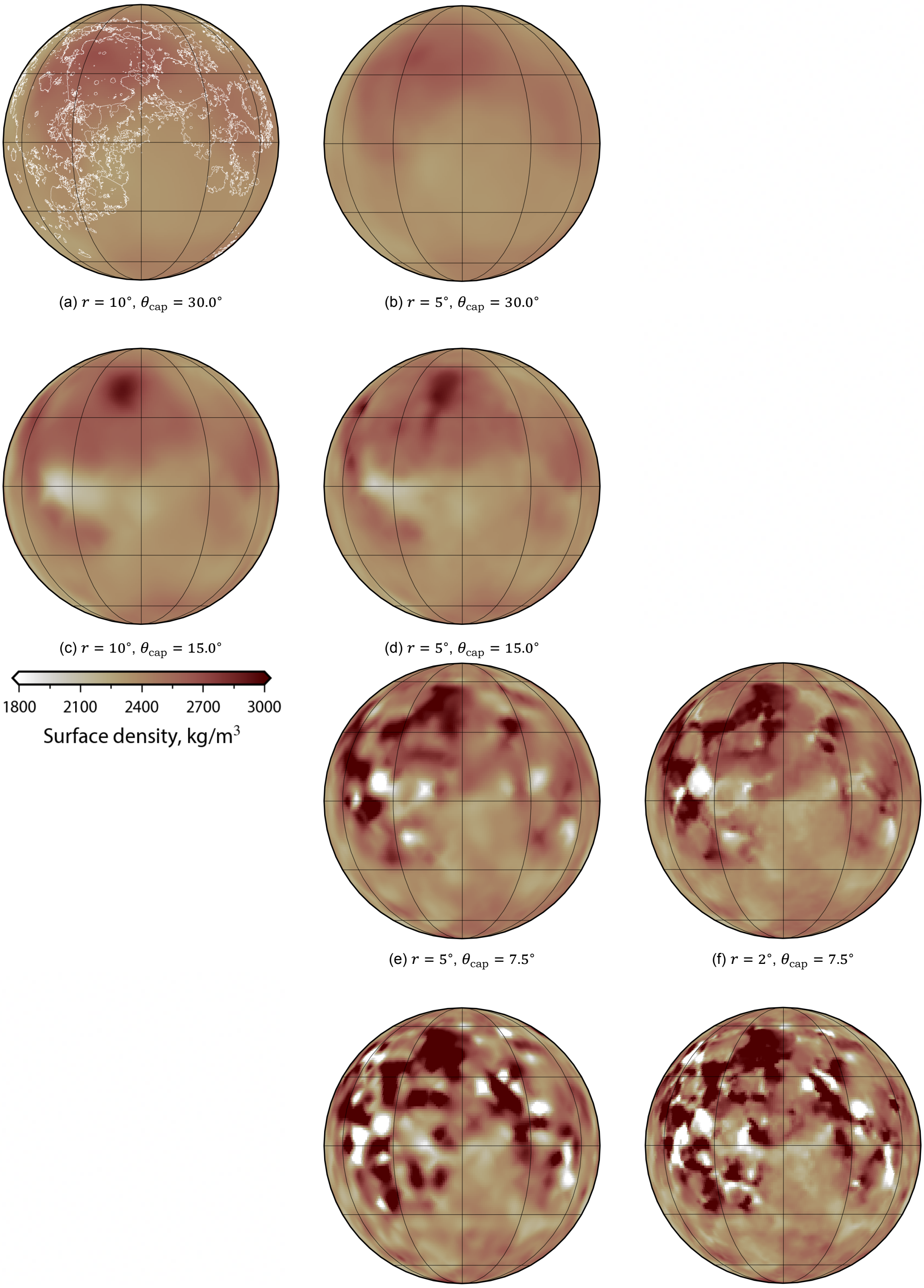

(a) $r = 10°$, $\theta_{\text{cap}} = 30.0°$

(b) $r = 5°$, $\theta_{\text{cap}} = 30.0°$

(c) $r = 10°$, $\theta_{\text{cap}} = 15.0°$

(d) $r = 5°$, $\theta_{\text{cap}} = 15.0°$

(e) $r = 5°$, $\theta_{\text{cap}} = 7.5°$

(f) $r = 2°$, $\theta_{\text{cap}} = 7.5°$

(g) $r = 5°$, $\theta_{\text{cap}} = 5.0°$

(h) $r = 2°$, $\theta_{\text{cap}} = 5.0°$

Figure 2.5: Nearside linear surface density estimates of the Moon. Lateral variations determined by a multitaper approach where 30 spherical caps are 99% concentrated each $r$ degrees in latitude and longitude, with various cap radii $\theta_{\text{cap}}$ indicated in the subcaptions. Maps are presented in an orthographic projection centered on 0° longitude. Boundaries of the lunar maria are indicated in (a) by a solid white line.

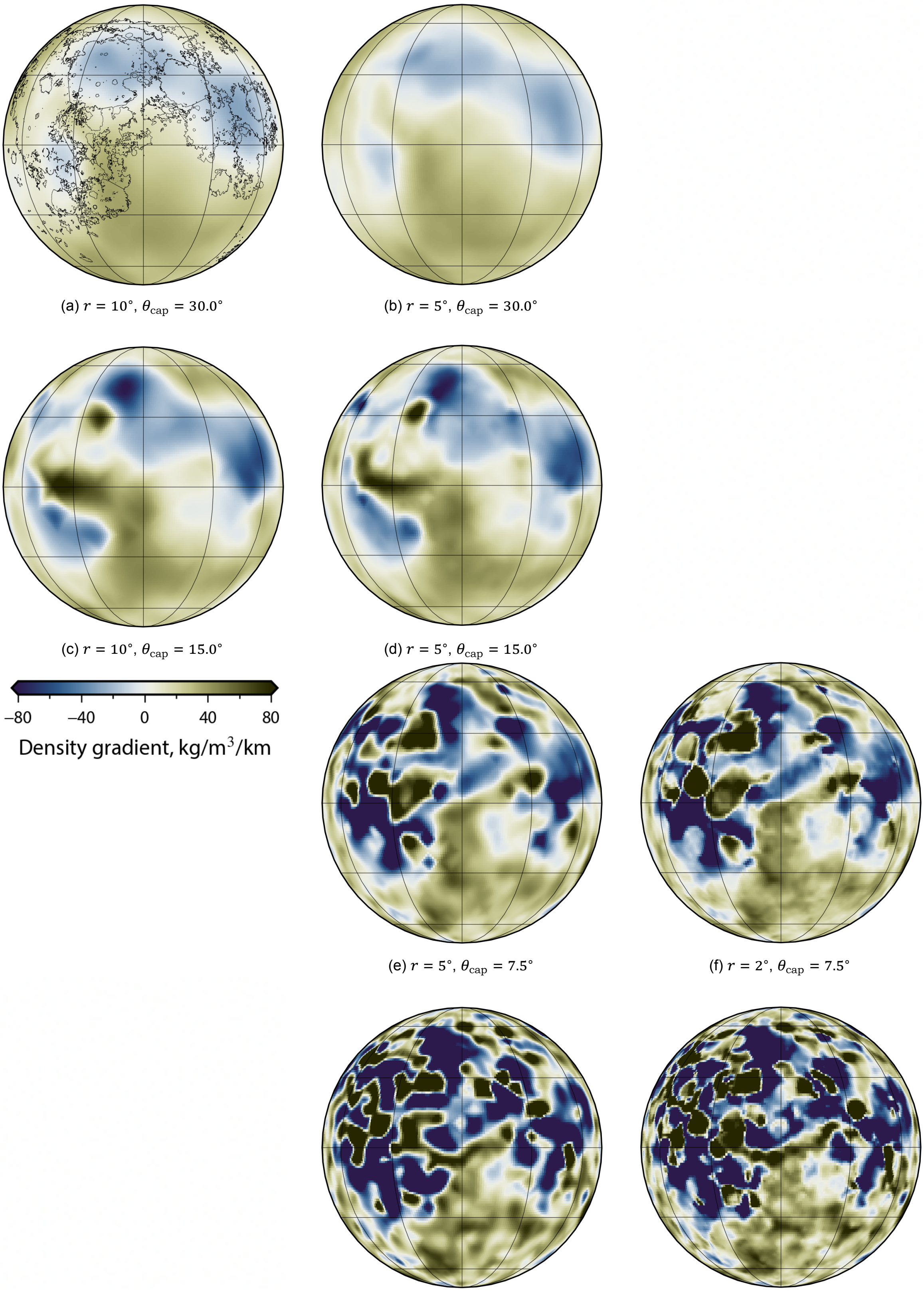

(a) $r = 10°$, $\theta_{\text{cap}} = 30.0°$

(b) $r = 5°$, $\theta_{\text{cap}} = 30.0°$

(c) $r = 10°$, $\theta_{\text{cap}} = 15.0°$

(d) $r = 5°$, $\theta_{\text{cap}} = 15.0°$

(e) $r = 5°$, $\theta_{\text{cap}} = 7.5°$

(f) $r = 2°$, $\theta_{\text{cap}} = 7.5°$

(g) $r = 5°$, $\theta_{\text{cap}} = 5.0°$

(h) $r = 2°$, $\theta_{\text{cap}} = 5.0°$

Figure 2.6: Nearside linear density gradient estimates of the Moon. Lateral variations determined by a multitaper approach where 30 spherical caps are 99% concentrated each $r$ degrees in latitude and longitude, with various cap radii $\theta_{\text{cap}}$ indicated in the subcaptions. Maps are presented in an orthographic projection centered on 0° longitude. Boundaries of the lunar maria are indicated in (a) by a solid black line.

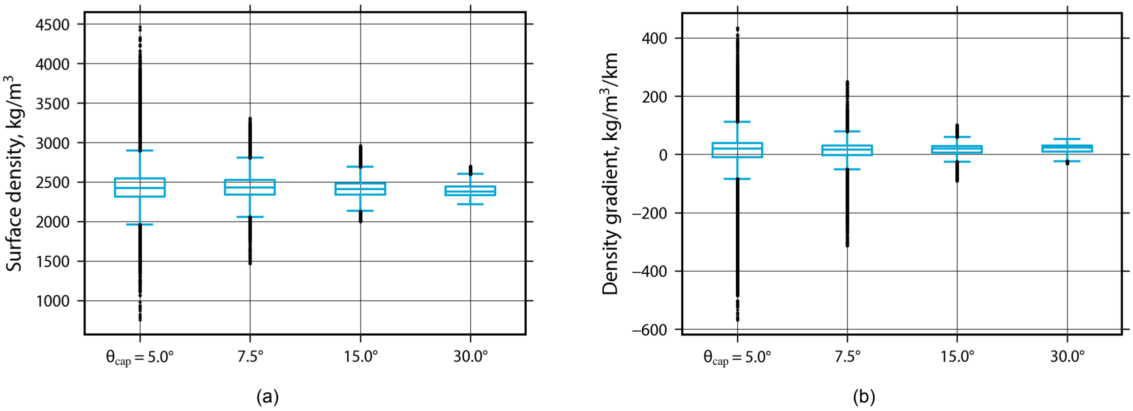

Figure 2.7: Boxplots of nearside linear surface density (a) and nearside linear density gradient (b) of the Moon, as a function of spherical cap radius $\theta_{\text{cap}}$. The central lines within the boxes are the median values, the boxes range from 25th to 75th percentiles, and the whiskers range from 5th to 95th percentiles. The outliers are shown as black dots.

First, it is observed from Figure 2.5 and Figure 2.6 that the resolution $r$ (different columns) exerts a smaller influence on the resulting maps than does the cap radius $\theta_{\text{cap}}$ (different rows). The maps with same $\theta_{\text{cap}}$ but different $r$ are nearly identical both in map features and values. However, maps with same $r$ but different $\theta_{\text{cap}}$ differ significantly from each other, especially in the lunar maria. Maps with large $\theta_{\text{cap}}$ (for example, 2.5b and 2.6b) are classified as smooth, small-varying surface density or density gradient values. On the contrary, maps with the same resolution but small $\theta_{\text{cap}}$ (for example, 2.5g and 2.6g) are seen to have small-scale features with extremely large variations in surface density and density gradient. This variability is especially true for the lunar maria, which are geologically more complex than the highlands (see Section 2.1), as was already observed in Oceanus Procellarum by Deutsch et al. (2019). Since a larger spherical cap effectively produces an average estimate of a larger area on the lunar surface, it is expected that larger $\theta_{\text{cap}}$ produce more smooth, small-varying feature maps, and vice-versa. Distributions of the surface density and density gradient as a function of $\theta_{\text{cap}}$ are presented in Figure 2.7, where it is observed that more extreme values are observed for smaller cap radii.

Second, all maps have distinct characteristics for the lunar maria and highlands. This commonality is already broadly introduced in the $\theta_{\text{cap}} = 30°$ maps; 2.5a shows high surface densities in the maria compared to the highlands, and 2.6a shows negative density gradients in the maria and positive density gradients in the highlands. With decreasing $r$ and $\theta_{\text{cap}}$ the same observation holds, albeit with additional smaller-scale variations and more extreme values, as has been discussed in the previous point. Negative density gradients prohibit the use of the exponential compaction model.

Third, the lunar highlands are very robust for various $r$ and $\theta_{\text{cap}}$, whereas the maria are heavily influenced by these model parameters. A partial explanation is that the maria are geological complex, as was already discussed in the first point. However, it is thought that the linear model introduced in the manuscript is not suitable for the lunar maria. More specifically, the lunar maria are large impact basins filled by ancient volcanic eruptions (see Section 2.1), and it has been estimated that these impact basins have a low crustal thickness of 0-20 km (Wieczorek et al., 2013). In addition, high-density mantle material is dominantly present in the maria, giving rise to the 'mascons' in the free-air anomaly (Figure 3.6), and may overly a lower-density (thin) crust as implied by negative density gradient values in Figure 2.6. Therefore, the two-layered mare compaction model introduced in the manuscript inside the lunar maria. The resulting surface density is a combination of the basalt density in the two-layered mare model and the linear surface density in the linear model.

## 2.4. Possibility of Inaccurate Albedo Correction for Latitude

As has been presented in the manuscript, the latitudinal dependency of $d$ is a result of latitude dependencies in $A$ and $P_{\text{max}}$. Unlike $P_{\text{max}}$, $A$ values may be inaccurately corrected for phase angle. Since incident sunlight at higher latitudes is more inclined from the local zenith than at lower latitudes, inaccurate correction of $A$ for multiple incident angles may be the cause for the latitudinal dependency of $A$, and ultimately of $d$. Jeong et al. (2015) ruled out this possibility by using LOLA 1.064 μm laser

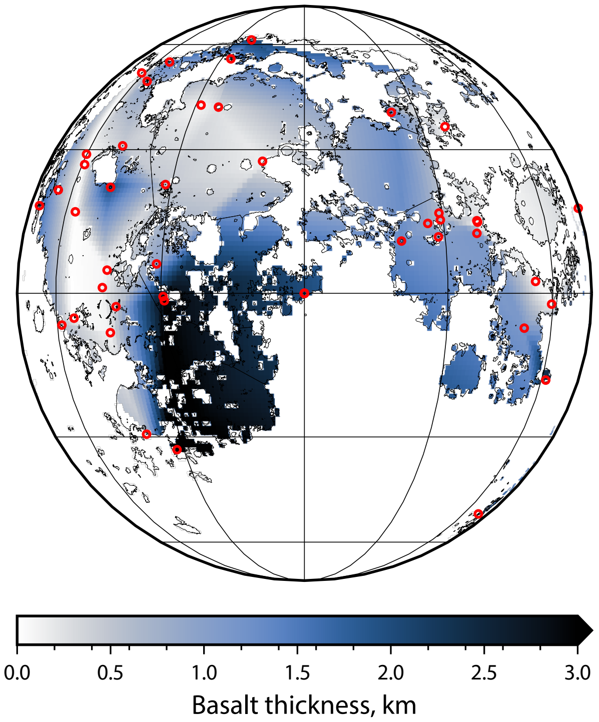

Figure 2.8: Basalt thickness estimates of the Moon by Du et al. (2019). Map is presented in an orthographic projection centered on 0° longitude. Boundaries of the lunar maria are indicated in by a solid black line, and basalt thickness estimates are indicated by a red dot.

reflectance measurements; as laser light is always reflected back to the instrument at 0° phase angle, phase angle correction is not needed. The albedo distribution of the LOLA laser measurements show the same latitudinal dependency, and thus confirm that phase angle correction does not cause the latitudinal dependency of the median grain size (Jeong et al., 2015).

## 2.5. Basalt Thickness Determination and Sensitivity Study

A parameter in the mare basalt model is the basalt thickness, which has not been included in the least squares fitting procedure to avoid ambiguity in the results. This is because the basalt density is already included in the fitting procedure, which is largely dependent on the basalt thickness. For example, if the basalt is thicker, the same gravity signal can be explained by a lower basalt density, and vice-versa. Since the parameter of interest is the basalt density, the basalt thickness should be retrieved from an independent source.

It has been chosen to take basalt thickness estimated from high-resolution topography by Du et al. (2019). More specifically, this study numerically models the elevation, flooding, and degradation of impact craters. The basalt thickness estimate is then obtained by taking the difference between the modelled crater depth and the observed crater depth, because the mare are impact basins filled by ancient volcanic eruptions (see Section 2.1). These discrete estimates are then translated to a map by linear interpolation within the mare bounds, as presented by Figure 2.8. It should be mentioned that more complex methods, such as elevation flow models, have been considered to obtain a basalt thickness map. However, it has been chosen to carry out a more simple linear interpolation and see the effect on the density results in the maria.

As a sensitivity study of basalt thickness, two additional maps have been provided as input to the mare basalt model. Namely, the entire map in Figure 2.8 has been multiplied by 75% and 125%, and the subsequent results are presented in Figure 2.9.

It can be seen that in 2.9a the surface density estimates in the maria are more extreme than estimates in 2.9b. Especially given the grain density estimates (see manuscript), the estimates in 2.9b result in more realistic porosity estimates. This could mean that the basalt thickness map in Figure 2.8 is inaccurate, particularly, the estimates of basalt thickness are too thin. If a basalt is too thin, the basalt

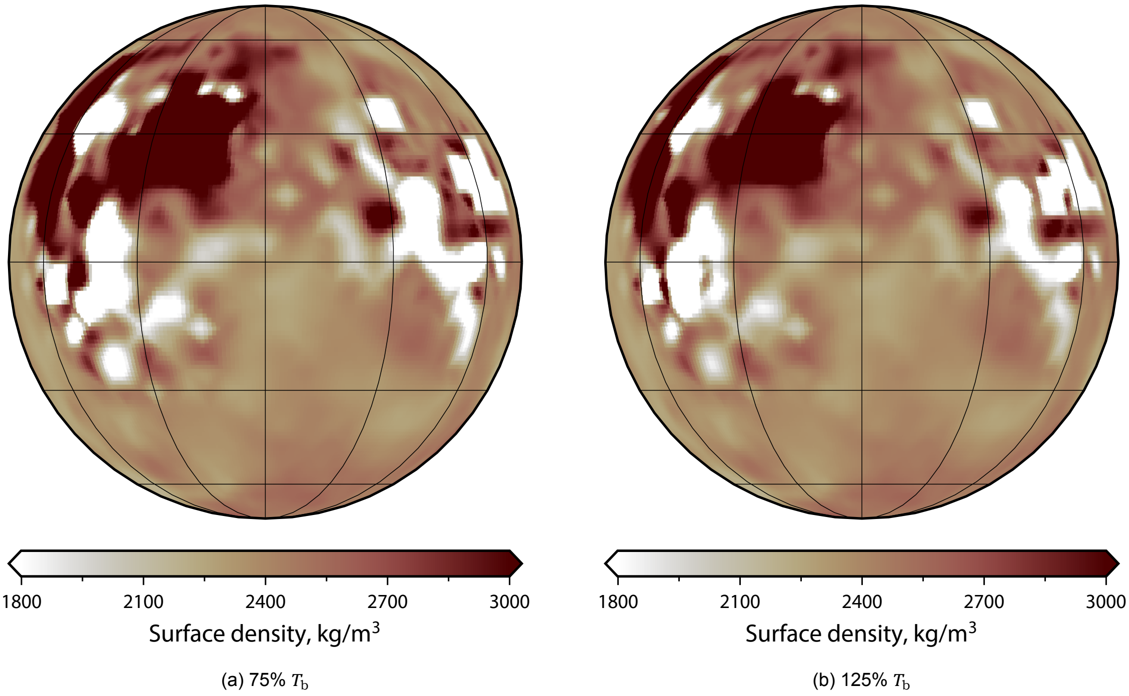

(a) 75% $T_{\text{b}}$

(b) 125% $T_{\text{b}}$

Figure 2.9: Nearside linear surface density estimates of the Moon for (a) 75% basalt thickness, and (b) 125% basalt thickness. Lateral variations determined by a multitaper approach where 30 spherical caps are 99% concentrated each 5 degrees in latitude and longitude, with cap radius $\theta_{\text{cap}} = 10^{\circ}$. Maps are presented in an orthographic projection centered on 0° longitude.

density is compensated to account for the same gravity signal, resulting in too high density estimates and therefore negative porosity. This should not necessarily be true everywhere. For example, it can be seen by comparing 2.9a and b that low density estimates increase as basalt thickness increases. The previous argument therefore does not hold anymore, and this could relate to inaccurate crustal density structure under the basalt. If the basalt becomes thicker, and if the crustal density is assumed too high, a thicker basalt density could result in a higher basalt density estimate.

Thus, it appears that a portion of the basalt thickness map is inaccurate to model the basalt gravity signals in the mare, and an increase in the basalt thickness result generally result in more realistic density and porosity estimates. In Chapter 3 this discussion is re-stated together with the basalt model discussion in the manuscript.

# 3

# Conclusion

This research aimed to characterise the lunar regolith in terms of its compactness by combining gravity and light polarisation observations. Based on a correlation study between the Moon's gravity field and reflected surface sunlight, it can be concluded that combining these complementary information sources improves estimates of regional variations in lunar regolith compactness. The constrained density structure of the Moon's crust resulted in highland surface densities of $2397 \pm 63$ kg/m$^3$ and mare surface densities averaging at $2736 \pm 487$ kg/m$^3$. Highland estimates are slightly larger ($+3.1$ %) than previously determined, while mare estimates are slightly lower ($-3.8$ %), albeit a large uncertainty that can be attributed to the geologically complex nature of the maria. Corresponding highland porosities of $18.8 \pm 2\%$ are consistent with those of lunar soil samples (averaging about 20%), while porosity values in the mare areas remain uncertain.

Regional variations in density have been determined by a localised spectral approach of the Moon's global gravity field, which could be translated to porosity via grain density. While localisation is a promising technique for geological homogeneous areas such as the lunar highlands, it raises the question of whether it is accurate for more geological complex areas such as the lunar maria. In addition, regional variations at smaller scales require gravity models of even higher resolution than current models.

Furthermore, the median grain size of lunar regolith has been estimated by analysis of reflected surface sunlight. Since these polarimetric observations are taken by Earth-based telescopes, this method is limited to the lunar nearside because the Moon is in tidal-lock with Earth. It has been observed that median grain size is larger in the maria than in the highlands, probably because the difference in composition results in an increased sensitivity to comminution in the highlands compared to the maria due to continuous bombardment of weathering agents on the Moon's surface.

Next, since high correlations between albedo, porosity, and grain size have been found in laboratory photometry of regolith analogues, these have been re-evaluated for the lunar nearside by a triangular correlation study between gravimetry-derived porosity, polarimetry-derived grain size, and albedo. It has been found that the scattering properties of lunar regolith are very similar to those of regolith analogues on Earth, which has resulted in extra constraints on the density and porosity structure of the Moon's upper crust. While this approach had promising results, it remains an indirect method for a combined study of lunar regolith. A direct correlation study is expected to be more effective, but polarimetry observations that match the gravity spatial resolution are currently scarce.

Based on these conclusions, future studies could address; 1) gravity modelling of the lunar mare basalts, 2) reiteration of this study for the lunar farside, and 3) Direct polarimetry-derived porosity constraints. It is believed that these three subjects advance gravity analysis of the Moon and naturally extend the research objective of this study. These recommendations are elaborated upon below.

1. Gravity modelling of the lunar mare basalts. Models of the vertical and lateral density profiles within the lunar maria have proven to be quite unstable because the maria are geologically complex. Additionally, the majority of the resulting density estimates are unrealistic as corresponding porosities are either negative or not in accordance with lunar mare soil samples. Therefore, it is recommended that the lunar maria are carefully re-examined. Specifically, the mare basalt model by Gong et al. (2016) employed in these regions models a high-density basalt overlying a

lower-density crust, and has four parameters; the basalt density, basalt thickness, upper crustal density, and crustal density gradient. The latter two have been constrained by assuming the crust is similar to highlands crust, however, this may not be true. It is believed the extreme density estimates are partially caused by this assumption. Furthermore, modelling the basalt thickness should receive extra attention. For example, by modelling basalt thicknesses from the lower degree ($l < 250$) spherical harmonics by Parker-Oldenburg inversion, or by accurately translating discrete thickness estimates to a spatial map by considering elevation flows. It is expected that this will result in more realistic density estimates within the maria.

2. Reiteration for the lunar farside. Hitherto, extra constraints on the density structure have been presented for the lunar nearside, primarily because lunar polarimetry has never been carried out from lunar orbit (Jeong et al., 2015). The observations used in this study are taken by Earth-based telescopes, which are not exposed to the lunar farside due to the synchronous rotation of the Moon around Earth (Srivastava and Varatharajan, 2016). However, the Wide-Angle Polarimetry Camera (PolCam) onboard Korea Pathfinder Lunar Orbiter (KPLO) is scheduled to launch in July 2022 and will measure the polarimetric properties of the lunar surface from orbit for the first time (Sim et al., 2020). These observations can extend this study by including farside observations, and since the farside is dominated by highlands (Petro and Pieters, 2004), this study is expected to work well for the farside. Besides, higher spherical harmonic degrees can be included in the highlands analysis since high correlations between gravity and topography have been found for these smaller scales, probably resulting in better density estimates (Goossens et al., 2020).
3. Direct polarimetry-derived porosity constraints. Building upon the previous point, polarimetry from lunar orbit will cover a large range of phase angles resulting in global high-resolution polarimetric phase curves of the Moon's surface. Photometric modelling of these curves allows for inversion of physical properties of lunar regolith such as porosity (Hapke, 2008). It has been demonstrated that Hapke's model can accurately infer porosity from these polarimetric phase curves (Hapke and Sato, 2015). These estimates of porosity can be translated to surface density through grain density (see manuscript), which can directly serve as surface constraints to the density structures resulting from the gravity field.

Nevertheless, the results indicate the potential for future gravity space missions to carry a polarimeter on board. The improved vertical and lateral density and porosity distribution determined in this research will enable future studies to decipher the (thermal) evolution of the Moon at smaller scales. This research has demonstrated similar behaviour of lunar regolith and synthetic regolith analogues on Earth, which could be utilised for future mission designs as humanity is returning to the Moon once and for all.

# A

# Linear Least Squares Fitting Procedure

Suppose measurements $\mathbf{y}$ can be expressed as a function of $\mathbf{x}$ as

$$\mathbf{y} = H\mathbf{x} + \boldsymbol{\epsilon}, \tag{A.1}$$

where $H$ is the observation matrix and $\boldsymbol{\epsilon}$ is the residuals vector. The objective of least-squares fitting is to minimise the squared residuals (Hansen et al., 2012):

$$\min J = \min \boldsymbol{\epsilon}^T\boldsymbol{\epsilon}, \tag{A.2}$$

such that the estimate $\hat{\mathbf{y}}$ can be calculated from the estimate parameters $\hat{\mathbf{x}}$

$$\hat{\mathbf{y}} = H\hat{\mathbf{x}} \tag{A.3}$$

Writing out the objective function Equation A.2 results in

$$\min\ (\mathbf{y} - H\mathbf{x})^T(\mathbf{y} - H\mathbf{x}) \tag{A.4}$$
$$\min\ \mathbf{y}^T(\mathbf{y} - H\mathbf{x}) - \mathbf{x}^T H^T(\mathbf{y} - H\mathbf{x}). \tag{A.5}$$

Thus, minimisation of the objective function translates to the latter term in Equation A.5 being equal to zero (Hansen et al., 2012), which results in

$$H^T(\mathbf{y} - H\hat{\mathbf{x}}) = 0 \tag{A.6}$$
$$H^T H\hat{\mathbf{x}} = H^T\mathbf{y} \tag{A.7}$$
$$\hat{\mathbf{x}} = (H^T H)^{-1}H^T\mathbf{y} \tag{A.8}$$

## A.1. Median Grain Size

Rewriting the empirical relationship between grain size and polarimetric anomaly (see manuscript) to the form of Equation A.1 results in

$$\log \mathbf{P}_{\max} = \frac{-\log \mathbf{A} + b}{a}, \tag{A.9}$$

and

$$\hat{\mathbf{y}} = -\hat{x}_1 \log \mathbf{A} + \hat{x}_2 = H\hat{\mathbf{x}}, \tag{A.10}$$

with

$$H = \begin{pmatrix} \log A_1 & 1 \\ \log A_2 & 1 \\ \vdots & \vdots \\ \log A_n & 1 \end{pmatrix} \tag{A.11}$$

Applying Equation A.8 to Equation A.10 results in

$$\hat{\mathbf{x}} = \begin{pmatrix} \hat{x}_1 \\ \hat{x}_2 \end{pmatrix} = \begin{pmatrix} 1/a \\ b/a \end{pmatrix} = (H^T H)^{-1} H^T \log \mathbf{P}_{\text{max}} \tag{A.12}$$

## A.2. Effective Density

### Linear model

Rewriting the theoretical linear effective density spectrum (see manuscript) to the form of Equation A.1 results in

$$\boldsymbol{\rho}_{\text{eff,lin}} = \frac{a}{\mathbf{k}} + \rho_{\text{surf,lin}}, \tag{A.13}$$

and

$$\hat{\mathbf{y}} = \frac{\hat{x}_1}{\mathbf{k}} + \hat{x}_2 = H\hat{\mathbf{x}}, \tag{A.14}$$

with

$$H = \begin{pmatrix} 1/k_1 & 1 \\ 1/k_2 & 1 \\ \vdots & \vdots \\ 1/k_n & 1 \end{pmatrix} \tag{A.15}$$

Applying Equation A.8 to Equation A.14 results in

$$\hat{\mathbf{x}} = \begin{pmatrix} \hat{x}_1 \\ \hat{x}_2 \end{pmatrix} = \begin{pmatrix} a \\ \rho_{\text{surf,lin}} \end{pmatrix} = (H^T H)^{-1} H^T \boldsymbol{\rho}_{\text{eff,lin}} \tag{A.16}$$

### Two-layered mare model

Rewriting the theoretical mare basalt effective density spectrum (see manuscript) to the form of Equation A.1 results in

$$\boldsymbol{\rho}_{\text{eff,mare}} = \rho_{\text{basalt}} + (\rho_0 - \rho_{\text{basalt}}) \left(\frac{r_0}{R}\right)^{\mathbf{1}+2} + \sum_{n=1}^{N} (\rho_n - \rho_{n-1}) \left(\frac{r_n}{R}\right)^{\mathbf{1}+2}, \tag{A.17}$$

and using

$$\sum_{n=1}^{N} (\rho_n - \rho_{n-1}) \left(\frac{r_n}{R}\right)^{\mathbf{1}+2} = \sum_{n=1}^{N} (\rho_0 + a(R - r_n) - \rho_0 - a(R - r_{n-1}) \left(\frac{r_n}{R}\right)^{\mathbf{1}+2} \tag{A.18}$$

$$= a \sum_{n=1}^{N} (r_{n-1} - r_n) \left(\frac{r_n}{R}\right)^{\mathbf{1}+2} \tag{A.19}$$

results in

$$\hat{\mathbf{y}} = \boldsymbol{\rho}_{\text{eff,mare}} - \rho_0 \left(\frac{r_0}{R}\right)^{\mathbf{l}+2} - a \sum_{n=1}^{N} (r_{n-1} - r_n) \left(\frac{r_n}{R}\right)^{\mathbf{l}+2} = \hat{x} \left(1 - \left(\frac{r_0}{R}\right)^{\mathbf{l}+2}\right) = H\hat{\mathbf{x}}, \tag{A.20}$$

with

$$H = \begin{pmatrix} 1 - \left(\frac{r_0}{R}\right)^{l_1+2} \\ 1 - \left(\frac{r_0}{R}\right)^{l_2+2} \\ \vdots \\ 1 - \left(\frac{r_0}{R}\right)^{l_n+2} \end{pmatrix} \tag{A.21}$$

Applying Equation A.8 to Equation A.20 results in

$$\hat{x} = \rho_{\text{basalt}} = (H^T H)^{-1} H^T \boldsymbol{\rho}_{\text{mare}} \tag{A.22}$$

# B

# Uncertainty Analysis

Use has been made of Hughes and Hase (2010) to propagate the uncertainties in the multi-variable equations.

The uncertainty in the median grain size estimate is expressed as

$$\begin{aligned} \delta d &= \delta(0.03 \exp(2.9(\log A + a \log P_{\max}))) && \text{(B.1)} \\ &= 0.03 \exp(2.9(\log A + a \log P_{\max}))\delta(2.9(\log A + a \log P_{\max})), && \text{(B.2)} \\ & && \text{(B.3)} \end{aligned}$$

where

$$\begin{aligned} \delta(2.9(\log A + a \log P_{\max})) &= 2.9\delta(\log A + a \log P_{\max}) && \text{(B.4)} \\ &= 2.9\sqrt{(\delta(\log A))^2 + (\delta(a \log P_{\max}))^2}, && \text{(B.5)} \end{aligned}$$

$$\delta(a \log P_{\max}) = a \log P_{\max} \sqrt{\left(\frac{\delta a}{a}\right)^2 + \left(\frac{\delta(\log P_{\max})}{\log P_{\max}}\right)^2}. \tag{B.6}$$

The uncertainties in measurements are $0.8\%A$ and $0.8\%P_{\max}$ (see section 4.3), and thus result in

$$\delta(\log A) = \frac{\delta A}{A \log 10} = \frac{0.8\%A}{A \log 10}, \tag{B.7}$$

and

$$\delta(\log P_{\max}) = \frac{\delta P_{\max}}{P_{\max} \log 10} = \frac{0.8\%P_{\max}}{P_{\max} \log 10}. \tag{B.8}$$

In addition to measurement uncertainties, there are uncertainties in the LLS fit, which can be calculated using

$$P_{\hat{x}} = (H^T P_y^{-1} H)^{-1} = \begin{pmatrix} \delta(\hat{x}_1)^2 & \delta(\hat{x}_1 \hat{x}_2) \\ \delta \hat{x}_2 \hat{x}_1 & (\delta x_2)^2 \end{pmatrix}. \tag{B.9}$$

The uncertainties in the fitting parameters $a$ and $b$ are then given as

$$\delta a = \delta\left(\frac{1}{\hat{x}_1}\right) = \hat{x}_1^2 \delta \hat{x}_1, \tag{B.10}$$

$$\delta b = \delta(a\hat{x}_2) = a\hat{x}_2 \left(\sqrt{\left(\frac{\delta a}{a}\right)^2 + \left(\frac{\delta \hat{x}_2}{\hat{x}_2}\right)^2}\right) \tag{B.11}$$

# C

# Supplementary Spatial Maps

In this section, high-resolution supplementary spatial maps are presented to provide the reader with additional insight into the observations.

## C.1. Free Air Anomaly

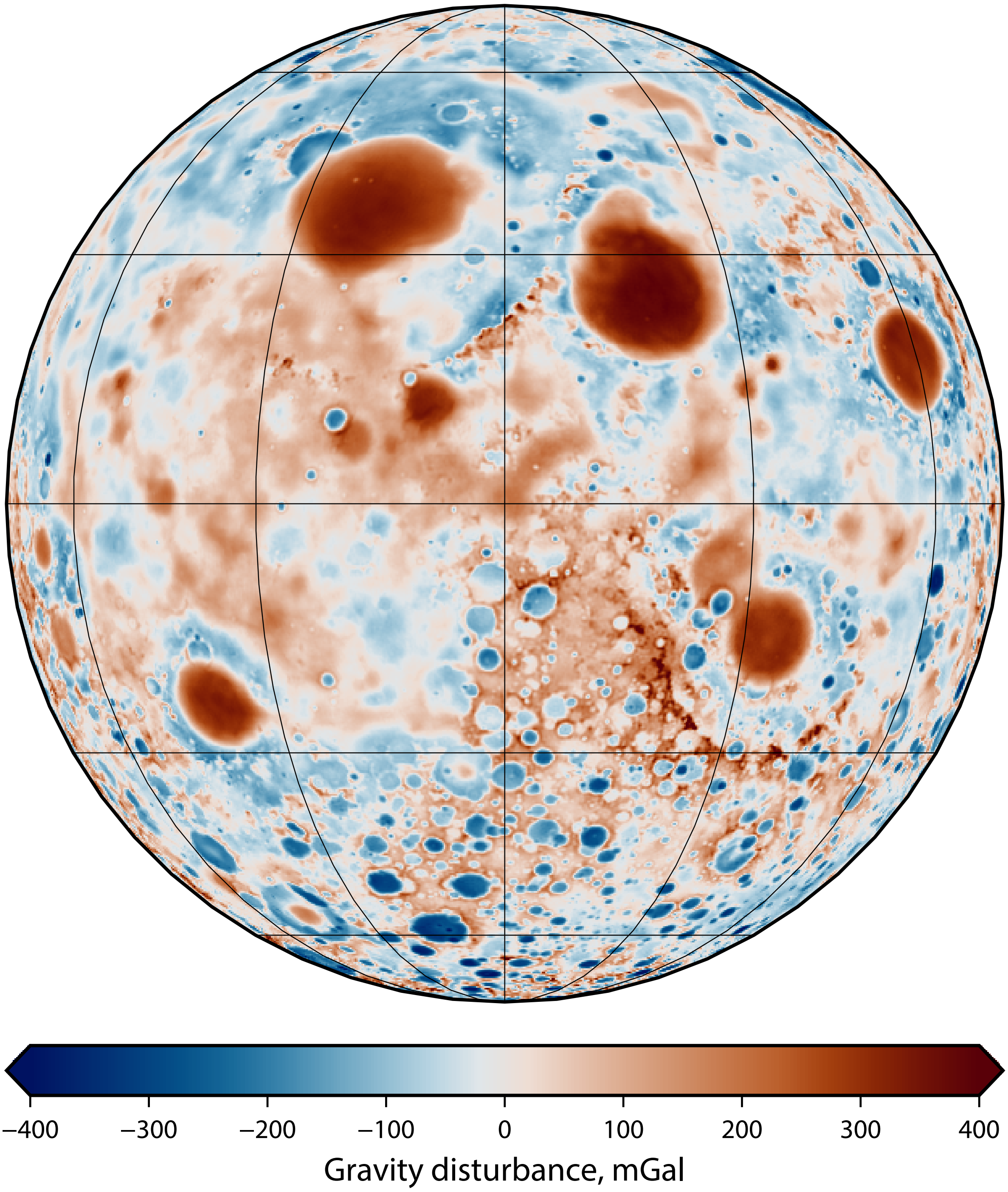
−400
−300
−200
−100
0
100
200
300
400
Gravity disturbance, mGal

Figure C.1: Nearside free air anomaly of the Moon for spherical harmonic degrees $1 \leq l \leq 650$. The map is presented in an orthographic projection centered on 0° longitude.

## C.2. Topography

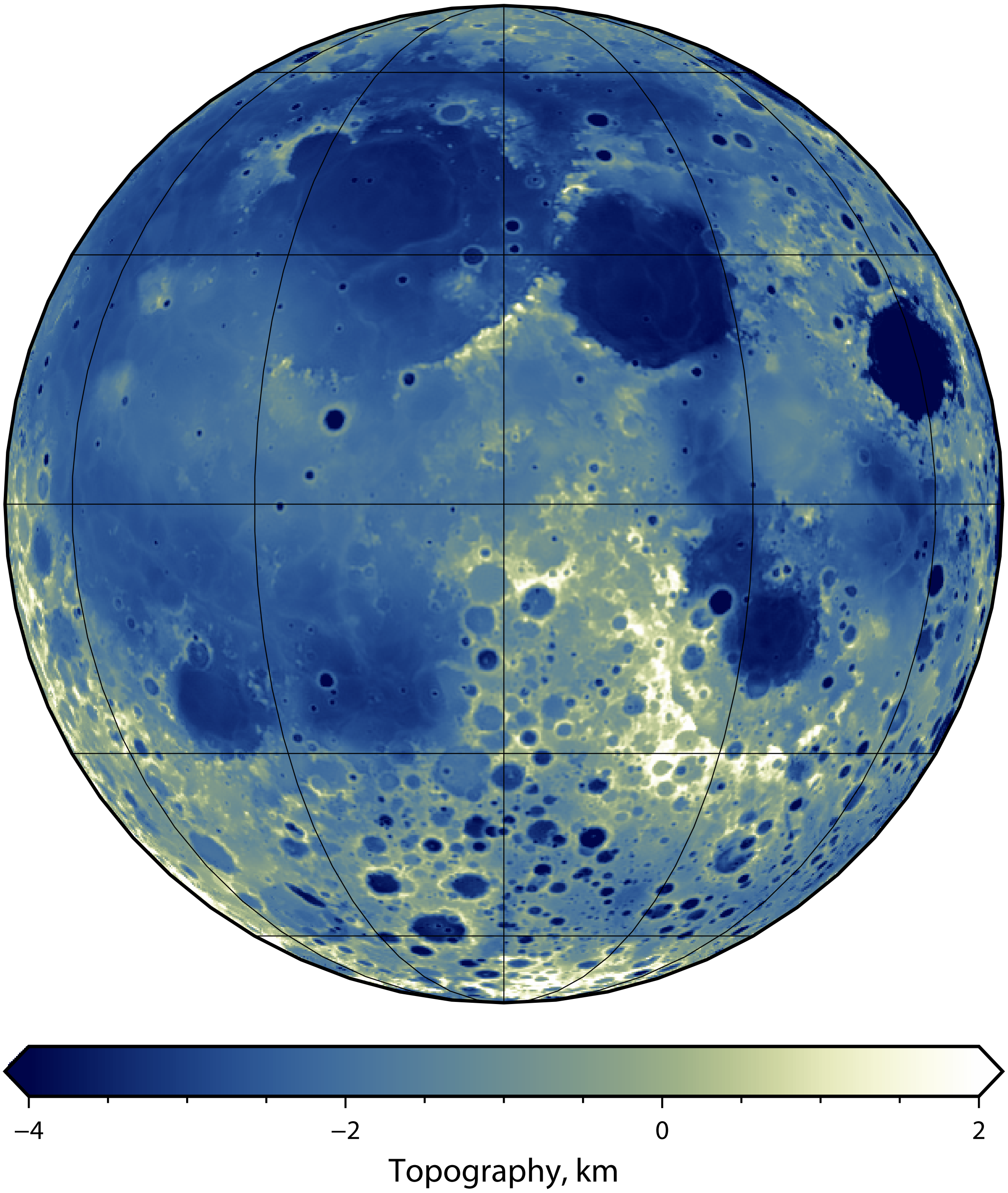

Figure C.2: Nearside topography of the Moon for spherical harmonic degrees $20 \leq l \leq 650$. The map is presented in an orthographic projection centered on 0° longitude.

## C.3. Bouguer Anomaly

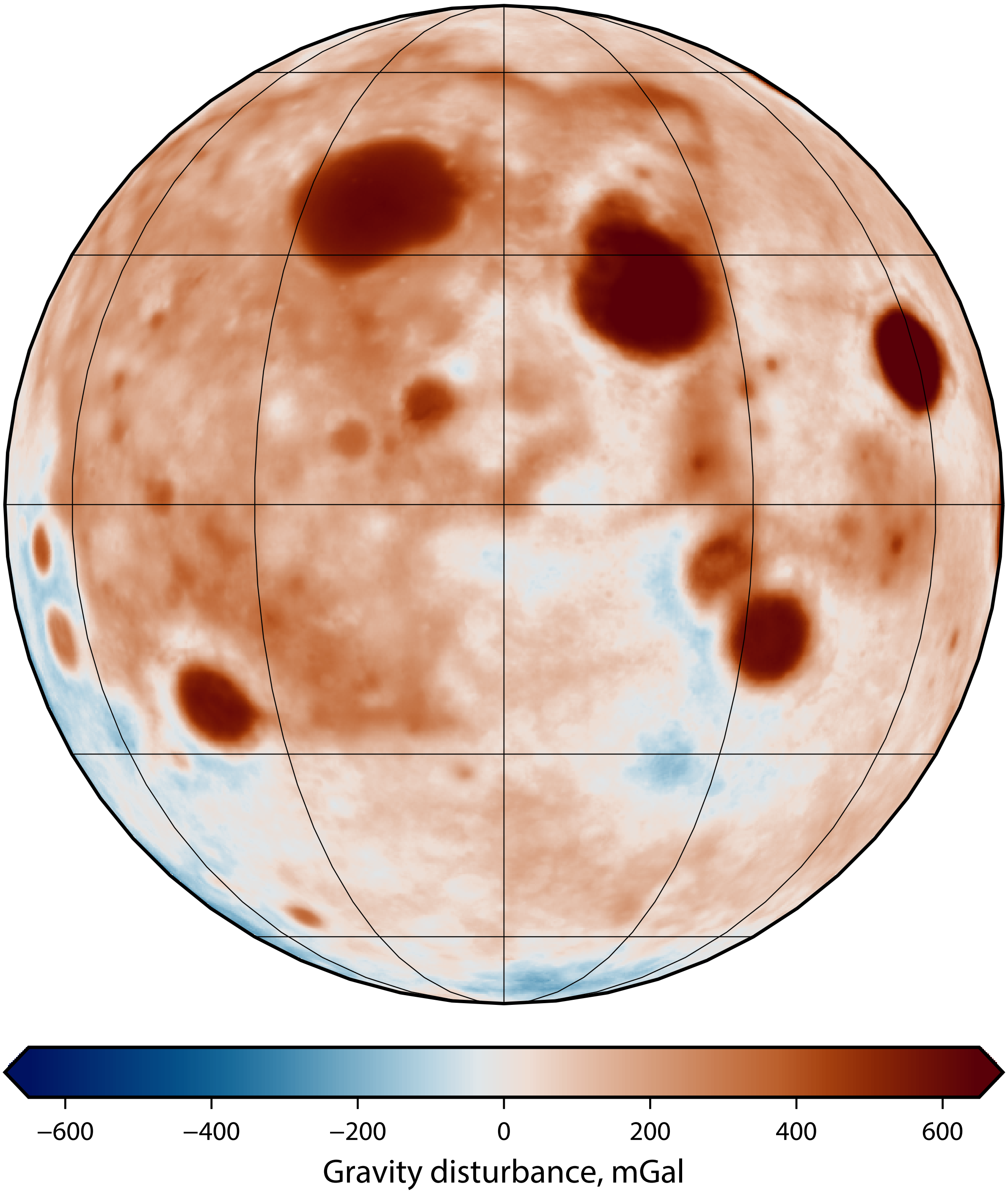
−600
−400
−200
0
200
400
600
Gravity disturbance, mGal

Figure C.3: Nearside Bouguer anomaly of the Moon for spherical harmonic degrees $1 \leq l \leq 650$. The map is presented in an orthographic projection centered on 0° longitude.

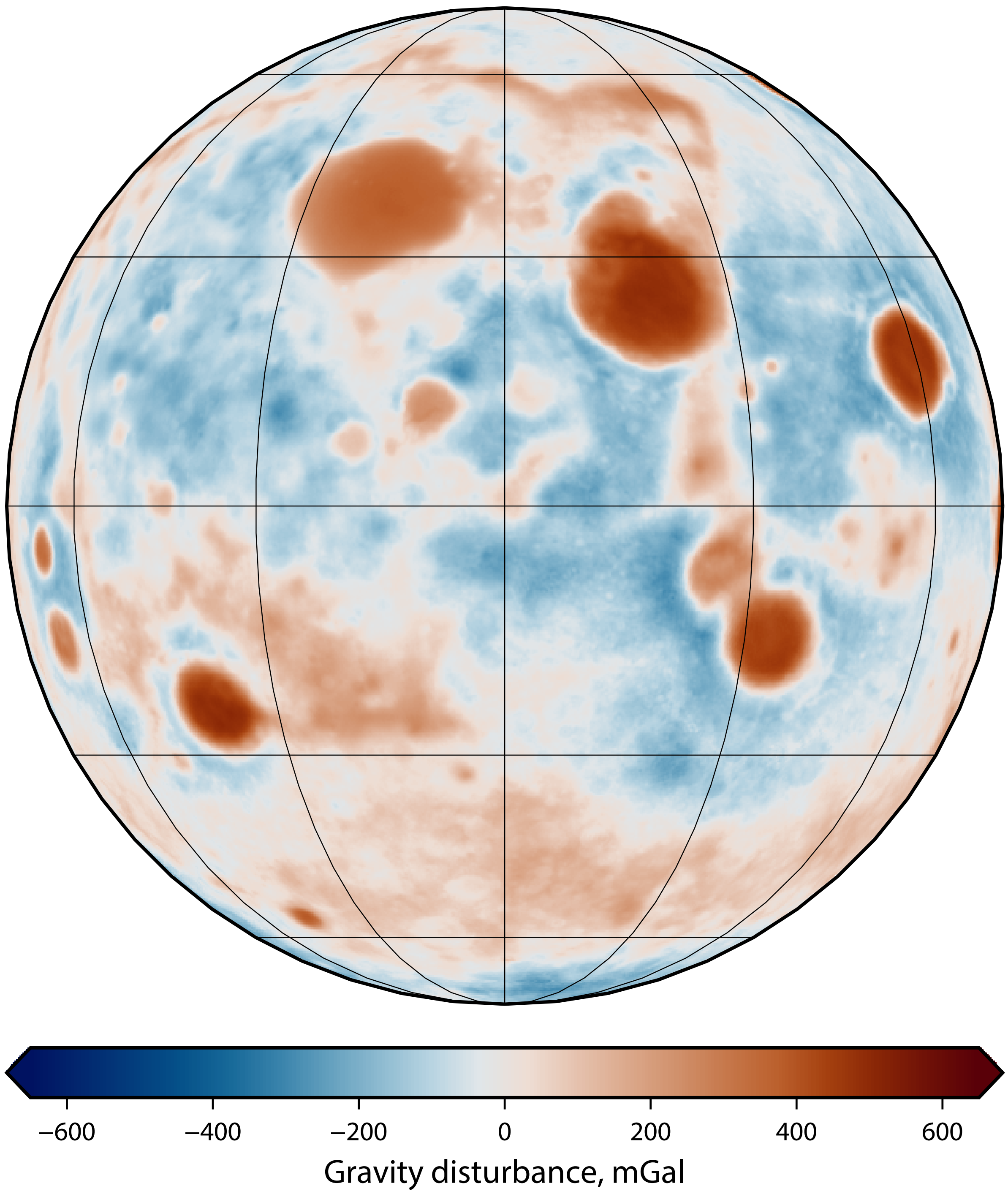
−600
−400
−200
0
200
400
600
Gravity disturbance, mGal

Figure C.4: Nearside Bouguer anomaly of the Moon for spherical harmonic degrees $3 \leq l \leq 650$. The map is presented in an orthographic projection centered on 0° longitude.

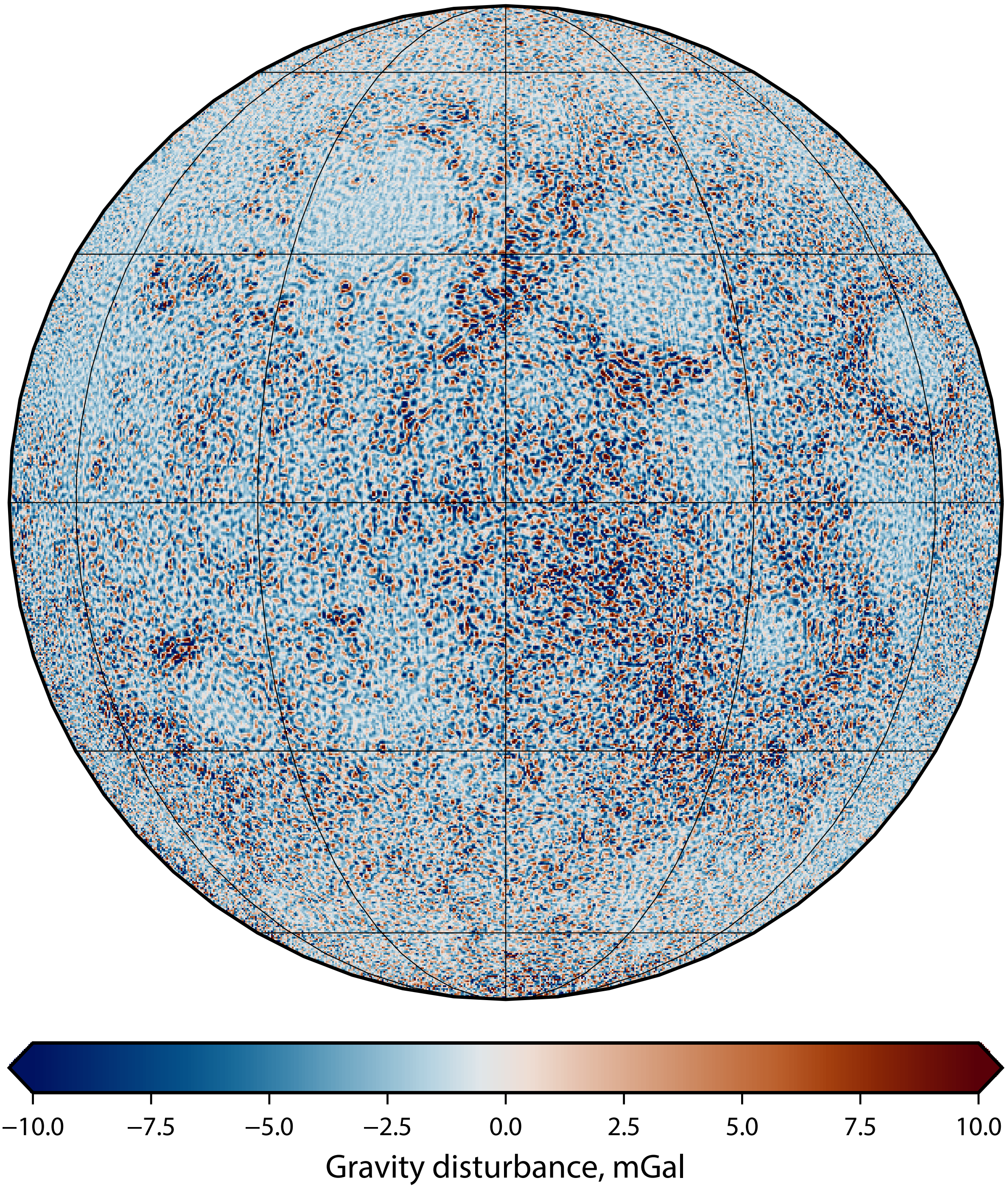
−10.0
−7.5
−5.0
−2.5
0.0
2.5
5.0
7.5
10.0
Gravity disturbance, mGal

Figure C.5: Nearside Bouguer anomaly of the Moon for spherical harmonic degrees $250 \leq l \leq 650$. The map is presented in an orthographic projection centered on 0° longitude.

# C.4. Gravity Gradient

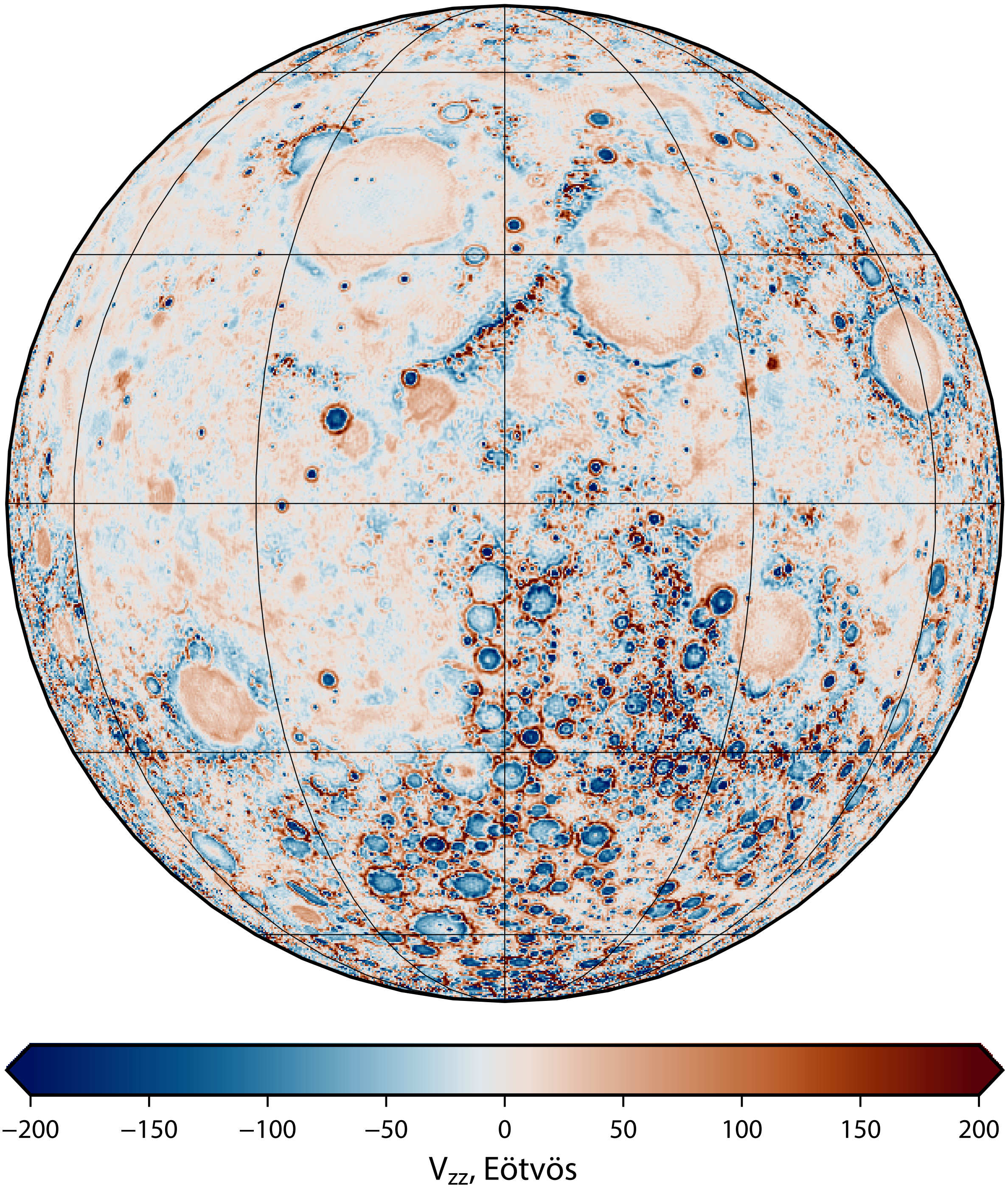
−200
−150
−100
−50
0
50
100
150
200
$V_{zz}$, Eötvös

Figure C.6: Nearside zz-component gravity gradient of the Moon for spherical harmonic degrees $20 \leq l \leq 650$. The map is presented in an orthographic projection centered on 0° longitude.

## C.5. Albedo

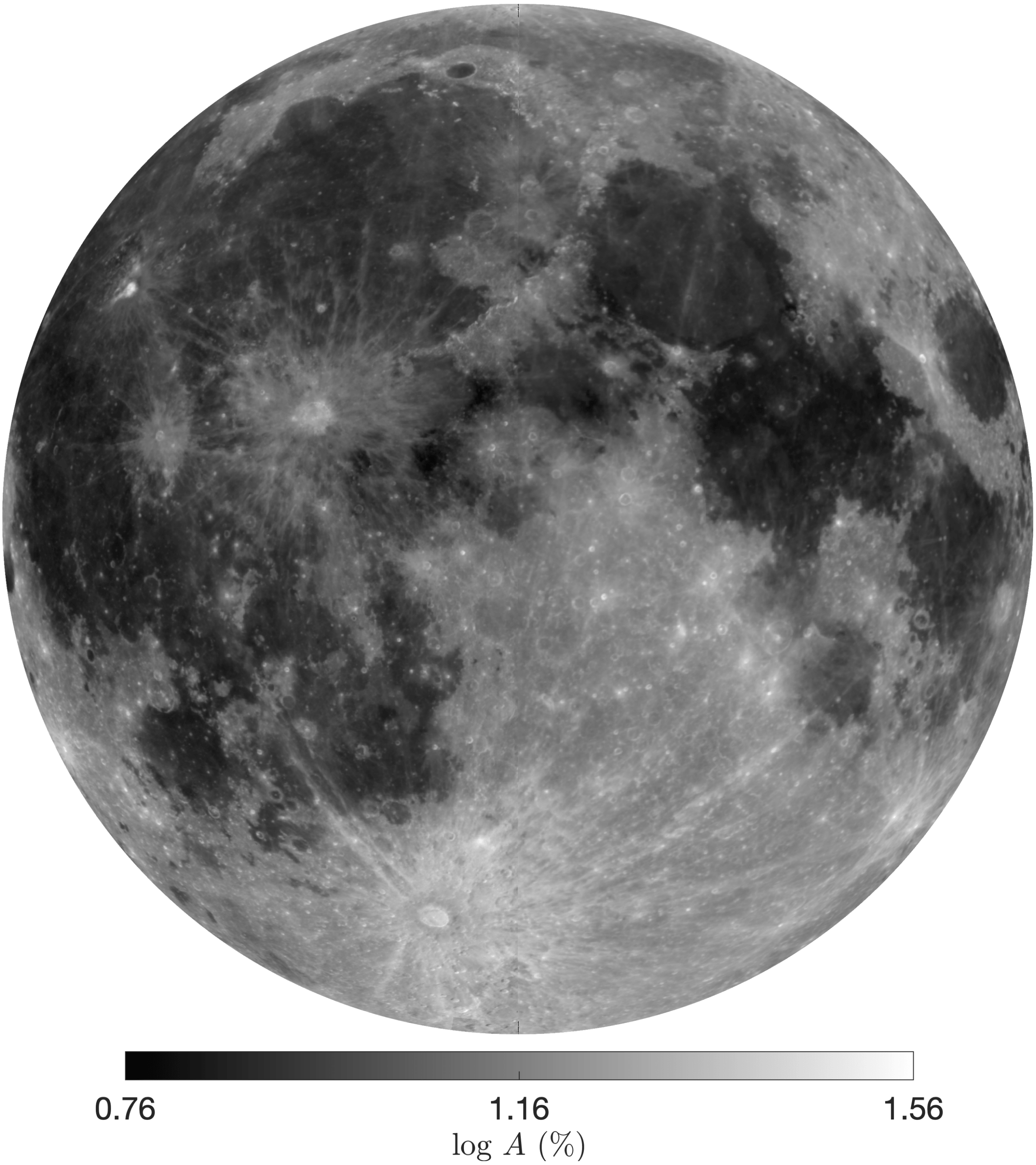

Figure C.7: Nearside albedo of the Moon. The map is presented in an orthographic projection centered on 0° longitude.

## C.6. Polarisation Degree

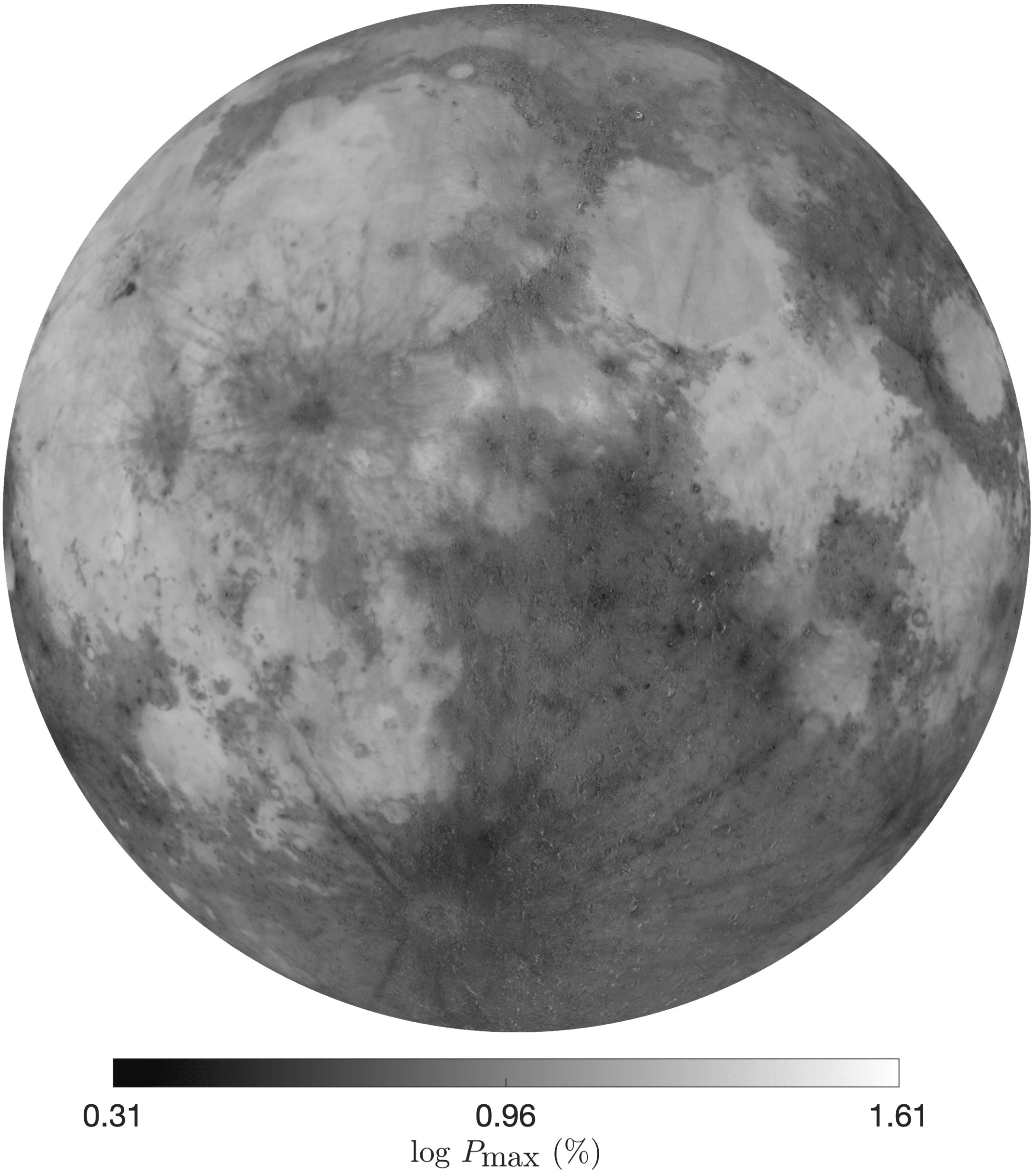

Figure C.8: Nearside maximum polarisation degree of the Moon. The map is presented in an orthographic projection centered on 0° longitude.

## C.7. Polarimetric Anomaly

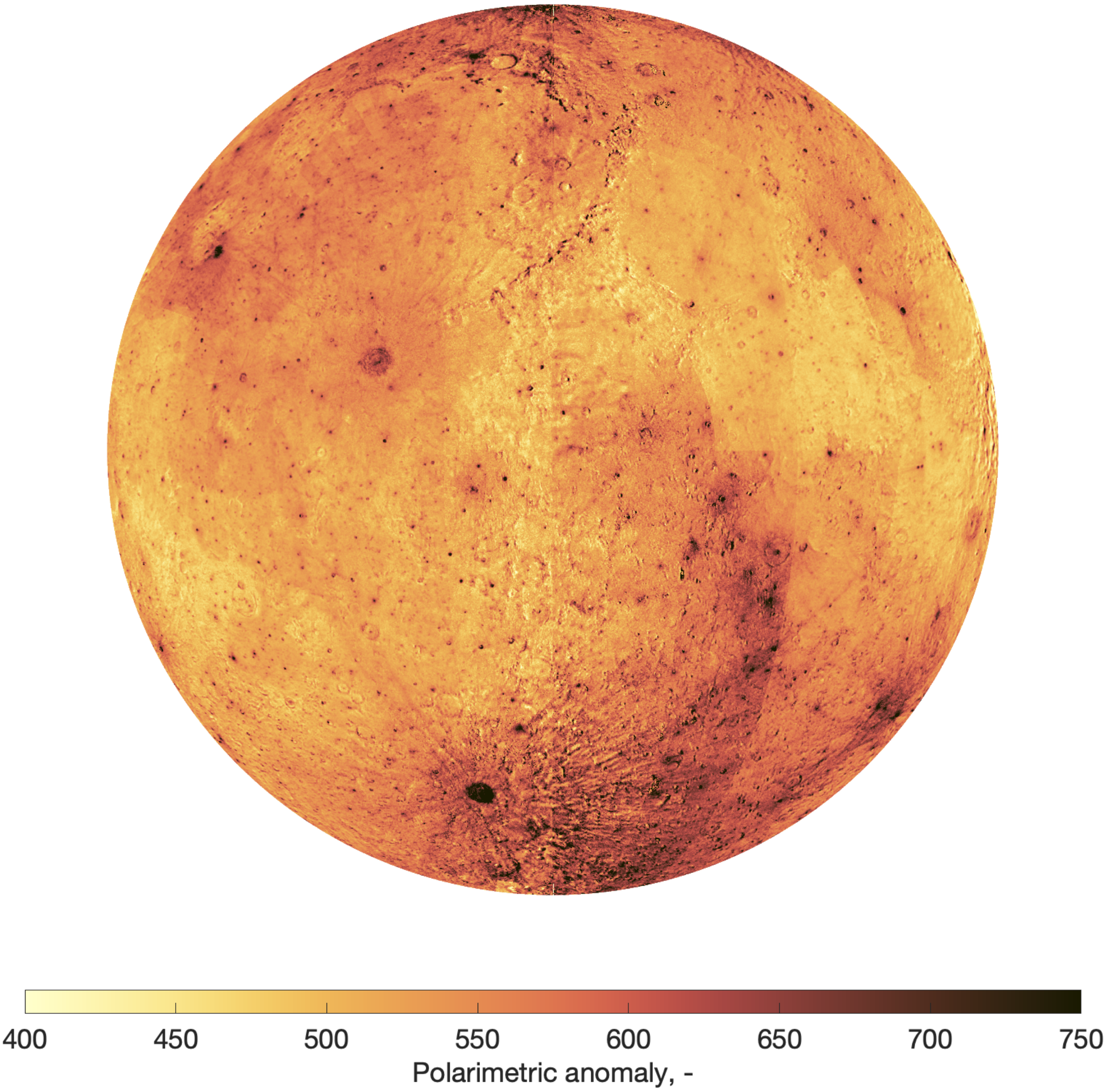
400
450
500
550
600
650
700
750
Polarimetric anomaly, -

Figure C.9: Nearside polarimetric anomaly of the Moon. The map is presented in an orthographic projection centered on 0° longitude.

# Bibliography

Adams, R. and Essex, C. (2016), *Calculus: A Complete Course*, Pearson Canada.

Aldrin, B. and Abraham, K. (2010), *Magnificent Desolation*, Bloomsbury Publishing Plc.

Audet, P. (2014), 'Toward mapping the effective elastic thickness of planetary lithospheres from a spherical wavelet analysis of gravity and topography', *Physics of the Earth and Planetary Interiors* **226**, 48–82.

Banderman, L., Kemp, L. and Wolstencroft, R. (1972), 'Circular Polarization of Light from Rough Surfaces', *Monthly Notices of the Royal Astronomical Society* **158**, 291–304.

Besserer, J., Nimmo, F., Wieczorek, M., Weber, R., Kiefer, W., McGovern, P., Andrews-Hanna, J., Smith, D. and Zuber, M. (2014), 'GRAIL gravity constraints on the vertical and lateral density structure of the lunar crust', *Geophysical Research Letters* **41**(16), 5771–5777.

Bowell, E. and Zellner, B. (1974), Polarizations of Asteroids and Satellites, Tucson: University of Arizona Press, pp. 381–404.

Deutsch, A., Neumann, G., Head, J. and Wilson, L. (2019), 'GRAIL-identified gravity anomalies in Oceanus Procellarum: Insight into subsurface impact and magmatic structures on the Moon', *Icarus* **331**, 192–208.

Dollfus, A. (1998), 'Lunar Surface Imaging Polarimetry: I. Roughness and Grain Size', *Icarus* **136**(1), 69 – 103.

Dollfus, A. and Bowell, E. (1971), 'Polarimetric Properties of the Lunar Surface and its Interpretation. Part I. Telescopic Observations', *Proceedings of the Second Lunar Science Conference* **10**, 29.

Du, J., Fa, W., Wieczorek, M., Xie, M., Cai, Y. and Zhu, M. (2019), 'Thickness of Lunar Mare Basalts: New Results Based on Modeling the Degradation of Partially Buried Craters', *Journal of Geophysical Research. Planets* **124**(9), 2430–2459.

Gong, S., Wieczorek, M., Nimmo, F., Kiefer, W., Head, J., Huang, C., Smith, D. and Zuber, M. (2016), 'Thicknesses of mare basalts on the Moon from gravity and topography', *Geophysical Research Letters* **121**, 854–870.

Goossens, S., Sabaka, T., Wieczorek, M., Neumann, G., Mazarico, E., Lemoine, F., Nicholas, J., Smith, D. and Zuber, M. (2020), 'High Resolution Gravity Field Models from GRAIL Data and Implications for Models of the Density Structure of the Moon's Crust', *Journal of Geophysical Research: Planets* **125**.

Griffiths, D. (2013), *Introduction to Electrodynamics; 4th ed.*, Pearson, Boston, MA. Re-published by Cambridge University Press in 2017.

Gualtieri, T. and Bandyopadhyay, A. (2015), 'Compressive deformation of porous lunar regolith', *Materials Letters* **143**, 276–278.

Hansen, C., Pereyra, V. and Scherer, G. (2012), *Least Squares Data Fitting With Application*, John Hopkins University Press.

Hapke, B. (2008), 'Bidirectional reflectance spectroscopy: 6. Effects of porosity', *Icarus* **195**(2), 918 – 926.

Hapke, B. and Sato, H. (2015), 'The porosity of the upper lunar regolith', *Icarus* **273**, 75 – 83.

Haynes, W. (2011), *Handbook of Chemistry and Physics*, 92 edn, CRC Press.

Hecht, E. and Zajac, A. (2013), *Optics*, 4 edn, Pearson Education Limited.

Hilst, R. v. d., Simons, F. and Zuber, M. (2002), *The Earth's Gravitational Field*, Massachusetts Institute of Technology.

Hinze, W., von Frese, R. and Saad, A. (2013), *Gravity Exploration*, Cambridge University Press.

Hughes, I. and Hase, T. (2010), *Measurements and Their Uncertainties: A Practical Guide to Modern Error Analysis*, Oxford University Press.

Ishiguro, M., Kuroda, D., Watanabe, M., Bach, Y., Kim, J., Lee, M., Sekiguchi, T., Naito, H., Ohtsuka, K., Hanayama, H., Hasegawa, S., Usui, F., Urakawa, S., Imai, M., Sato, M. and Kuramoto, K. (2017), 'Polarimetric Study of Near-Earth Asteroid (1566) Icarus', *The Astronomical Journal* **154**(5), 180.

Jansen, J., Andrews-Hanna, J., Li, Y., Lucey, P., Taylor, G., Goossens, S., Lemoine, F., Mazarico, E., Head, J., Milbury, C., Kiefer, W., Soderblom, J. and Zuber, M. (2017), 'Small-scale density variations in the lunar crust revealed by GRAIL', *Icarus* **291**, 107 – 123.

Jeong, M., Kim, S., Garrick-Bethell, I., Park, S., Sim, C. K., Jin, H., Min, K. W. and Choi, Y. (2015), 'Multi-band Polarimetry of the Lunar Surface. I. Global Properties', *The Astrophysical Journal Supplement Series* **221**(1), 16.

Kar, A., Sen, A. and Gupta, R. (2020), '"laboratory photometry of regolith analogues: Effect of porosity-ii"', *Icarus* p. 114211.

Karttunen, H. (2007), *Fundamental Astronomy*, 5 edn, Springer-Verlag Berlin and Heidelberg GmbH & Co. KG.

Konopliv, A., Asmar, S., Carranza, E., Sjogren, W. and Yuan, D. (2002), 'Recent Gravity Models as a Result of the Lunar Prospector Mission', *Icarus* **150**, 1–18.

Konopliv, A., Park, R., Yuan, D., Asmar, S., Watkins, M., Williams, J., Fahnestock, E., Kruizinga, G., Paik, M., Strekalov, D., Harvey, N., Smith, D. and Zuber, M. (2013), 'The JPL lunar gravity field to spherical harmonic degree 660 from the GRAIL Primary Mission', *Journal of Geophysical Research (Planets)* **118**, 1415–1434.

Konopliv, A., Park, R., Yuan, D., Asmar, S., Watkins, M., Williams, J., Fahnestock, E., Kruizinga, G., Paik, M., Strekalov, D., Harvey, N., Smith, D. and Zuber, M. (2014), 'High-resolution lunar gravity fields from the GRAIL Primary and Extended Missions', *Geophysical Research Letters* **41**.

Korokhin, V. and Velikodsky, Y. (2005), 'Parameters of the positive polarization maximum of the Moon: Mapping', *Solar System Research* **39**, 45–53.

Kvaratskhelia, O. I. (1988), 'Spectropolarimetry of the lunar surface and its ground samples.', *Bulletin of Abastumari Astrophysical Observatory* **64**, 1–312.

Landi Degl'Innocenti, E. and Bagnulo, S. and Fossati, L. (2007), 'Polarimetric Standardization', *The Future of Photometric, Spectrometric and Polarimetric Standardization Conference* **364**.

Lemoine, F., Goossens, S., Sabaka, T., Nicholas, J., Mazarico, E., Rowlands, D., Loomis, B., Chinn, D., Neumann, G., Smith, D. and Zuber, M. (2014), 'GRGM900C: A degree 900 lunar gravity model from GRAIL primary and extended mission data', *Geophysical Research Letters* **41**(10), 3382–3389.

Lissauer, J. and Pater, I. d. (2013), *Fundamental Planetary Science - Physics, Chemistry and Habitability*, Cambridge University Press.

Lyot, B. (1929), 'Recherches sur la Polarisation de la Lumière des Planètes et de quelques Substances Terrestres', *Annales de l'Observatoire de Paris, section de Meudon* **8**, 1–161.

McMaster, W. (1954), 'Polarization and the Stokes Parameters', *American Journal of Physics* **22**(6), 351–362.

Metzger, P. T., Anderson, S. and Colaprete, A. (2018), *Experiments Indicate Regolith is Looser in the Lunar Polar Regions Than at the Lunar Landing Sites*, pp. 79–85.

Moriarty III, D. P. and Pieters, C. M. (2018), 'The character of south pole-aitken basin: Patterns of surface and subsurface composition', *Journal of Geophysical Research: Planets* **123**(3), 729–747.

Namiki, N., Iwata, T., Matsumoto, K., Hanada, H., Noda, H., Goossens, S., Ogawa, M., Kawano, N., Asari, K., Tsuruta, S., Ishihara, Y., Liu, Q., Kikuchi, F., Ishikawa, T., Sasaki, S., Aoshima, C., Kurosawa, K., Sugita, S. and Takano, T. (2009), 'Farside Gravity Field of the Moon from Four-Way Doppler Measurements of SELENE (Kaguya)', *Science* **323**(5916), 900–905.

Nelson, D. M., Koeber, S. D., Daud, K., Robinson, M. S., Watters, T. R., Banks, M. E. and Williams, N. R. (2014), Mapping Lunar Maria Extents and Lobate Scarps Using LROC Image Products, *in* 'Lunar and Planetary Science Conference', p. 2861.

Neumann, G., Zuber, M., Wieczorek, M., Head, J., Baker, D. H., Solomon, S., Smith, D., Lemoine, F., Mazarico, E., Sabaka, T., Goossens, S., Melosh, H. J., Phillips, R., Asmar, S., Konopliv, A., Williams, J., Sori, M., Soderblom, J., Miljković, K., Andrews-Hanna, J., Nimmo, F. and Kiefer, W. (2015), 'Lunar impact basins revealed by Gravity Recovery and Interior Laboratory measurements', *Science Advances* **1**(9).

Ohtake, M., Matsunaga, T., Haruyama, J., Yokota, Y., Morota, T., Honda, C., Ogawa, Y., Torii, M., Miyamoto, H., Arai, T., Hirata, N., Iwasaki, A., Nakamura, R., Hiroi, T., Sugihara, T., Takeda, H., Otake, H., Pieters, C., Saiki, K., Kitazato, K., Abe, M., Asada, N., Demura, H., Yamaguchi, Y., Sasaki, S., Kodama, S., Terazono, J., Shirao, M., Yamaji, A., Minami, S., Akiyama, H. and Josset, J. (2009), 'The global distribution of pure anorthosite on the Moon', *Nature* **461**(7261), 236–240.

Oppenheim, A., Willsky, A. and Nawab, S. (1996), *Signals & Systems (2nd Ed.)*, Prentice-Hall, Inc., USA.

Park, R. S., Konopliv, A. S., Yuan, D. N., Asmar, S., Watkins, M. M., Williams, J., Smith, D. E. and Zuber, M. T. (2015), A high-resolution spherical harmonic degree 1500 lunar gravity field from the GRAIL mission, *in* 'AGU Fall Meeting Abstracts', Vol. 2015.

Petro, N. and Pieters, C. (2004), 'Surviving the heavy bombardment: Ancient material at the surface of South Pole-Aitken Basin', *J. Geophys. Res* **109**.

Pogge, R. (2008), 'Lecture 8: Phases of the Moon'. Astronomy 161: An Introduction to Solar System Astronomy.

Sakai, T. and Nakamura, A. (2005), 'Quantification of porosity and surface roughness in laboratory measurements of the bidirectional reflectance of asteroid surface analogues, journal=Earth, Planets and Space', **57**(1), 71–76.

Scott, E. (2015), *Our Moon: New Discoveries about Earth's Closest Companion*, Clarion Books.

Shkuratov, Y. (1981), 'Connection Between the Albedo and Polarization Properties of the Moon: Fresnel Component of Reflected Light', *Soviet Astronomy* **25**, 490.

Shkuratov, Y., Kaydash, V., Korokhin, V., Velikodsky, Y., Opanasenko, N. and Videen, G. (2011), 'Optical measurements of the Moon as a tool to study its surface', *Planetary and Space Science* **59**(13), 1326 – 1371.

Shkuratov, Y. and Opanasenko, N. (1992), 'Polarimetric and photometric properties of the moon: Telescope observation and laboratory simulation: 2. The positive polarization', *Icarus* **99**(2), 468 – 484.

Shkuratov, Y., Opanasenko, N. and Korokhin, V. (2015), The Moon, Cambridge University Press, pp. 303–319.

Shkuratov, Y., Opanasenko, N. and Kreslavsky, M. (1992), 'Polarimetric and photometric properties of the Moon: Telescopic observations and laboratory simulations: 1. The negative polarization', *Icarus* **95**(2), 283 – 299.

Shkuratov, Y., Opanasenko, N., Opanasenko, A., Zubko, E., Bondarenko, S., Kaydash, V., Videen, G., Velikodsky, Y. and Korokhin, V. (2008), ‘Polarimetric mapping of the Moon at a phase angle near the polarization minimum’, *Icarus* **198**, 1–6.

Shkuratov, Y., Opanasenko, N., Zubko, E., Grynko, Y., Korokhin, V., Pieters, C., Videen, G., Mall, U. and Opanasenko, A. (2007), ‘Multispectral polarimetry as a tool to investigate texture and chemistry of lunar regolith particles’, *Icarus* **187**(2), 406–416.

Sim, C., Kim, S., Jeong, M., Choi, Y. and Shkuratov, Y. (2020), ‘Lunar Polarimetry from its Orbit with KPLO/POLCAM: Phase-angle Coverage’, *Lunar and Planetary Science Conference* **51**.

Smith, D., Zuber, M., Jackson, G., Cavanaugh, J., Neumann, G., Riris, H., Sun, X., Zellar, R., Coltharp, C., Connelly, J., Katz, R., Kleyner, I., Liiva, P., Matuszeski, A., Mazarico, E., McGarry, J., Novo-Gradac, A., Ott, M., Peters, C., Ramos-Izquierdo, L., Ramsey, L., Rowlands, D., Schmidt, S., Scott, V., Shaw, G., Smith, J., Swinski, J., Torrence, M., Unger, G., Yu, A. and Zagwodzki, T. (2010), ‘The Lunar Orbiter Laser Altimeter Investigation on the Lunar Reconnaissance Orbiter Mission’, *Space Science Reviews* **150**(1), 209–241.

Smith, D., Zuber, M., Neumann, G. and Lemoine, F. (1997), ‘Topography of the Moon from the Clementine lidar’, *Journal of Geophysical Research: Planets* **102**(E1), 1591–1611.

Smith, M., Craig, D., Herrmann, N., Mahoney, E., Krezel, J., McIntyre, N. and Goodliff, K. (2020), The Artemis Program: An Overview of NASA’s Activities to Return Humans to the Moon, *in* ‘2020 IEEE Aerospace Conference’, pp. 1–10.

Srivastava, N. and Varatharajan, I. (2016), ‘Geomorphology of Lowell crater region on the Moon’, *Icarus* **266**, 44–56.

Staid, M., Pieters, C. and Head III, J. (1996), ‘Mare Tranquillitatis: Basalt emplacement history and relation to lunar samples’, *Journal of Geophysical Research: Planets* **101**(E10), 23213–23228.

Stinson, A. (2016), Polarimetry of small bodies of the Solar System, PhD dissertation, University College London.

Szekely, G., Rizzo, M. and Bakirov, N. (2007), ‘Measuring and testing dependence by correlation of distances’, *The Annals of Statistics* **35**(6), 2769 – 2794.

Tapley, B. D., Bettadpur, S., Watkins, M. and Reigber, C. (2004), ‘The gravity recovery and climate experiment: Mission overview and early results’, *Geophysical Research Letters* **31**(9).

Taylor, S., Taylor, G. and Taylor, L. (2006), ‘The Moon: A Taylor perspective’, *Geochimica et Cosmochimica Acta* **70**(24), 5904–5918.

Velikodsky, Y., Opanasenko, N., Akimov, L., Korokhin, V., Shkuratov, Y., Kaydash, V., Videen, G., Ehgamberdiev, S. and Berdalieva, N. (2011), ‘New earth-based absolute photometry of the moon’, *Icarus* **214**(1), 30 – 45.

von Engelhardt, W., Hurrle, H. and Luft, E. (1976), ‘Microimpact-induced changes of textural parameters and modal composition of the lunar regolith.’, *Lunar and Planetary Science Conference Proceedings* **1**, 373–392.

W.D. McComb (1999), *Dynamics and Relativity*, Oxford University Press.

Wieczorek, M. (2015), ‘Gravity and Topography of the Terrestrial Planets’, *Treatise on Geophysics* (2), 153–193.

Wieczorek, M. A. and Meschede, M. (2018), ‘SHTools: Tools for Working with Spherical Harmonics’, *Geochemistry, Geophysics, Geosystems* **19**(8), 2574–2592.

Wieczorek, M., Neumann, G., Nimmo, F., Kiefer, W., Taylor, G., Melosh, J., Phillips, R., Solomon, S., Andrews-Hanna, J., Asmar, S., Konopliv, A., Lemoine, F., Smith, D., Watkins, M., Williams, J. and Zuber, M. (2013), ‘The crust of the moon as seen by GRAIL’, *Science (New York, N.Y.)* **339**.

Wieczorek, M. and Simons, F. (2007), ‘Minimum-Variance Multitaper Spectral Estimation on the Sphere’, *Journal of Fourier Analysis and Applications* **13**(6), 665–692.

Zellner, N. E. B. (2019), ‘Lunar Impact Glasses: Probing the Moon’s Surface and Constraining its Impact History’, *Journal of Geophysical Research: Planets* **124**(11), 2686–2702.

Zuber, M., Smith, D., Lehman, D., Hoffman, T., Asmar, S. and Watkins, M. (2013), ‘Gravity Recovery and Interior Laboratory (GRAIL): Mapping the Lunar Interior from Crust to Core’, *Space Science Reviews* **178**.

Zuber, M., Smith, D., Watkins, M., Asmar, S., Konopliv, A., Lemoine, F., Melosh, J., Neumann, G., Phillips, R., Solomon, S., Wieczorek, M., Williams, J., Goossens, S., Kruizinga, G., Mazarico, E., Park, R. and Yuan, D. (2012), ‘Gravity Field of the Moon from the Gravity Recovery and Interior Laboratory (GRAIL) Mission’, *Science (New York, N.Y.)* **339**.